Immunoengineering Approaches for the Treatment of Cancer and Prevention of Infectious Diseases

By

Charles Park

A dissertation submitted in partial fulfillment
of the requirements for the degree of
Doctor of Philosophy
(Biomedical Engineering)
in The University of Michigan
2021

Doctoral Committee:

Associate Professor James J. Moon, Chair
Assistant Professor Kelly B. Arnold
Associate Professor Deepak Nagrath
Associate Professor Sunitha Nagrath

Charles Park

pcharlie@umich.edu

ORCID iD: 0000-0003-1339-5673

ACKNOWLEDGEMENTS

First and foremost, I would like to thank Dr. James Moon for his support and allowing me to join his lab. He has been a great mentor that kept me motivated and influenced me in many aspects. I've learned to keep the persistence and diligence in research, to have passion and pride in what I study, and how I should pursue forward as a scientist. I would also like to sincerely thank my committee members, Dr. Kelly Arnold, Dr. Deepak Nagrath and Dr. Sunitha Nagrath for their kind words, guidance and thoughtful critiques during the preparation of my thesis.

I consider myself lucky to have joined Dr. Moon's lab where I met friends for life. Cameron, Yuchen, Joe, Lukasz, Emeka and Lindsay were the best lab mates. I still think of and reminisce the times when we were altogether in the lab, and those memories have been a great source of moral support for me that I am sure made it possible for me to handle the hardships I went through during the past five years as a PhD student.

Also, the times I spent together with the current lab members, Xiaoqi, Cheng, Jin, and Marisa as coworkers and friends would be unforgettable. I always enjoyed the discussions we shared, and I feel like every word we spoke, even the meaningless jokes, will be missed. I hope as great colleagues and friends, our relationships will continue just as they are now. Also, I want to thank Jutaek, Sejin and Kai for their times spent for scientific discussions with me and sharing their experiences, from which I learned so much to become a better scientist. Lastly, I would like to thank Yao, for helping me with many experiments and making our lab the best environment for

conducting experiments.

My best friend, Seung Won Shin, has been a huge support for me as always that I would appreciate for life. Our chats, despite the time lag and the distance between where we are, were one of the most interesting and motivating conversations I had. His moral support was huge especially during the rough times and made me able to endure those times. Also, I will not forget the help and advice that Dr. Sung Jin Park gave me when I needed them the most. He has been one of the mentors that significantly influenced me as a scientist.

Lastly, I cannot thank enough for the infinite support from my parents and their belief in me. They were the ones I would seek talking to when I was going through my worst days and helped me make good decisions that led me here. Also, my girlfriend, Jeongyun Yang, gave me support more than any others in so many ways and made my time in Michigan the happiest time in my life so far.

TABLE OF CONTENTS

LIST OF FIGURES

on day 0 and vaccinated at s.c. tail base on day 7 with the indicated vaccines. A subset of animals also received intratumoral administration of 0.5 μg CDA on day 11. On day 14, animals were analyzed for (**b)** Adpgk-tetramer+CD8+ T cells within PBMCs, (**c)** tumor-infiltrating CD3+CD8+ T cells, and (**d)** tumor-infiltrating Adpgk-tetramer+CD3+CD8+ T cells by flow cytometry. (**e)** Concentrations of IFN-γ were measured in tumors using ELISA. (**f)** Timeline of experiment. C57BL/6 mice inoculated at s.c. flank with $6x10^5$ MC-38 colon carcinoma cells on day 0 were vaccinated on day 7 via s.c. tail base. These mice received intratumoral administration of 0.5 μg CDA on days 11, 14, and 17. Shown are (**g)** the average tumor growth curves and (**h)** animal survival. (**i)** Tumor growth curve after re-challenging survivors with MC-38 cells. Mice were re-challenged with $1.2x10^6$ MC-38 cells by subcutaneous injection on the left-side flanks 90 days after the initial tumor inoculation. Data are presented as mean ± SEM. *$p < 0.05$, **$p < 0.01$, ***$p < 0.001$, and ****$p < 0.0001$, analyzed by (**b-e)** one-way ANOVA followed by Tukey's HSD multiple comparison post hoc test or (**g,i)** two-way ANOVA followed by Sidak's multiple comparisons test. (**h)** The survival curves were analyzed by the log-rank (Mantel−Cox) test. ... 44

Figure 3-6. PEI NP vaccine plus CDA combination therapy regresses poorly immunogenic B16F10 melanoma. a) Timeline of experiment. While tumor growth and survival of B16F10-bearing mice were monitored, subsets of mice were sacrificed on day 11 for ELISPOT and ELISA analyses using spleens and tumor samples, respectively. b) Neoantigen peptide (M27)-specific cells within splenocytes were detected with IFN-γ ELISPOT assay. c) Cytokine concentrations in tumor measured by ELISA. d) Tumor growth and e) survival curves of B16F10 tumor-bearing mice. Asterisks in d) indicate statistical comparison between CDA and NP Vacc + CDA. Data are presented as mean ± SEM. *$p < 0.05$, **$p < 0.01$, and ****$p < 0.0001$, analyzed by **b,c)** one-way ANOVA followed by Tukey's HSD multiple comparison post hoc test or **d)** two-way ANOVA

ABSTRACT

The field of immunoengineering is highly interdisciplinary, involving the insights from various other fields of studies such as physiology, computation, pharmacology, materials science and many more. With the recent progress in technology development, analyzing detailed cellular interactions that constitute the immune system has become possible, and many more biological and engineering tools became within reach for precise investigation and modulation of immune responses. As a result, many breakthroughs have been achieved in various clinical settings. Immunotherapies, such as anti-PD-1 antibody and chimeric antigen receptor T cells, revolutionized cancer immunotherapy, while genome sequencing and nanotechnology allowed for the rapid development of various vaccines in response to the recent outbreak of Coronavirus Disease 2019. Also, analysis of massive amount of data collected from the bacterial genome within various parts of the body, called the microbiome, is enabling us to study the relationship between the microbiota and human body and health, and is suggesting new ways of treating once thought to be hard-to-treat diseases.

In Chapters II and III, strategies for modulating the immune responses using biomaterials for cancer immunotherapy are introduced. Chapter II describes silica-based nanoparticle-mediated stimulator of interferon gene (STING) agonist delivery. Compared to soluble form of STING agonist, it induced ~4-fold higher dendritic cell activation *in vitro*, accompanied by significantly enhanced cytokine secretion, which together with prolonged immune cell activation within the tumor microenvironment, greatly improved therapeutic efficacy of the STING agonist in mouse

melanoma models. In Chapter III, an adjuvant and a model neoantigen peptide were formulated into a nanoparticle, which increased dendritic cell activation and antigen presentation by 2~4 folds and 4-folds, respectively *in vitro* compared to soluble formulation. It translated to ~3 folds higher antigen-specific CD8+ T cell frequency in blood circulation in mice. In addition, an attempt to induce a stronger chemokine gradient to recruit more T cells to tumor from the blood circulation was also investigated.

In Chapter IV, use of lipid-based nanoparticle to formulate vaccines against infectious diseases, including human immunodeficiency virus-1 (HIV-1) and severe acute respiratory syndrome coronavirus-2 (SARS-CoV-2), is introduced. The aim of the study was to load subunit proteins into lipid-based nanoparticles while maintaining the structural intactness and to induce enhanced antibody responses when vaccinated to animals. Nanoparticle vaccine enhanced *in vitro* dendritic cell activation and antigen presentation, while improving antigen trafficking to lymph node *in vivo*, leading to significantly enhanced IgG responses in animals.

In Chapter V, I investigated the effects of prebiotics on gut microbiota and immune responses during cancer immunotherapy using a cancer vaccine. Recently the communication between the gut microbiota and the immune system started to be revealed, thanks to mass data analysis and genome sequencing becoming more available for general research purposes. Also, studies are reporting the correlation of certain bacterial species and their metabolites with immunotherapeutic outcomes during cancer immunotherapies. Here, I sought to investigate the effects of prebiotics consumption on gut microbiota and if changes in bacterial frequencies can modulate the immune responses following cancer vaccination using mouse tumor models.

Lastly in Chapter VI, I present the overall review of the studies in this thesis. Also, future directions to pursue are discussed with ways to provide complementing information to some of the

experiments, which currently can only suggest limited insights, and potential clinical translation in mind.

CHAPTER I. Introduction

1.1. Background

Immunotherapy has gathered huge interests especially in the recent decades with the advent of advanced biological tools and computation technologies. With accumulating knowledge and data, immunoengineering approach to treat diseases became very effective and practical over the years, creating many different strategies of modulating the immune responses depending on the type of diseases. Here, strategies for treating cancer and infectious diseases by modulating innate and adaptive immune responses using immune-modulating agents and biomaterials as tools will be discussed. Depending on the type of disease, different stages of immune responses were targeted for modulation with strategies and materials carefully chosen. Described in more details in the following pages, the main research areas to be discussed are (1) cancer immunotherapy, (2) development of vaccines for infectious diseases, and (3) prebiotics delivery for enhancing immune responses.

1.2. Cancer immunotherapy

One of the most actively investigated areas of immunoengineering research is cancer immunotherapy. Programmed cell death receptor-1 (PD-1) blockade therapy may be one of the most well-known recent breakthrough discoveries in the field of cancer immunotherapy (*1, 2*). Within the tumor microenvironment, immunosuppression becomes more severe as the tumor progresses to later stages, through various mechanisms (*3, 4*). One of the major pathways the

spontaneously formed tumor-specific CD8+ T cells are inhibited is by the engagement of their PD-1 receptors with the ligands, PD-L1 and PD-L2, expressed on tumor cells. Treatment of anti-PD-1 or anti-PD-L1 antibodies has proven to have significantly meaningful efficacies in various cancers, including melanoma, colon carcinoma, head and neck squamous cell carcinoma, and many more (*5-10*). Another breakthrough is now a well-known chimeric antigen receptor T cell therapy (*11-14*). So called CAR-T, falls into the category of adoptive cell transfer (ACT) therapy, which is one of the cancer therapeutic techniques that transfers ex vivo expanded T cells to patients from different sources including autologous tumor infiltrating T cells and genetically modified peripheral T cells (*14*). Usually, the patient receiving ACT is preconditioned by eliminating pre-existing lymphocytes in the body to maximize availability of cytokines to the transferred T cells that leads to greater expansion post transfer and prolong their existence in the blood circulation. CAR-T targeting CD19 expressed by leukemic B cells achieved outstanding response rates in patients with acute lymphoblastic leukemia (ALL) and have attracted a tremendous number of resources to the field. With CAR-Ts that target different receptors than CD19, such as CD20 and CD22, this technology is continuously evolving to prevent relapse and be more effective in treating different kinds of Hematologic Malignancies (*15, 16*).

Together with the aforementioned hypes in the field, the discovery of neoantigen brought a huge revolution to how we perceive cancer which was once thought to be a disease that is expert at eluding the immune surveillance (*17*). Recent advances in genomics and proteomics discovered mutations within the somatic genes of tumor cells. The so-called tumour mutanome revealed that every tumor has a unique set of driver and passenger mutations (*17-19*). Tumor cells expressing mutated proteins (neoantigens) present these new epitopes in the context of major histocompatibility complex (MHC) molecules. In contrast to tumor associated antigens (TAA),

whose expression is shared among healthy and tumor cells, neoantigens arise from mutations in tumors and are, therefore, fully restricted to tumor cells. Thus, immunotherapies that capitalize on rich genomic and proteomic bioinformatics data for personalized strategies directed to neoantigens are enabling highly specific targeting of tumour cells without risking healthy tissues or being limited by immune tolerance (*20*). Using the neoantigens of different kinds that are synthesized into forms of DNA, RNA or peptides, cancer vaccines were produced to effectively treat different kinds of cancers, and currently many clinical trials are undergoing either as a monotherapy or in combination with various delivery vehicles and adjuvants (*21-24*).

Despite these advances, still only a fraction of patients undergo complete tumor regression. There are many reasons for this, including immunosuppressive TME and suboptimal immune activation by therapeutic treatments. Immune response during cancer therapy is initiated by the release of tumor-specific antigens from spontaneously dying tumor cells or drug- or immune cell-induced tumor cell death. These antigens are taken up by antigen presenting cells, processed into peptides that are presented on the MHC molecules, which together with co-stimulatory ligands on the APCs (B7.1/2) activate naïve T cells in the lymph nodes. T cells then proliferate and become effector cells, which effuse out from the lymph node into the blood circulation. They migrate following the chemokine gradient, traffic to and infiltrate the tumor. Many immunoengineering approaches are developed to solve the aforementioned issues that cause suboptimal therapeutic outcomes, by taking various strategies to modulate different stages of the immune responses and immune cell types, such as dendritic cells and T cells.

Use of nanoparticles is one of the most commonly used strategies to enhance the efficacies of various therapeutics (*25*). Depending on the material and structural design of the nanoparticle, nanoparticle-mediated drug or vaccine delivery is reported to improve pharmacokinetics after

systemic administration, enabling co-delivery of adjuvant to antigen presenting cells (APC) for enhanced innate immune responses and increase the delivery of drugs to a targeted site within the body (*26, 27*).

Another hurdle to achieving successful cancer immunotherapy is to increase tumor-infiltration of antigen-specific CD8+ T cells. Many types of tumors are reported to down-regulate the expression of T cell attractant chemokines or have immature blood vessels, so-called leaky vasculature that limits the transmigration of T cells across the blood vessels into tumor tissues (*28-30*). In such cases, the CD8+ T cells in the blood circulation either generated by vaccination or by adoptive cell transfer, fail to traffic to and infiltrate tumor. It is reported that the degree of tumor-infiltration by lymphocytes is correlated with the patient prognosis (*31, 32*), highlighting the importance of finding the means to overcome this issue. In some studies, treatment of chemo-drugs, such as cisplatin and temozolomide (*33*), or agonists of pattern recognition receptors (PRR), such as stimulator of interferon genes (STING) agonist and cytosine-guanine-rich (CpG) motifs (CpG-ODN) (*34, 35*), within tumors triggered the release of lymphocyte attractant chemokines from the tumor, increasing the tumor infiltration by T cells and NK cells. Therefore, it is presumed that in addition to other forms of immunotherapies that stimulate inflammatory immune responses against tumor, combinatorial treatment of therapeutics to recruit lymphocytes to tumor may provide a great synergy to achieving improved therapeutic outcome.

In Chapters II and III, immunomodulation strategies using nanoparticle-mediated drug and vaccine delivery for cancer immunotherapy are discussed. First, a silica-based nanoparticle was used to deliver a model STING agonist to enhance the activation of dendritic cells (DC), which led to improved tumor growth suppression in mouse melanoma models. Next, a charge-induced nano-sized complex of cationic polymer and CpG was used to formulate a peptide-based cancer

vaccine to induce stronger DC activation and antigen presentation and subsequent CD8+ T cell responses. In combination with the vaccine treatment, STING agonist was treated to tumor to induce T cell attractant chemokine release from the tumor, which resulted in increased tumor infiltration by the vaccine-induced CD8+ T cells in the blood circulation.

1.3. Infectious diseases

Pathogenic bacteria and virus cause infectious diseases, the symptoms of which range from light to heavy illnesses, in some cases that reach serious morbidity or mortality. Many have been identified in history and are now well-known and thoroughly studied, while there are still newly emerging diseases that sometimes are alerting to the human society. Historically, there had been a number of outbreaks of infectious diseases that were highly contagious, causing epidemics that sometimes led to pandemics (*36*-*38*). Plague by a species of bacteria that caused Black Death and avian-origin viral infections that caused Spanish Flu are among many well-known pandemics that took many lives. With improved sanitization and more importantly by the advent of chemo-drugs and vaccines, many once thought to be detrimental and contagious diseases were able to be controlled and contained before being widely spread.

While, on the bright side, many diseases are now in control with some of them even assumed to be extinct by ever improving vaccine and drug development technologies, there is a rising concern over the fight against infectious diseases. That is, the term between appearances of new pathogens with high transmissibility or mortality, thus with the potential to cause epidemic or to pandemic, is becoming shorter in the recent decades. One of the main reasons for the increased frequency is the apparent changes that have occurred in our society, such as overpopulation, increasing international travels and indoor activities. Most recently, first reported in December

2019, a novel corona virus called severe acute respiratory syndrome coronavirus 2 (SARS-CoV-2) that spread throughout the world with an upsetting speed was declared a pandemic in March 2020 and was named Coronavirus Disease 2019 (COVID-19). Unlike in the cases of similar viruses such as SARS-CoV that caused the 2002 epidemic and MERS-CoV that attracted global concerns due to its high mortality rate in 2012, both of which were managed to be contained, many conditions, such as ever-increasing international travels, overpopulation and mild- or asymptomatic, yet transmissible incubation period, were met in the case of SARS-CoV-2 that let the virus exude out from the efforts to contain it regionally from where it began, and eventually spread globally at an epic speed to cause the pandemic (*39*).

We have learned now that similar outbreaks will inevitably occur in future with shorter frequencies, which prompted global interest in developing interventions to counter diseases that cause such outbreaks. Broadly, those interventions can be categorized as either therapeutic or prophylactic. Both types of interventions ultimately aim to have a certain percentage of people in a community to have immunity that prevents further spread of the disease, which is termed communal/herd immunity. However, finding or discovering a therapeutic that shows sufficient efficacy each time an outbreak occurs, if at all possible, would be very challenging. Especially in the urgent setting of an epidemic outbreak, the extremely low percentile of drug candidates reaching the market and the typical time of 10 years spent for development of a new drug may seem even more unrealistic. To expedite the provision of efficacious drugs to the clinic, searching among drugs that are mostly FDA approved, called drug repurposing, is gaining a lot of attentions (*40*). However, when a novel pathogen arises, lack of preclinical study models and limited availability of pathogen and its biological/pathological information would still pose hurdles.

Similarly, vaccine development may also be challenging and time consuming when facing an epidemic outbreak by a novel pathogen. The process of developing a vaccine consists of two key steps: 1) identifying an antigen and 2) developing a delivery approach for said antigen to achieve robust cellular and humoral immunity. In case of COVID-19, our experiences of SARS-CoV and MERS-CoV have enabled fast reaction against SARS-CoV-2 since analysis of viral genomic sequence and protein structures of ligands that bind to human receptors became rapidly available due to similarities between these viruses. It was discovered that SARS-CoV-2 can be targeted at specific sites of its surface glycoprotein called spike protein. 3D structural analyses have confirmed that the S1 subunit protein and more specifically the receptor binding domain (RBD) within the protein to be critical structural regions for the virus to bind with angiotensin-converting enzyme 2 (ACE2) expressed on human cells and initiate infection (*41, 42*). Likewise, for future pathogens that may arise in future, various simulation and computation methods together with our experiences of encounters with previous variants of the pathogen may provide an expedited identification of targetable antigen.

On the other hand, development of delivery approaches for efficient immune activation by a vaccine antigen is in the realm where we can invest on before an outbreak occurs (*43*, *44*). Different types of vaccine technologies are used to develop vaccines which can be categorized depending on the type of antigen used: inactivated/attenuated virus, RNA, DNA and protein (*45*). Whole virus has been a type of vaccine conventionally used that brought a huge health benefit to human life, saving many lives while greatly reducing the cases of many major diseases, such as smallpox, tuberculosis and yellow fever. Live attenuated virus and inactivated virus are the two major types of whole virus vaccine. Live attenuated viruses are developed by passaging a virus multiple times in environments that differ from those of human hosts, making the virus lose its

ability to infect and replicate within human. In contrast, inactivated viruses are made by various ways to kill the virus, such as heating or chemical treatments. Therefore, as opposed to live attenuated vaccines, inactivated vaccines do not bear the risk of viral reversion. However, the reagents used to inactivate the live viruses often are damaging to the parts of the virion structure that is essential to the immunogenicity of the vaccine. Therefore, the vaccines synthesized with this method often fail to meet acceptable potency or need multiple vaccination regimen to achieve sufficient protection.

In contrast to whole virus vaccines that are administered in the forms of virions, DNA, RNA and protein vaccines have an option to be encapsulated in delivery platforms which may enhance the vaccine potency. Many of the DNA and RNA vaccines (especially the RNA vaccines) currently under development for COVID-19 are in the forms of nanoparticles consisted of lipid-based materials (*46*). Nanoparticles are used to achieve efficient trafficking of the vaccine antigen to the lymph node, co-delivery of adjuvant that further enhances the immune activation, and protection of antigen from degradation, benefiting the pharmacokinetics.

It is important, however, to carefully design the structure and material of the delivery carrier depending on the type of antigen material, whether it being DNA, RNA or protein, the route of administration and expected pharmacokinetics after administration. Especially when protein subunits are used as the vaccine antigen, maintaining the quaternary and tertiary structures of the protein during the nanoparticle loading process is critical during the vaccine formulation, since it enables the vaccine to present appropriate epitopes to the immune cells, which is closely related to the generation of quality neutralizing antibodies that are effective at neutralizing the pathogens (*47*). In Chapter IV, generation of protein-based vaccines made in a form of lipid nanoparticle is introduced. Glycoproteins of human immunodeficiency virus-1 and RBD of SARS-CoV-2 are

used as model antigens to be loaded in the lipid nanoparticles, and rationale and the methods of formulating effective vaccines that generate potent antibody responses in mouse and rabbit are discussed.

1.4. Effects of prebiotics on gut microbiome and immune responses

Microbiota is a collection of microorganisms that include bacteria, virus and fungi. Microbiome refers to the genomic materials as well as the physical entities of the microbes consisting the microbiota. It has been revealed that human body harbors multiple microbiotas depending on the organs or parts of the body. With the advances in sequencing tools and mass data analysis, people are able to take a deeper look into the composition of each microbiota and the factors that influence the bacterial residents within the microbiota.

The gut microbiome is one of the most actively studied subjects of microbiome research, where the food that we consume has been identified to be a critical factor to how gut bacteria react and metabolize, and ultimately to our general health (*48, 49*). More importantly, recent studies are finding scientific bases for the close relationship between the gut microbiota and host immunity. Depending on how the diet is regulated, one may either suffer from autoimmune or inflammatory disorders or may elicit robust immune responses against intrusions of external pathogens (*50-52*). In particular, consumption of dietary fibers is known to provide sources for gut bacteria to metabolize on, which upon fermentation generates short chain fatty acids (SCFA) as the metabolic products. Studies are reporting the effects of SCFA on the various types of immune cells, including dendritic cells, T cells, and many more (*53-55*), and their contributions during cancer immunotherapy (*56-58*). Although there are contrasting reports of the effect of SCFA levels in blood on the clinical responses upon therapeutic interventions, such as anti-PD-1 or anti-CTLA-4

antibody treatments (*58, 59*), it is certain that the bacterial metabolites have significant impact on how the immune system is regulated.

Based on these clues, people were able to predict the relationship between the gut microbiome and the way hosts respond to vaccination. From mice studies, immune responses induced by vaccination were varied based on whether a mouse received antibiotics or was kept in a germ-free environment (*60, 61*). Later, similar effects were observed in human cases, where antibiotic treatment led to marked reduction in bacterial loads in the gut and significantly reduced flu vaccine efficacy (*62, 63*). Therefore, from an immunoengineering perspective, modulation of immune response upon vaccination may be achieved by influencing the gut microbiome, and consumption of dietary fibers is a great way to achieve that goal. In Chapter V, the effects of prebiotics consumption on microbiome and subsequent influence on cancer vaccine efficacy in mouse tumor model are discussed.

CHAPTER II. Improving STING Agonist Delivery for Cancer Immunotherapy Using Biodegradable Mesoporous Silica Nanoparticles

2.1. Abstract

Stimulator of interferon genes (STING) activation by intratumoral STING agonist treatment has been recently shown to eradicate tumors in preclinical models of cancer immunotherapy, generating intense research interest and leading to multiple clinical trials. However, there are many challenges associated with STING agonist-based cancer immunotherapy, including low cellular uptake of STING agonists. Here, biodegradable mesoporous silica nanoparticles (bMSN) with an average size of 80 nm have been developed for efficient cellular delivery of STING agonists. STING agonists delivered via bMSN potently activate innate and adaptive immune cells, leading to strong anti-tumor efficacy and prolonged animal survival in murine models of melanoma. Delivery of immunotherapeutic agents via biodegradable bMSN is a promising approach for improving cancer immunotherapy.

2.2. Introduction

Exogenous nucleic acids that have successfully bypassed external sensing and appear in the cytosol are processed by cyclic GMP–AMP synthase (cGAS) into cyclic dinucleotides (CDNs), which engage stimulator of interferon genes (STING) molecules positioned along the endoplasmic reticulum. This triggers the interferon regulatory factor 3 (IRF-3) and nuclear factor kappa-light-

chain-enhancer of activated B cells (NFκB) signaling pathways and leads to type I interferon and pro-inflammatory cytokine production. In addition to protection against viral and bacterial infections, recent findings have also revealed a critical role of STING in initiating immune responses against cancer. Numerous studies have reported promising anti-cancer effects of STING agonists (*64, 65*). Importantly, STING agonist treatment induces significant anti-tumor immune responses, leading to complete tumor regression and durable anti-tumor immunity in multiple murine tumor models (*66, 67*). Compared with other PRR-binding adjuvants, STING agonists showed a distinct potency in that their sole treatment led to complete regression of established tumors in preclinical settings. The role of STING agonists in triggering type I interferon response leading to activation of various immune cell types suggests many potential applications for cancer treatment. Based on many promising preclinical studies, two types of STING agonist have undergone clinical evaluation as a single treatment or in combination with immune checkpoint blockers. Thus, STING has sparked intense research interest in the field of cancer immunotherapy (*68, 69*), and there are multiple clinical trials underway to evaluate the therapeutic efficacy of STING agonists.

Despite their outstanding efficacies against various types of tumors, there are several hurdles of using soluble forms of STING agonist that limits their clinical translation. As STING agonists are based on cyclic dinucleotides with negative charges, their cellular permeability is minimal. Since STING molecules reside within the cytosol where endoplasmic reticulum is located, inability to permeate into cytosol leads to suboptimal activation of STING at a given dose. Also, due to their small molecular weight, STING agonists diffuse rapidly into systemic circulation upon injection, which may potentially cause severe off-target side-effects. Therefore, most preclinical and clinical studies with STING agonists have been limited to direct intratumoral injection, which

limits their use to treating local tumors. A recent report on STING activation in T cells leading to cell death exposes a negative effect of STING activation on cell types other than innate immune cells (*70*). In addition, since natural STING agonists are based on inherently unstable CDN structures, they exhibit a fast clearance from blood circulation. Lastly, the amount of STING agonist injected to tumor has been shown to dictate CD8+ T cell response (*71*), underscoring the importance of regulating the dose and pharmacokinetics of STING agonist to achieve robust anti-tumor immunity.

Here, we sought to promote cellular delivery of STING agonists using a well-established nanoparticle system with a strong track record of biocompatibility, safety, and manufacturability, considering the overarching direction of design to clinical translation. In particular, mesoporous silica nanoparticle (MSN) is a widely used inorganic drug delivery nanocarrier with tunable size, low immunogenicity, controlled release of cargo materials, and facile and low-cost preparation process (*72, 73*). However, while synthetic MSNs composed of amorphous silica are generally considered to be biocompatible, their limitations include relatively small pore sizes for drug loading, slow biodegradation, and long-term tissue retention (*74-78*). To address these issues, we have developed biodegradable mesoporous silica nanoparticles (bMSN) for cytosolic delivery of STING agonists. We have recently shown that bMSN with a less-dense Si-O-Si matrix undergoes faster biodegradation process than conventional MSN and that bMSN's large pore size ranging 5-10 nm allows for efficient loading and delivery of biomacromolecules for combination cancer treatments (*79*). Here, we report that bMSN surface-modified with amine serves as a promising platform for cellular delivery of STING agonists and immune activation. Using two murine models of melanoma, we demonstrate the therapeutic efficacy of bMSN carrying STING agonists, highlighting the potential of bMSN for applications in cancer immunotherapy.

2.3. Materials and Methods

Synthesis of bMSN and CDA loading

We synthesized bMSN by an oil-water biphase reaction approach.[22,41] Twenty-four ml of (25 wt %) CTAC solution and 0.18 g of TEA were added to 36 ml of water and stirred gently at 60 °C for 1 hr. Twenty ml of TEOS in cyclohexane (10 v/v %) was carefully added to 60 mL of the water-CTAC-TEA solution (0.3 M CTAC and 20 mM TEA) and kept at 60 °C. The reaction was kept at a constant temperature with continuous stirring for 18 hr to obtain nanoparticles. They were washed with ethanol for 3 times and water for 2 times with centrifugation at 15,500g for 15 min. Surfactant was removed by incubating the nanoparticles in 10% NH4NO3/ethanol (v/v) at 50 °C overnight, followed by washing. The resulting nanoparticles were freeze-dried and stored at 4°C until use. To load CDA, 40 μg of CDA was mixed with 225 μg of bMSN in 5 mM histidine buffer, followed by 1 min of bath sonication. The mixture was incubated in 37 °C for 1 hour under constant shaking, then centrifuged at 10,000 g for 5 min. After removing the supernatant, the pellet was dispersed into PBS. The resulting CDA@bMSN showed 96.3% of CDA loading efficiency.

In vivo studies

Animals were cared for following the federal, state, and local guidelines. The University of Michigan, Ann Arbor is an AAALAC international accredited institution, and all work conducted on animals was in accordance with and approved by the Institutional Animal Care and Use Committee (IACUC) with the protocol # PRO00008587. Female C57BL/6 mice, 5-6 weeks in age (The Jackson Laboratory) were inoculated subcutaneously with 3x105 mouse melanoma cells (either B16F10 or B16F10OVA) on the right-side flank. After 6 days, mice received CDA formulations (PBS as control) via intratumoral injection. Blood sampling and tumor excision were

performed on the indicated time points. Blood samples were collected from the facial vein using a lancet. In a separate study, tumor sizes were measured every 2-3 days for monitoring tumor growth.

Statistical analysis

Data are presented as mean ± SEM. Data were approximately normally distributed, and variance was similar between the groups. Experiments were repeated multiple times as independent experiments with the sample size indicated in the figure captions. Data were analyzed using either one-way analysis of variance (ANOVA) or two-way ANOVA, followed by Tukey's multiple comparison test for comparison of multiple groups using Prism 7.0e (GraphPad Software). Animal survival was analyzed by the log-rank (Mantel−Cox) test. *$p < 0.05$, **$p < 0.01$, ***$p < 0.001$, and ****$p < 0.0001$.

2.4. Results and Discussion

We synthesized bMSN as we previously reported with some modifications for cytosolic delivery of STING agonists (*79*). The resulting bMSN had an approximate average diameter of 80 nm, as visualized by transmission electron microscopy (TEM) (**Figure 2-1a**). Compared with conventional mesoporous silica nanoparticles, bMSN had a larger pore size (5 – 10 nm) and a thinner Si-O-Si matrix that allowed for rapid degradation within 120 hours in a physiological condition (**Figure 2-1b**). We loaded bMSN with a model STING agonist, bis-(3'-5')-cyclic dimeric adenosine monophosphate (CDA). Since CDA is a dicyclic nucleotide with anionic charges, the silica surface of bMSN was modified with amines (-NH2) to facilitate charge-mediated drug loading. The amine-modification changed the zeta potential of bMSN from -27.6 mV to 9.3 mV but did not affect the size of the nanoparticles (**Figure 2-1c,d**). The resulting bMSN-NH_2 (henceforth referred to as bMSN) was incubated at various concentrations with a fixed amount of

CDA (8 μg). After CDA was simply mixed and incubated with pre-formed bMSN for 1 hr, we observed > 90% loading of 8 μg CDA into 25 μg of bMSN (**Figure 2-1e**), indicating drug loading of ~290 μg per mg of bMSN (CDA@bMSN). CDA was released from CDA@bMSN within 1 hr at pH 7.0 (**Figure 2-1f**). However, when incubated at a slightly acidic condition of pH 6.0 mimicking the conditions within the tumor microenvironment (TME) (*80*), we observed slower release of CDA (**Figure 2-1f**).

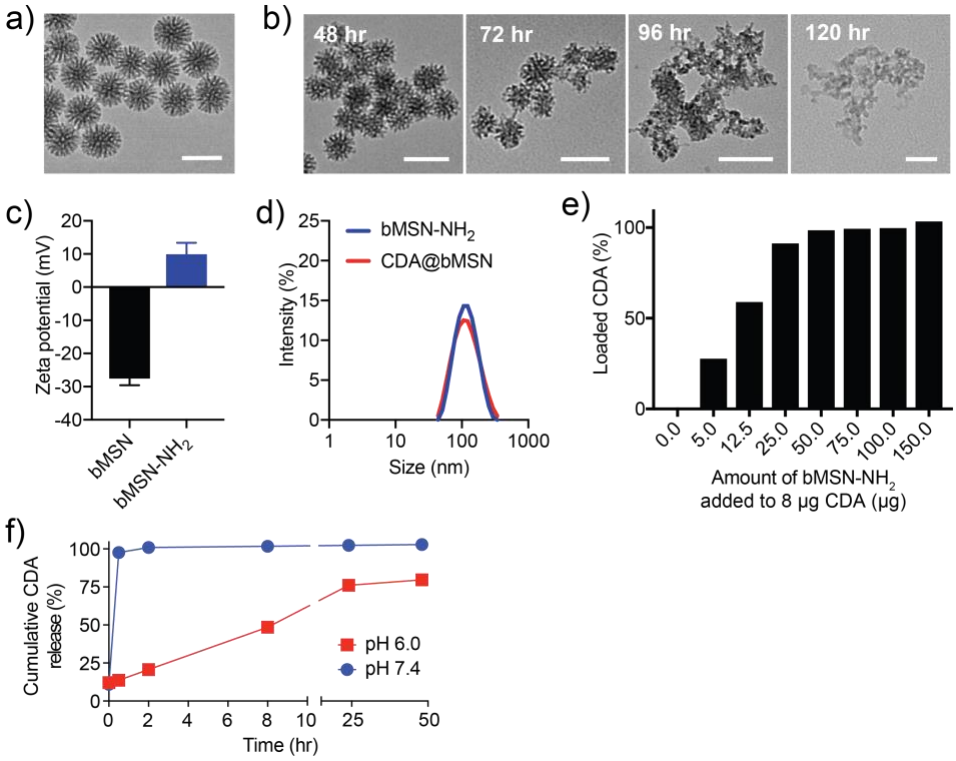

Figure 2-1 Cellular delivery of STING agonists using bMSN. (**a**) TEM image of bMSN. (**b**) Degradation of bMSN in a physiological condition (Krebs-Henseleit solution at 37 °C). (**c**) Surface charge and (**d**) hydrodynamic size of bMSN measured before and after amine-modification using DLS. Particles were transferred to water for measurements. (**e**) CDA-loading capacity of bMSN. (**f**) CDA Release profiles in different pH conditions. All data are presented as mean ± SEM, showing representative results from two independent studies with n = 3, with the exception of (**e**) with n = 1. Scale bars in (**a**) and (**b**) = 100 nm.

Next, we examined cellular uptake of CDA@bMSN using mouse bone marrow-derived dendritic cells (BMDCs), as a widely used surrogate for APCs. BMDCs incubated with free fluorophore-tagged CDA for 6 hr showed a minimal increase in the fluorescence signal (**Figure 2-2a**), whereas BMDCs incubated with CDA@bMSN exhibited markedly enhanced CDA signal

(**Figure 2-2a**). Similarly, confocal microscopy revealed that BMDCs and B16F10 melanoma cells incubated with fluorophore-tagged CDA@bMSN exhibited much stronger cytosolic fluorescence signal, compared with minimal signal in cells treated with free CDA (**Figure 2-2b, Figure 2-2c**), demonstrating efficient bMSN-mediated cytosolic delivery of STING agonist.

In addition, CDA@bMSN treatment led to robust BMDC activation, as evidenced by significantly increased expression of CD40 ($P < 0.0001$) and CD86 ($P < 0.001$), compared with free CDA treatment (**Figure 2-2d**), likely due to the increased cellular uptake of CDA@bMSN. Blank bMSN slightly increased the expression level of CD40, but not CD86, indicating minimal immune activation by the blank bMSN itself. Next, we used THP1-Blue ISG (human monocyte-derived cells expressing a reporter gene for STING activation) to study the effects of CDA@bMSN on STING activation. Compared with free CDA, CDA@bMSN induced significantly stronger STING activation even at 12.5 μg/ml dose of CDA ($P < 0.0001$, **Figure 2-2e**), indicating amplification STING activation by bMSN-mediated delivery of CDA. Notably, both THP1-Blue ISG cells and primary CD8+ T cells incubated with either free CDA or CDA@bMSN exhibited similar levels of viability (**Figure 2-2f, Figure 2-2g**), showing biocompatibility of CDA@bMSN. We have also previously reported biological safety of the bMSN platform (*79*). Taken together, compared with free soluble CDA, CDA@bMSN significantly improved cellular uptake of CDA and amplified STING activation, without negatively affecting cytotoxicity.

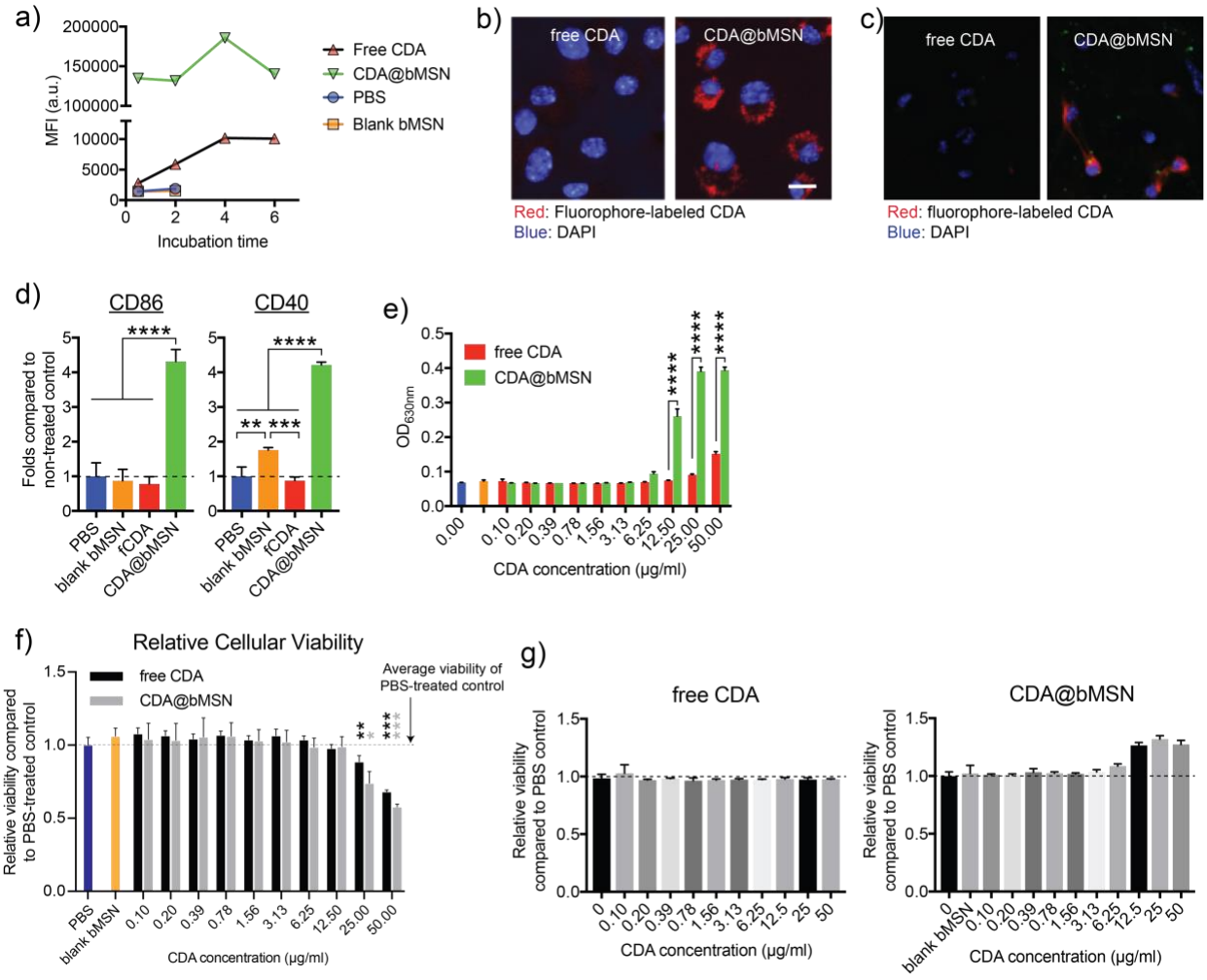

Figure 2-2. Effects of bMSN-mediated CDA delivery in vitro. (**a-c**) Uptake of CDA by BMDCs assessed in vitro with (**a**) flow cytometry and (**b,c**) confocal microscopy. (**d**) Activation of BMDCs measured by flow cytometry after 4 hr of incubation. (**e**) STING activation of human monocyte-derived THP1-Blue ISG cells measured after overnight incubation. Relative viability of THP1-Blue ISG cells (**f**) and CD8+ T cells (**g**) after STING agonist treatment, measured using cell counting kit-8. All data are presented as mean ± SEM, showing representative results from two independent studies with n = 3, Scale bars in (**b,c**) = 5 μm. **p < 0.01, ***p < 0.001, ****p < 0.0001 analyzed by one-way or two-way ANOVA with Tukey's HSD multiple comparison post hoc test.

We examined secretion of cytokines and chemokines from BMDCs treated with CDA formulations. In line with the enhanced uptake of CDA and activation of BMDCs (**Figure 2-2a-d**), CDA@bMSN treatment significantly increased the release of IL-6, IL-12p40, IFN-β, CXCL10, CCL2, CCL3, and CCL5 from BMDCs, compared with free CDA ($P < 0.0001$, **Figure 2-3a**). Although tumor-infiltrating immune cells are known as the major cell types that are activated by

STING agonists and initiate anti-tumor immune response, tumor cells also have been shown to respond to STING agonists (*81, 82*). We examined whether CDA treatment can promote cytokine and chemokine production from melanoma cell lines, B16F10 and B16F10OVA. Tumor cells incubated with free CDA did not release any detectable levels of cytokines or chemokines; however, CDA@bMSN treatment led to significantly amplified secretion of CXCL10 and CCL5 from B16F10 cells and CCL2 and CCL5 from B16F10OVA cells ($P < 0.01$ for CCL2 and $P < 0.0001$ for the others, **Figure 2-3b**). In order to confirm STING-dependent activation, we pre-treated BMDCs with a STING inhibitor, C-178, followed by incubation with CDA formulations. Pre-treatment with C-178 significantly decreased the secretion of cytokines and chemokines induced by both free CDA and CDA@bMSN (**Figure 2-3c**), showing that CDA-mediated immune activation is indeed dependent on the STING pathway.

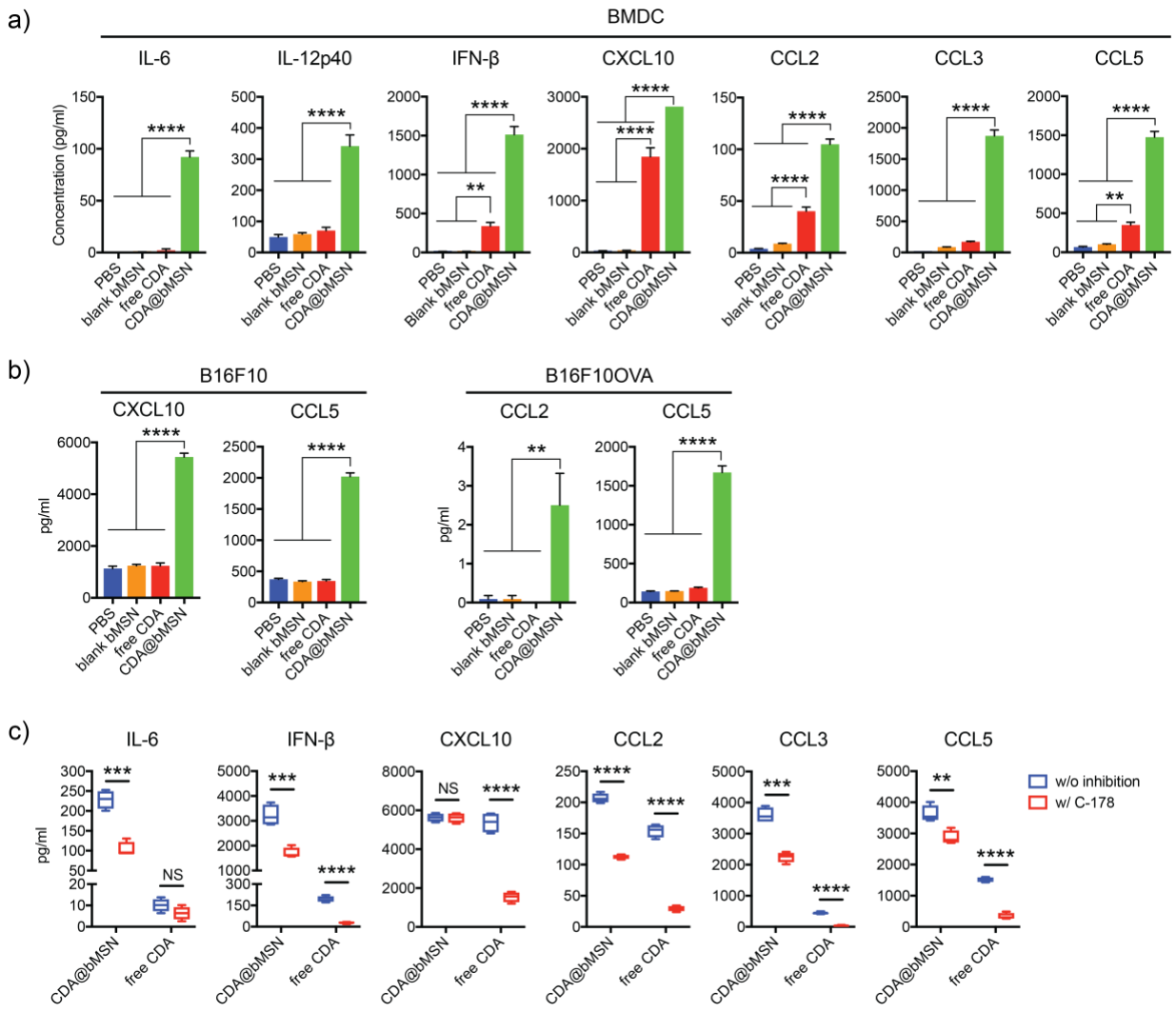

Figure 2-3. CDA@bMSN promotes cytokine and chemokine release from BMDCs and tumor cells. (a) Mouse BMDCs and (**b**) mouse melanoma cell lines, B16F10 and B16F10OVA, were treated with 10 μg/ml of CDA for 6 hr in vitro. Supernatants were assessed by ELISA for cytokines and chemokines. (**c**) BMDCs pre-treated for 1 hr with 0.5 μM of a STING inhibitor, C-178, followed by treatment with 10 μg/ml of CDA for 6 hr. Data are presented as mean ± SEM, showing representative results from two independent studies with n = 3-4. **p < 0.01, ***p < 0.001, ****p < 0.0001 analyzed by analyzed by one-way or two-way ANOVA with Tukey's HSD multiple comparison post hoc test.

Next, anti-tumor effects of CDA@bMSN was investigated in a murine melanoma model of B16F10OVA. C57BL/6 mice were injected subcutaneously with $3x10^5$ B16F10OVA cells on the right-side flank. When tumors reached > 100 mm^3 on day 6 after tumor inoculation, we performed a single intratumoral administration of 2 μg CDA in either bMSN or free form (**Figure 2-4a**). Interestingly, both free CDA and CDA@bMSN treatments were able to induce regression

of established tumors with minimal tumor volume by day 14 (**Figure 2-4b**). However, 50% of mice in the free CDA-treated group quickly relapsed and had to be euthanized by day 30. In stark contrast, 100% mice in the CDA@bMSN treatment group remained tumor free for the duration of the study (**Figure 2-4c**). To understand the differences between the free CDA and CDA@bMSN treatment groups, we analyzed the levels of cytokines and chemokines as well as various immune cell subsets. In line with our *in vitro* results (Figure 3), after 3 hours of intratumoral administration, CDA@bMSN induced strong release of IFN-β, CXCL10, CCL2, and CCL5 in TME and serum (**Figure 2-4d,e**). Notably, even after 24 hr of administration, higher levels of CXCL10 and CCL2 were detected within the TME for the CDA@bMSN group, compared with free CDA group ($P < 0.05$, **Figure 2-4d**), suggesting sustained immune activation mediated by bMSN.

We also investigated the effects of CDA treatment on the innate and adaptive immune responses. Intratumoral administration of CDA@bMSN led to robust activation of DCs within the TME, as evidenced by upregulation of CD86 within 3 hr and CD40 within 24 hr post treatment (**Figure 2-4f**). There was a trend for higher expression levels of CD86 and CD40 on DCs after 24 hr of treatment with CDA@bMSN, compared with free CDA (**Figure 2-4f**) although their differences were not statistically significant. While free CDA treatment induced transient upregulation and down-regulation of CD107α, a degranulation marker, on intratumoral NK cells, CDA@bMSN treatment led to sustained expression of CD107α on intratumoral NK cells for up to 24 hr ($P < 0.5$, **Figure 2-4g**). By 24 hr of CDA@bMSN treatment, we also observed activation of NK cells in the circulation, as shown by increased levels of CD107α and NKG2D (*83, 84*) (**Figure 2-4h**).

Intratumoral injection of free CDA significantly decreased the number of CD8+ T cells within the tumor by 24 hr post CDA injection, compared with no treatment group ($P < 0.05$, **Figure**

2-4i). This is in line with the literature reporting decreased tumor-infiltration of lymphocytes after intratumoral administration of free STING agonist (*71, 81*). In contrast, intratumoral CDA@bMSN treatment resulted in significantly higher number of intratumoral CD8+ T cells at 24 hr time point, compared with free CDA ($P < 0.01$, **Figure 2-4h**), suggesting that bMSN-mediated CDA delivery reversed the decrease in intratumoral infiltration of CD8+ T cells associated with free CDA (*71, 81*). CDA@bMSN treatment also significantly increased the expression of a degranulation marker, CD107α, on intratumoral CD8+ T cells by 24 hr, compared with untreated control ($P < 0.05$, **Figure 2-4j**). Overall, these results suggest that bMSN-mediated delivery of CDA amplifies the magnitude and duration of cytokine and chemokine release within TME and potently activates intratumoral DCs, NK cells, and CD8+ T cells, thus leading to regression of established tumors.

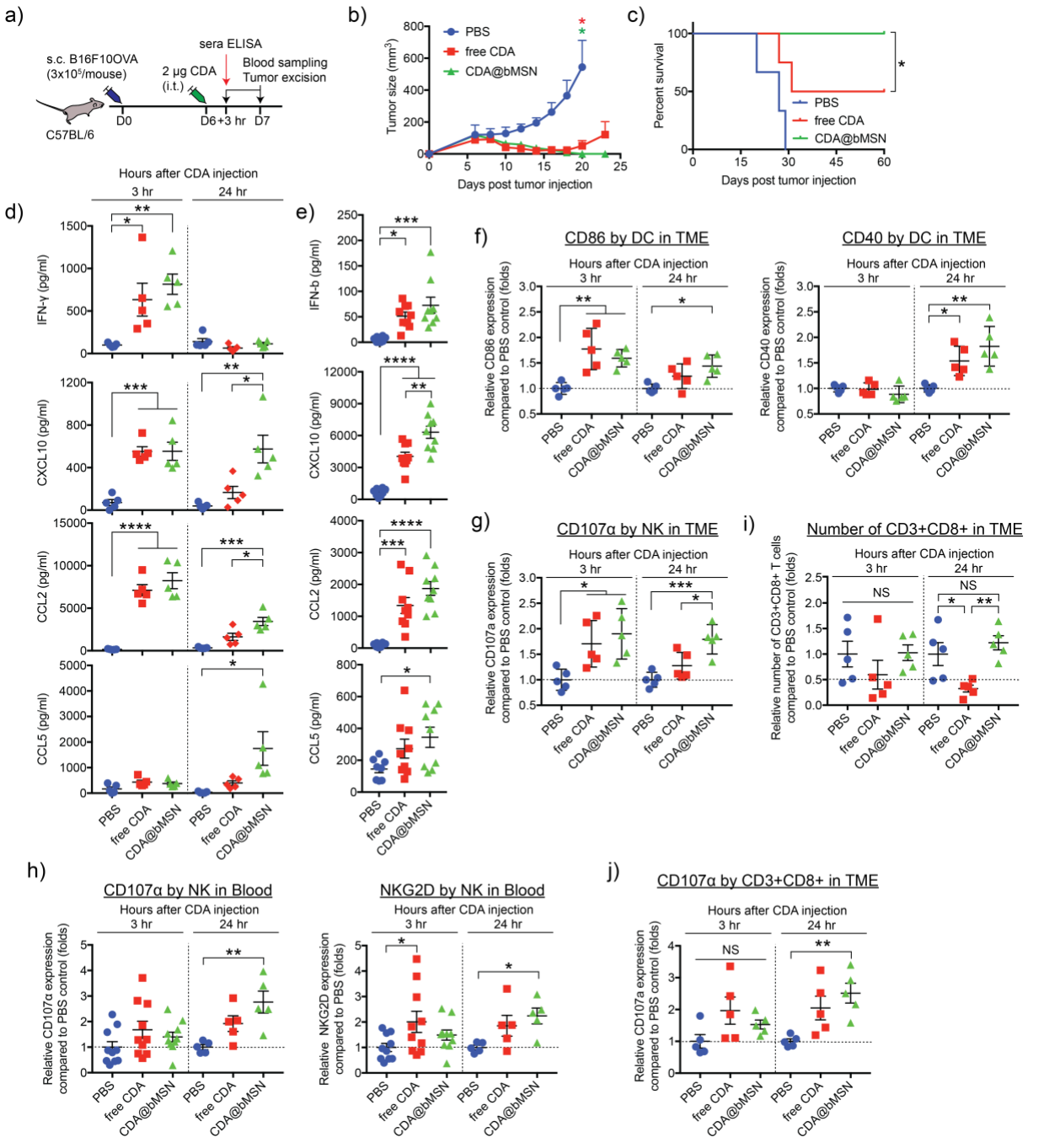

Figure 2-4. A single intratumoral treatment with CDA@bMSN exerts potent anti-tumor efficacy. (**a**) C57BL/6 mice were subcutaneously injected with 3x105 B16F10OVA cells on the right-side flank. After 6 days, each mouse received intratumoral injection of 2 μg CDA as a soluble or bMSN formulations. After 3 or 24 hr, blood sampling and tumor excision were performed. (**b**) Tumor growth curves and (**c**) animal survival are shown. (**d**) Cytokine levels within tumor tissues or (**e**) sera were measured by ELISA after 3 and 24 hr or 3 hr of CDA injection, respectively. Flow cytometric analyses were performed to examine (**f**) CD86 and CD40 expression on DCs, (**g,h**) CD107α expression on NK cells and (**i**) the number of CD8+ T cells within the B16F10OVA TME for (**f,g,i**) and blood for (**h**). Data are presented as mean ± SEM, showing representative results from two independent studies with n = 3-4 for (**b-c**) and n = 5 for (**d-j**). *$p < 0.05$, **$p < 0.01$, ***$p < 0.001$, ****$p < 0.0001$ analyzed by analyzed by one-way or two-way ANOVA with Tukey's HSD multiple comparison post hoc test. Animal survival curves were analyzed by the log-rank (Mantel−Cox) test.

Having observed strong anti-tumor efficacy of CDA@bMSN, we evaluated CDA@bMSN in the setting of established B16F10 melanoma. As B16F10 is a poorly immunogenic, highly aggressive tumor model, we increased the dose of CDA@bMSN to 5 µg. C57BL/6 mice were inoculated s.c. with $3x10^5$ B16F10 cells. When tumors were > 50 mm^3 on day 6, we performed a single intratumoral administration of CDA either in a soluble or bMSN forms (**Figure 2-5a**). Whereas mice in the untreated control group quickly succumbed to B16F10 tumor with a median survival of 12 days, free CDA treatment slowed the B16F10 tumor growth and extended the median survival to 18 days (p < 0.01, **Figure 2-5b,c**). Compared with free CDA group, CDA@bMSN treatment further inhibited B16F10 tumor growth (p < 0.01, **Figure 2-5b**) and extended the median survival to 24 days (p < 0.05, **Figure 2-5c**), thus highlighting the therapeutic potential of CDA@bMSN.

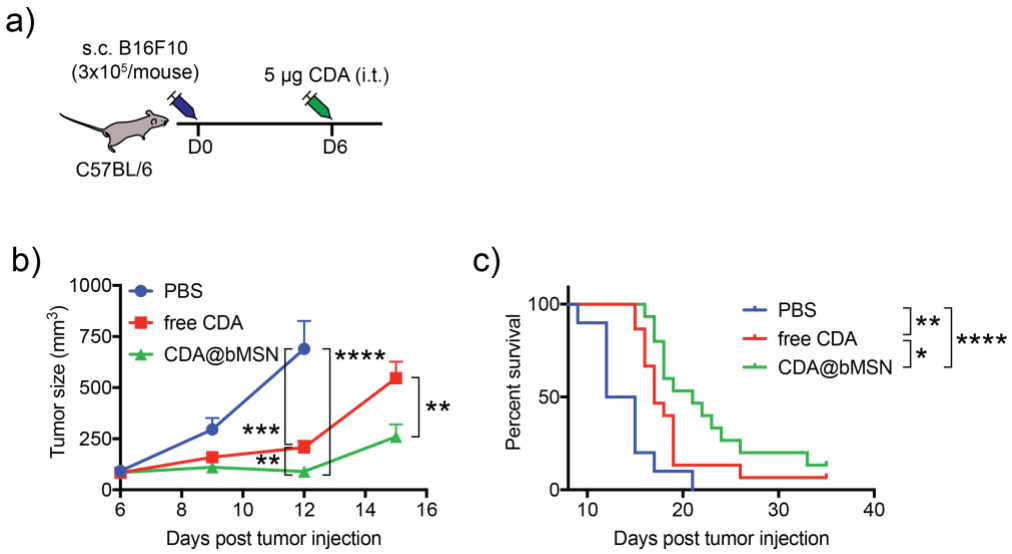

Figure 2-5. A single intratumoral treatment with CDA@bMSN exerts potent anti-tumor efficacy in B16F10 mouse melanoma model. (a) C57BL/6 mice were subcutaneously injected with 3x105 B16F10 cells on the right-side flank. After 6 days, each mouse received intratumoral injection of 5 µg free CDA or CDA@bMSN. (**b**) Tumor growth curves and (**c**) animal survival curves are shown. Data are presented as mean ± SEM, pooled from two independent studies. *p < 0.05, **p < 0.01, ***p < 0.001, ****p < 0.0001 analyzed by analyzed by two-way ANOVA with Tukey's HSD multiple comparison post hoc test. Animal survival curves were analyzed by the log-rank (Mantel−Cox) test.

2.5. Conclusion

In summary, we have developed bMSN for efficient cytosolic delivery of STING agonists. While previous studies have reported various STING agonist-loaded NP systems (*85-89*) including liposomes and polymeric NPs, their fabrication and drug loading procedures are often complicated with multiple synthesis and separation steps, and many of these NP platforms have not been clinically tested. On the other hand, silica-based NPs offer a promising platform with biocompatibility, facile manufacturing process, and clinical safety (*72, 73, 90*). Notably, we have achieved > 90% loading of CDA into bMSN simply by admixing CDA with pre-formed bMSN for 1 hr. We show that bMSN carrying STING agonists improves STING activation by DCs and tumor cells and elicits potent innate and adaptive immune responses in vivo, leading to strong anti-tumor efficacy and prolonged animal survival in murine models of melanoma. While the mechanisms underlying bMSN-mediated STING activation and subsequent cascades of innate and adaptive immune responses remain to be elucidated, our results suggest that bMSN is a biodegradable and biocompatible carrier for efficient delivery of STING agonists. It is also notable that the typical dose of STING agonists reported in the literature ranges from 10-240 μg, often used in combination with chemotherapeutic or immunotherapeutic agents (*66, 71, 91-95*). In contrast, we report that a single injection of CDA@bMSN at the dose of 5 μg or less exerted potent anti-tumor efficacy, thus highlighting the dose-sparing effect of the bMSN platform. Recent advances in cancer immunotherapy have generated intense research interest in drug delivery vehicles for improving immune activation (*20, 26, 96, 97*), and our bMSN system may offer a promising platform for delivery of immunomodulatory agents for cancer immunotherapy.

Nevertheless, as our current studies have mainly focused on the acute responses mounted by innate immune cells after intratumoral CDA injection, our future studies will address the effects

of bMSN-based CDA delivery on adaptive immune responses and examine systemic delivery of CDA@bMSN. Further research is warranted to optimize the bMSN platform for the delivery of STING agonists in the context of combination cancer immunotherapy.

CHAPTER III. Personalized Combination Nano-immunotherapy for Robust Induction and Tumor Infiltration of CD8+ T Cells

3.1. Abstract

Identification of tumor-specific mutations, called neoantigens, offers new exciting opportunities for personalized cancer immunotherapy. However, it remains challenging to achieve robust induction of neoantigen-specific T cells and drive their infiltration into the tumor microenvironment (TME). Here, we have developed a novel polyethyleneimine (PEI)-based personalized vaccine platform carrying neoantigen peptides and CpG adjuvants in a compact nanoparticle (NP) for their spatio-temporally concerted delivery. PEI NP vaccine significantly enhanced activation and antigen cross-presentation of dendritic cells, resulting in strong priming of neoantigen-specific CD8+ T cells with the frequency in the systemic circulation reaching as high as 23 ± 7% after a single subcutaneous administration. However, activated CD8+ T cells in circulation exhibited limited tumor infiltration, leading to poor anti-tumor efficacy. Notably, local administration of stimulator of interferon genes (STING) agonist promoted tumor infiltration of vaccine-primed CD8+ T cells, thereby overcoming one of the major challenges in achieving strong anti-tumor efficacy with cancer vaccination. PEI NP vaccination combined with STING agonist therapy eliminated tumors in murine models of MC-38 colon carcinoma and B16F10 melanoma and established long-term immunological memory. Our approach provides a novel therapeutic strategy based on combination nano-immunotherapy for personalized cancer immunotherapy.

3.2. Introduction

Recent advances in genomics and proteomics are shedding new light on the tumor mutanome, revealing that every tumor has a unique set of driver and passenger mutations (*17-19*). Expression of neoantigens is, by definition, restricted to tumor cells as opposed to tumor-associated antigens with shared expression among healthy and tumor cells. Thus, immunotherapy directed against neoantigens may allow for specific immunological targeting of tumor cells without self-tolerance. It has been the motive for an avalanche of cancer vaccine studies in the recent years.

In 2017, first-in-man phase I clinical trials were reported in which patients with advanced melanoma were treated with neoantigen peptide vaccines following surgical resection of the tumour (*24*). Each of six patients received seven doses of 20 different neoantigen peptides mixed with poly(I:C) stabilized with poly-L-lysine (poly-ICLC) adjuvant(*24*); neoantigen vaccination induced CD4+ and CD8+ T cells specific for 58 (60%) and 15 (16%) of the 97 unique neoantigens identified across the six patients. Four patients showed no recurrence at 25 months after vaccination, and two patients had complete tumour regression after co-treatment with the checkpoint blockade agent anti-PD-1. Along with another phase I trial with neoantigen encoding mRNA vaccine detailed below(*98*), these seminal trials showed that personalized neoantigen vaccination, especially in combination with immune checkpoint blockade, can unleash the full cytotoxic potential of neoantigen-specific T cells to kill tumours with limited adverse effects, and underscored the clinical applicability of personalized neoantigen vaccines as a new therapeutic strategy for long-term protection against tumour relapse and metastasis.

The tantalizing results of neoantigen vaccination galvanized the personalized immunotherapy field; nevertheless, producing potent anti-tumour neoantigens therapies in a safe,

effective, and personalized process is challenging: efficient delivery strategies are needed to enhance transport of neoantigens together with adjuvant molecules to lymph nodes; the amino acid composition of neoantigen peptides can have significant effects on their isoelectric properties, meaning that the administration of a cocktail of soluble peptides can lead to their precipitation, deposition in off-target tissues, or dissemination through the systemic circulation without preferential targeting to lymphoid tissues. Issues in vaccine delivery can result in only a minor fraction of the injected peptides reaching the target lymphoid tissues, reducing vaccine efficacy. Also, even if vaccination generates sufficient anti-tumor CD8+ T cells in the systemic circulation, intratumoral trafficking of CD8+ T cells is often limited, thus resulting in poor anti-tumor effects. Notably, tumor infiltration of CD8+ T cells is correlated with patient prognosis, as shown by recent retrospective analyses of clinical cases (*31, 99-101*). Also, tumors with sparse T cell infiltration are less responsive to immune checkpoint blockade (ICB) therapies designed to reinvigorate tumor-infiltrating lymphocytes (*102*). Such immunologically "cold" tumors have various immunosuppressive mechanisms to exclude or reprogram immune cells, thus shaping the tumor microenvironment (TME) to evade the immune surveillance (*2, 103*). While chemotherapy (*104, 105*), oncolytic virus (*106*), and anti-angiogenic agents (*107*) have been applied to reverse immunosuppression and convert non-immunogenic "cold" tumors into T cell-inflamed "hot" tumors, it remains to be seen how to combine them effectively with cancer vaccination.

Therefore, current personalized cancer vaccines using neoantigen peptides face two major problems. 1) Neoantigen peptides delivered in soluble forms generate suboptimal immune potency. 2) Many tumors release insufficient levels of chemokines to attract circulating CD8+ T cells to the site of tumor. Thus, new approaches are needed to promote the induction of neoantigen-specific T cells and increase their tumor infiltration.

Here, to overcome these urgent challenges, we have developed a facile personalized nanoparticle vaccine using polyethyleneimine (PEI) that offers versatile functionality for modular incorporation of neoantigens and simple electrostatic assembly of CpG adjuvant. PEI NP vaccine significantly enhanced cellular uptake of antigens and adjuvant molecules to promote activation and antigen cross-presentation of dendritic cells (DCs), resulting in robust priming of neoantigen-specific CD8+ T cell. However, despite high frequency of anti-tumor CD8+ T cells in the systemic circulation, we observed weak anti-tumor effect due to limited intratumoral trafficking of activated CD8+ T cells. STING is a pattern recognition receptor (PRR) that triggers NF-κB and IRF3 pathways, leading to strong type I IFN responses (*108*), and recent studies have reported promising therapeutic efficacy of STING agonists for cancer treatment (*66*, *71*). Here, we have demonstrated that intratumoral administration of STING agonist induced robust secretion of cytokines and chemokines that promoted T cell trafficking into the TME. When combined with PEI NP vaccination, treatment with STING agonist led to strong recruitment of vaccine-primed, neoantigen-specific CD8+ T cells into the TME, leading to significantly improved anti-tumor efficacy, compared to either treatment alone. These studies present a new combination nano-immunotherapy for inducing neoantigen-specific T cells and their tumor infiltration for achieving potent anti-tumor efficacy.

Specifically, we prepared personalized NP vaccine based on PEI by taking advantage of its versatile functionality for chemical conjugation and electrostatic complexation. PEI was grafted with PEG for enhancing colloidal stability and biocompatibility, followed by conjugation with CSS-modified neoantigen peptides via reduction sensitive disulfide bond. Because of the strong cationic characteristic of PEI, the simple mixture of PEI conjugates with anionic CpG formed a nanoscale condensate by electrostatic complexation. (**Figure 3-1a**). CpG was employed as an

adjuvant not only because of its strong anionic property but also for its potent immunostimulatory property (*109*).

3.3. Materials and Methods

Synthesis of PEI conjugates and CpG nanocomplex

PEI-PEG was prepared using branched PEI (Sigma-Aldrich, molecular weight ~25,000) and methoxy poly(ethyleneglycol) propionic acid N-hydroxysuccinimide (Nanocs, molecular weight 5000) as reported previously 41. For PEI-PEG/CSS-antigen, PEI-PEG was dissolved in DMSO and added with 3-(2-Pyridyldithio)propionic acid N-hydroxysuccinimide ester (SPDP, Sigma-Aldrich) to create thiol-reactive disulfide bond. After stirring for 3h, the mixture was reacted with CSS-antigen overnight, followed by dialysis-purification using Amicon ultra 10 kDa MW cutoff centrifugal filters. CpG nanocomplex was formed by vigorously mixing CpG (CpG 1826, Integrated DNA Technology) and PEI conjugate in PBS at the weight ratio 0.5, 1, 2, or 3.

Animal studies

Animals were cared for following federal, state and local guidelines. All experiments performed on animals were in accordance with and approved by the Institutional Animal Care and Use Committee (IACUC) at the University of Michigan, Ann Arbor. 5-6 weeks old female C57BL/6 mice were purchased from Jackson Laboratories. Tumor cells (6x105 MC-38 cells per mouse (1.2x106 for re-challenge study) and 3x105 B16F10 cells per mouse) were injected s.c. on the right flank of each mouse. Vaccines were administered s.c. at the tail-base on indicated days. Four days after the vaccination, CDA (dissolved in PBS; 0.5 μg for the MC-38 model and 5 μg for

the B16F10 model) was injected into tumors on the indicated days. Tumor sizes were measured using a caliper.

In vitro BMDC studies

BMDCs were collected from hind femurs of C57BL/6 mice, cultured with media supplemented with GM-CSF for 8-10 days as previously reported 42. For the analysis of cytokine secretion and proliferation by PEI NP, immature BMDCs were treated with free PEI-PEG/CSS-Adpgk (PEI conjugate, 3 μg/ml), free CpG (1 μg/ml), or PEI NPs formulated at different weight ratios of PEI conjugate/CpG (1 μg/ml CpG and the respective amount of PEI conjugate). Cells were washed after 2 h, supplemented with fresh media, and further incubated for 24 h for the detection of IL-12p70 in cell culture media using ELISA, while BMDC proliferation was measured using a cell counting kit (CCK-8; Dojindo Molecular Technologies, Inc.).

For studying CpG uptake by BMDCs, 5' phosphate group of CpG was tethered with ethylenediamine and subsequently labeled with Alexa Fluor® 647 NHS Ester (AF647-NHS, Invitrogen) as described before.41 In parallel, PEI conjugates were labeled with Alexa Fluor® 488 NHS Ester (AF488-NHS, Invitrogen). BMDCs were then incubated with soluble formulation or PEI NPs at dose of 10 μg/ml CpG-AF467 and 20 μg/ml PEI conjugates-AF488 (equivalent of 10 μg/ml for free Adpgk). At the indicated time points, cells were collected, washed with FACS buffer (1% BSA in PBS), and then subjected to flow cytometry for measuring fluorescence signals. To visualize cellular localization, BMDCs were grown onto 12 mm glass coverslips in 24 well plates at a density of 5 × 105 cells/well and treated with samples as above for 24 h. Cells were further incubated with Hoechst 33342 (5 μg/ml, Invitrogen) and Lysotracker Red DND-99 (100 nM, Invitrogen) for 30 min for the staining of nuclei and endolysosomes, respectively. Then, cells were

fixed with 4% formaldehyde in PBS and mounted on slide glass using ProLong™ Diamond Antifade Mountant (Invitrogen) for confocal microscopy (Nikon A1Rsi).

For assessing activation and antigen cross-presentation, PEI NPs were constructed using PEI-PEG/CSS-SIINFEKL and CpG. BMDCs were incubated for 24 h with either soluble or PEI NP formulation of SIINFEKL and CpG (2 μg/ml SIINFEKL and 1 μg/ml CpG). Cells were then stained with antibody-fluorophore conjugates including CD40-APC (Invitrogen), CD86-PE/Cy7 (BD Biosciences), and SIINFEKL/H-2kb-PE (Invitrogen) for 30 min at room temperature. Cells were washed with FACS buffer and analyzed using flow cytometry.

For the analysis of cytokine secretion by BMDCs in response to CDA treatment, BMDCs were seeded at a density of 105 cells/well in a 96-well tissue culture plate and incubated overnight at 37 oC with 5% CO2. Cells were washed with PBS twice, and then added with 5 μg of CDA in 200 μl of fresh culture media. Culture media were retrieved after 6 hrs for ELISA assay.

Analyses of CD8+ T cells and cytokines in blood and tumor

Blood was collected at the indicated time points by submandibular bleeding, treated with ACS lysing buffer (Gibco), and washed with PBS to obtain PBMCs. For TME analysis, tumor tissues were excised from tumor-bearing mice, cut into small pieces (1-2 mm) with scissors, and treated with 1 mg/ml of collagenase A (Sigma-Aldrich) and 100 IU of DNase I (Sigma-Aldrich) for 30 min at 37 oC with continuous shaking. Samples were placed on top of 40 μm strainers and mashed through with a plunger, followed by centrifugation at 1000 g for 5 min. The cell pellet was resuspended and washed twice with PBS by centrifuging at 1500 g for 3 min. PBMCs and tumor cells were stained with a live/dead staining dye (eBioscience) and fluorophore-labeled antibodies including CD3-FITC (Biolegend), CD8-APC (BD Biosciences), and Adpgk tetramer-PE (NIH Tetramer Core Facility), fixed with 2% formaldehyde, and then suspended in FACS buffer for

flow cytometry. Blood sera and tumor tissue supernatants were separately collected for detection of cytokines using ELISA.

Statistical analysis

Statistical analysis was performed with Prism 7.0e (GraphPad Software). Statistical comparisons were performed using one-way ANOVA followed by Tukey's HSD multiple comparison post hoc test or two-way ANOVA followed by Sidak's multiple comparisons test, as indicated in the figure legends. Animal survival was analyzed by the log-rank (Mantel−Cox) test. Statistical significances are indicated as $*p < 0.05$, $**p < 0.01$, $***p < 0.001$, and $****p < 0.0001$.

3.4. Results and Discussion

PEI-PEG conjugate was synthesized by conjugating methoxy poly(ethyleneglycol) propionic acid N-hydroxysuccinimide (methoxy-PEG-NHS) to the primary amine of PEI. The stoichiometry PEI:PEG was controlled to 1:15, which was reported to diminish cytotoxicity of PEI.(*110, 111*) The conjugation was confirmed by quantification of free amine groups using 2,4,6-trinitrobenzene sulfonic acid (data not shown). To prepare a personalized NP vaccine, we employed Adpgk, a neo-epitope identified in MC-38 mouse colon adenocarcinoma.(*112*) PEI-PEG was incubated with 3-(2-pyridyldithio)propionic acid N-hydroxysuccinimide ester (SPDP) at room temperature (RT) for 3 hr for amine-to-sulfhydryl cross-linking, followed by overnight incubation with CSS-Adpgk. The resulting PEI-PEG/CSS-Adpgk conjugate was analyzed by gel permeation chromatography (GPC). As shown in **Figure 3-1b**, PEI-PEG/CSS-Adpgk had a major elution peak at 15 min; however, this particular peak was absent in the PEI-PEG conjugate, suggesting successful conjugation of Adpgk onto PEI-PEG. A brief treatment (~5 min) with dithiothreitol

(DTT) delayed the elution of PEI-PEG/CSS-Adpgk by ~0.9 min to be overlapped with the peak of free CSS-Adpgk + DTT sample (**Figure 3-1b**), indicating efficient release of CSS-Adpgk from PEI-PEG/CSS-Adpgk in a reduction sensitive manner.

Incubation of PEI-PEG/CSS-Adpgk with CpG led to the formation of nanoparticles (PEI NPs). Dynamic light scattering (DLS) measurement showed that the hydrodynamic size of PEI NPs decreased with an increasing feed amount of CpG, resulting in 40 – 50 nm Z-average size and 0.2 – 0.3 polydispersity index with the PEI conjugate/CpG weight ratio of > 1 (**Figure 3-1c**). In addition, the zeta potential values of PEI NPs were between those of free PEI conjugates and free CpG with almost neutral charges (**Figure 3-1d**), thus suggesting PEI/CpG charge compensation and PEG surface passivation. To assess the impact of complexation on immune activation by CpG, bone marrow-derived dendritic cells (BMDCs) were incubated with PEI NPs, and IL-12p70 secretion and cellular viability were measured. PEI NPs formulated at the PEI-conjugate/CpG weight ratio of 1 or 2 promoted higher amount of IL-12p70 and proliferation of BMDCs, compared to PBS and free CpG (**Figure 3-1e,f)**. In contrast, PEI conjugate alone did not induce the secretion of IL-12p70 nor proliferation of BMDCs, which indicated the crucial role of CpG in immune activation by PEI NPs. PEI NPs formulated at the PEI conjugate/CpG weight ratio of 2 exhibited relatively uniform size of 20 – 30 nm under transmission electron microscope (**Figure 3-1g**), which correlated well with the DLS measurements. Based on these results, PEI NPs formulated at the PEI conjugate/CpG weight ratio of 2 was chosen for the subsequent studies.

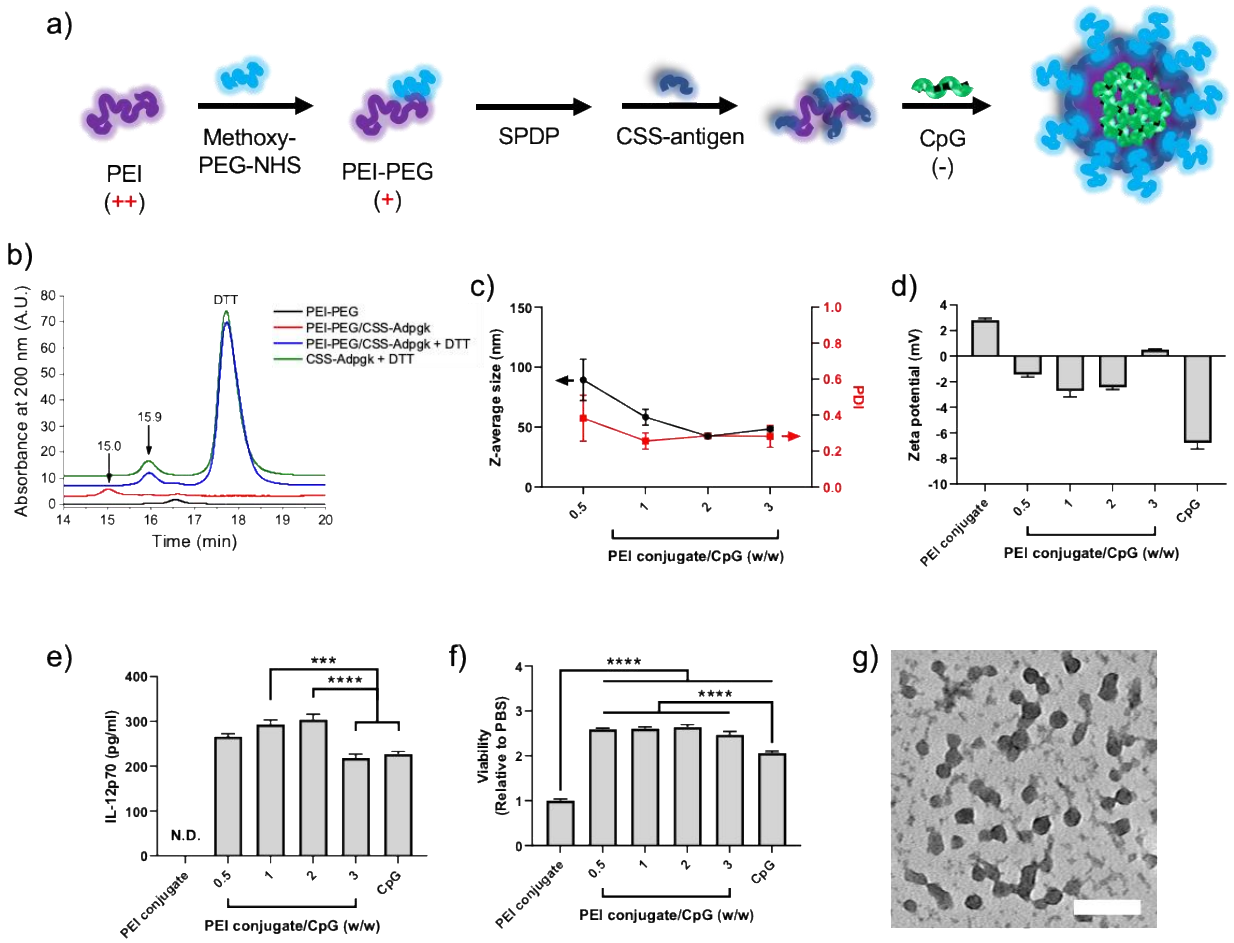

Figure 3-1. Synthesis and characterization of PEI NPs. (**a)** Schematic drawing of PEI nanoparticle vaccine formation. PEGylated PEI was conjugated with CSS-antigen via disulfide linkage and then condensated with CpG by electrostatic complexation to form PEI NPs. (**b)** GPC chromatograms, indicating the formation of PEI-PEG/CSS-Adpgk conjugate. (**c)** Hydrodynamic size and (**d)** surface charge of PEI NPs synthesized in different PEI conjugate:CpG weight ratios, as measured by DLS and zeta potential. (**e)** IL-12p70 secretion and (**f)** viability of mouse BMDC after incubation with PEI conjugate, CpG, or PEI NPs. (**g)** PEI NPs composed of a PEI conjugate:CpG weight ratio of 2:1 were imaged using TEM after 2% uranyl acetate staining. Scale bar = 100 nm. Data are presented as mean ± SEM. ***$p < 0.001$, ****$p < 0.0001$, analyzed by one-way ANOVA, followed by Tukey's HSD multiple comparison post hoc test.

Next, we investigated the impact of PEI NPs on DC uptake and subsequent activation and antigen presentation. Fluorophore-labeled CpG was formulated into PEI NPs for fluorescence-based analysis of NP uptake by BMDCs. PEI NPs promoted the uptake of CpG as early as after 2 h of incubation and showed > 30-fold increase over 72 hr, compared to free CpG (**Figure 3-2a**). The presence of Adpgk or CSS-Adpgk peptide admixed with CpG did not affect the uptake of

CpG, showing comparable levels with free CpG treatment alone. We further examined cellular uptake using confocal microscopy and confirmed that BMDCs incubated with PEI NPs displayed brighter CpG fluorescence within the endo-lysosomal compartments, compared with BMDCs incubated with free CpG (**Figure 3-2b**). Enhanced endo-lysosomal CpG delivery can potentiate engagement and activation of TLR9 receptors, which are located within the endo-lysosomes (*113*). We also investigated maturation and antigen presentation of BMDCs by employing SIINFEKL peptide, a MHC-I-restricted epitope of ovalbumin protein. BMDCs were incubated with PEI NPs consisting of PEI-PEG/CSS-SIINFEKL conjugates or control soluble formulations, followed by flow cytometric analysis. PEI NPs significantly increased the expression of co-stimulatory markers, including CD40 and CD86, on BMDCs (**Figure 3-2c**). Next, cells were stained with 25-D1.16 monoclonal antibody that recognizes SIINFEKL peptide complexed with H-2K^b MHC-I molecule (H-2K^b-SIINFEKL). Admixture of soluble SIINFEKL + CpG increased the expression of H-2K^b-SIINFEKL within 8 h, which rapidly declined to the baseline level after 24 h (**Figure 3-2d**). In contrast, PEI NPs significantly increased antigen presentation after 24 h, as shown by highly elevated levels of H-2K^b-SIINFEKL, compared to SIINFEKL + CpG ($p < 0.0001$, **Figure 3-2d**). Thus, despite the slow kinetics, PEI NPs significantly increased the cumulative extent of antigen presentation, compared with soluble formulations. Taken together, these results show that PEI NPs promote cellular uptake of antigen and CpG, leading to enhanced DC activation, maturation, and antigen presentation, compared with their free admixture.

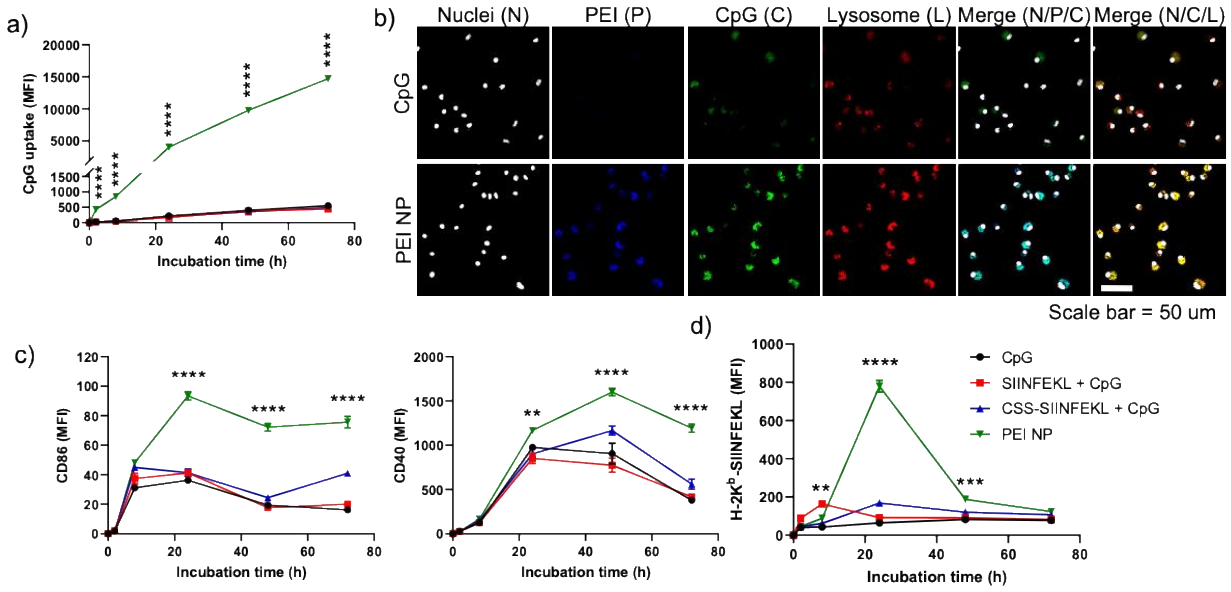

Figure 3-2. PEI NP promotes cellular uptake of antigen and CpG by DCs and improves DC maturation and antigen cross-presentation. a-b) BMDCs were incubated *in vitro* with fluorophore-labeled CpG in the indicated formulations, and fluorescence signals were measured using (**a)** flow cytometry and (**b)** confocal microscopy (scale bar = 50 µm). (**c-d)** BMDCs were incubated with CpG, SIINFEKL + CpG, CSS-SIINFEKL + CpG, or PEI NP, and (**c)** DC activation and (**d)** antigen presentation were measured by staining cells with **c)** anti-CD86 and anti-CD40 antibodies or (**d)** anti-H-2K^b-SIINFEKL antibody, respectively, followed by flow cytometry. Data are presented as mean ± SEM. *$p < 0.05$, **$p < 0.01$, ***$p < 0.001$, and ****$p < 0.0001$, analyzed by two-way ANOVA, followed by Tukey's HSD multiple comparison post hoc test. Asterisks represent comparison between PEI NP vs. Adpgk + CpG in (**a)**, and between PEI NP vs. SIINFEKL + CpG in (**c)** and (**d)**.

Next, we examined the immunogenicity and anti-tumor efficacy of PEI NPs *in vivo*. C57BL/6 mice were injected subcutaneously (s.c.) with $6x10^5$ MC-38 mouse colon carcinoma cells on the right flank on day 0. On day 7 when tumors were palpable, mice were vaccinated with various doses of PEI NPs composed of PEI-PEG/CSS-Adpgk conjugates and CpG (NP Vacc) via s.c. injection at tail base (**Figure 3-3a**). Soluble vaccines composed of free Adpgk and CpG (Sol Vacc) at the corresponding doses were used as control groups. To assess the priming of antigen-specific CD8+ T cells, peripheral blood mononuclear cells (PBMCs) were collected 7 days after the vaccination, and the frequencies of Adpgk-specific CD8+ T cells were measured by the tetramer assay. NP Vacc induced a dose-dependent increase in the frequency of Adpgk-specific CD8+ T cells in peripheral blood (**Figure 3-3b**). Notably, a single vaccination with NP Vacc at

1x dose (containing 10 µg of Adpgk peptide + 15 µg CpG) promoted clonal expansion of Adpgk-specific CD8+ cells as high as 23 ± 6.9% among all CD8+ T cells in PBMCs, representing 3-fold enhancement compared with 1x dose of Sol Vacc ($p < 0.05$, **Figure 3-3b**). However, despite this significant expansion of neoantigen-specific CD8+ T cells in the systemic circulation, we did not observe meaningful anti-tumor effect for any of the vaccine groups (**Figure 3-3c**). Since successful cancer immunotherapy requires sufficient infiltration of anti-tumor T cells into the TME (*114*) we analyzed the TME for the frequency of CD8+ T cells. The total number of tumor-infiltrating CD8+ T cells in the TME was similar for all the treatment groups (**Figure 3-3d**). Although NP Vacc induced a slight increase in the number of Adpgk-specific CD8+ T cells, compared with PBS (**Figure 3-3e**), there was no statistical difference between the NP Vacc and Sol Vacc groups. Taken together, NP Vacc effectively expanded tumor-specific CD8+ T cells in the systemic compartment, but their anti-tumor efficacy was limited, potentially due to poor tumor infiltration of activated T cells.

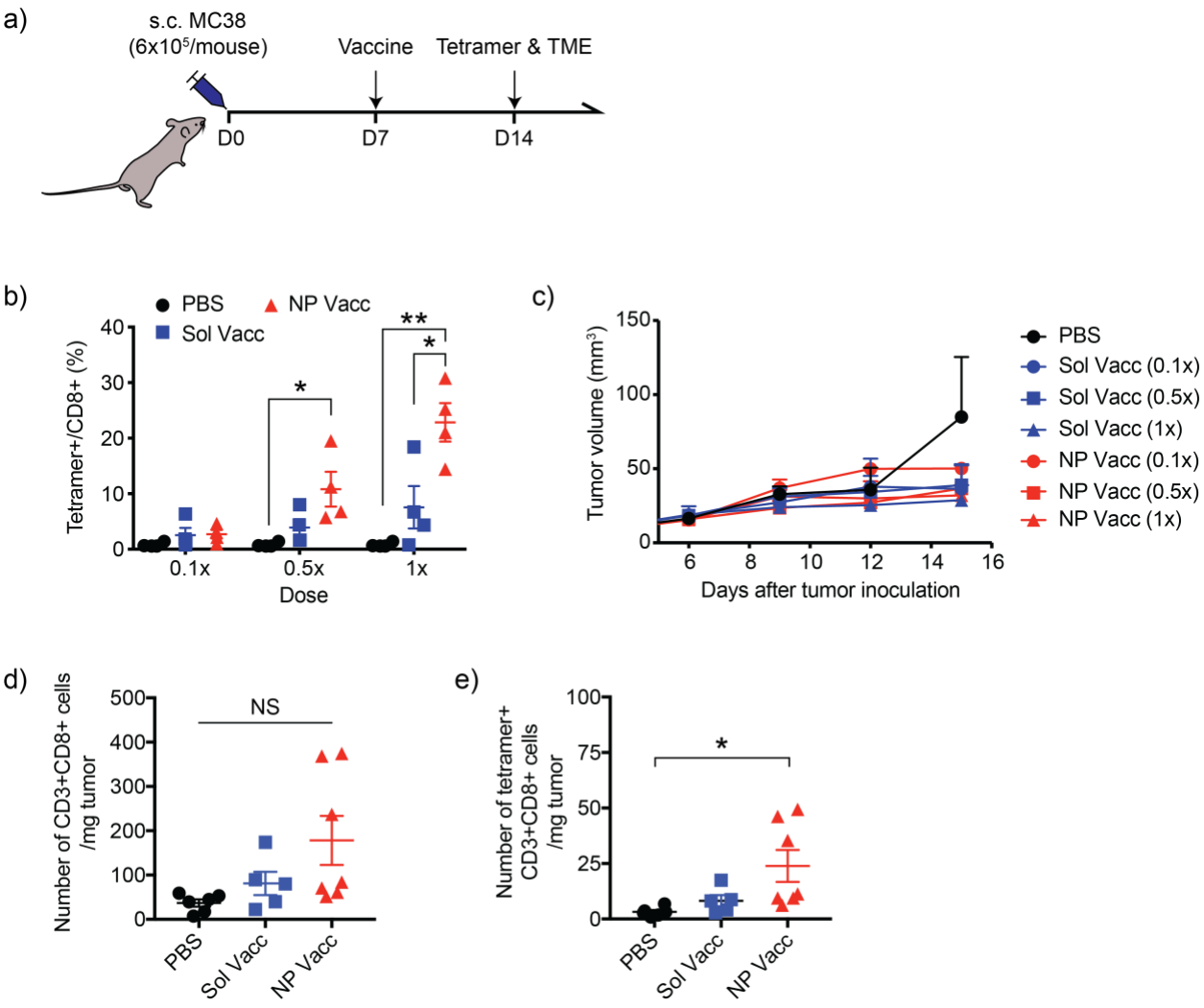

Figure 3-3. PEI NP elicits tumor-specific CD8+ T cell responses in the systemic compartment but fails to inhibit MC-38 tumor growth (**a)** Timeline of experiment. (**b)** C57BL/6 mice were inoculated at s.c. flank with $6x10^5$ MC-38 colon carcinoma cells on day 0 and vaccinated at s.c. tail base on day 7 with increasing doses of vaccines. Neoantigen-specific CD8+ T cell levels in blood circulation were quantified on day 14 by tetramer staining and flow cytometry. (**c)** Shown are the average MC-38 tumor growth curves. (**d-e)** Numbers of tumor-infiltrating (**d)** CD3+CD8+ T cells and (**e)** tetramer+CD3+CD8+ T cells were measured on day 14. Data are presented as mean ± SEM. *$p < 0.05$, **$p < 0.01$, and ****$p < 0.0001$, analyzed by one-way ANOVA, followed by Tukey's HSD multiple comparison post hoc test.

STING has been reported to promote tumor infiltration of peripheral T cells through the type I interferon (IFN) pathway (*115, 116*). Based on these studies, we investigated whether STING agonist can recruit vaccine-primed circulating CD8+ T cells into tumors. First, we examined whether cyclic-di-adenosine monophosphate (CDA), a potent STING agonist, can induce secretion of chemokines essential for recruitment of T cells. BMDCs treated with CDA *in*

vitro produced increased levels of CXCL10, CCL2, CCL3, and CCL5 (**Figure 3-4a**). When CDA was administered directly into MC-38 tumors *in vivo*, this led to increased serum concentrations of IFN-β, CXCL10, CCL2, and CCL5 in a dose-dependent manner (**Figure 3-4b**). Intratumoral (i.t.) administration of CDA at the dose range of 1-20 µg was well tolerated, and mice did not show any abnormal change in body weight (**Figure 3-4c**).

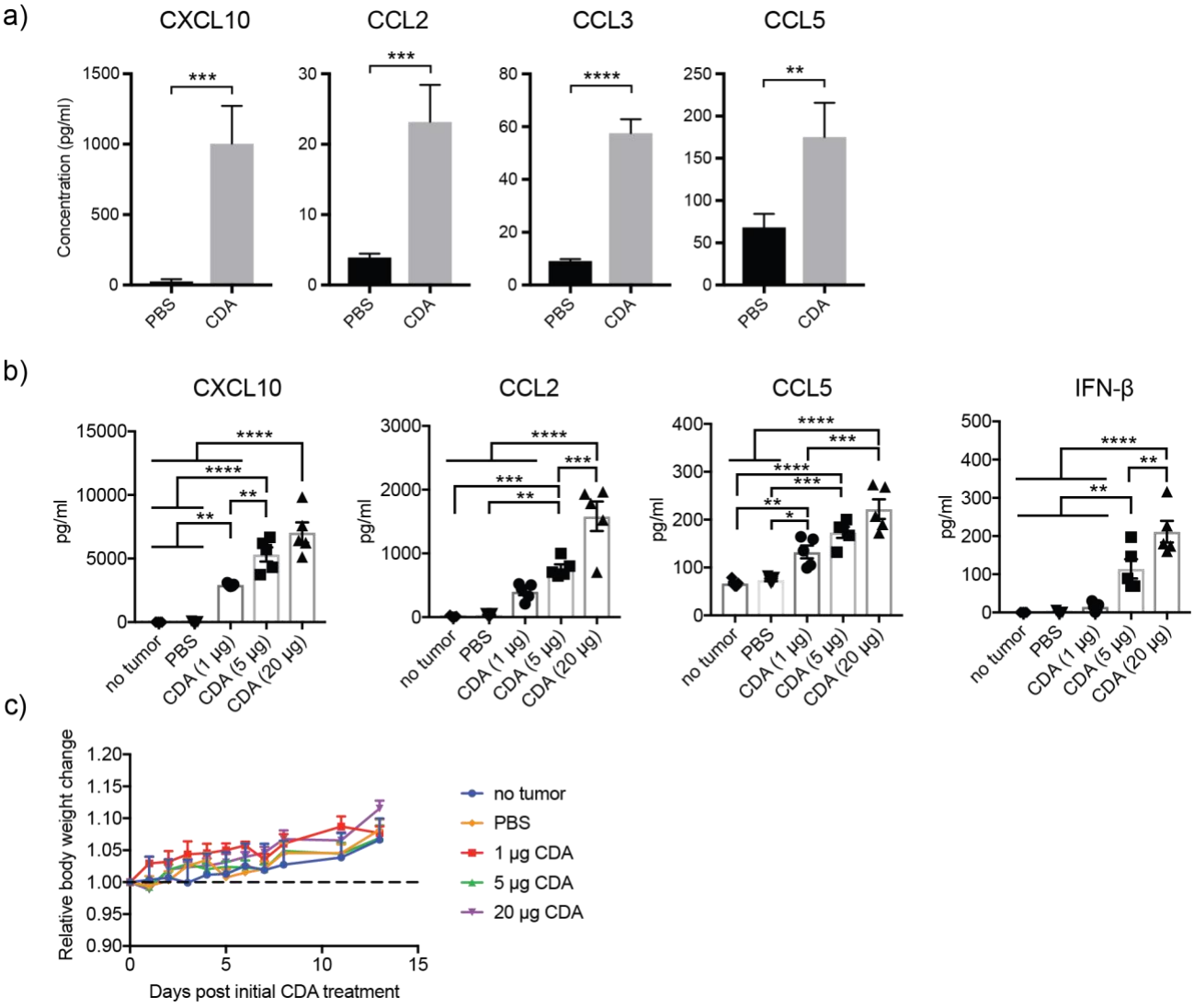

Figure 3-4. In vitro and in vivo effects of CDA treatment. (**a**) CDA (5 µg/ml) was treated to mouse BMDCs for 6 hours and culture media were analyzed for the levels of chemokines by ELISA. (**b**) Serum chemokine/cytokine concentrations 3 hours after intratumoral injection of CDA. Mice with no tumor did not receive CDA injection. (**c**) Body weight change after CDA injection. For 1 and 5 µg CDA, mice received injections every 3 days for three times and for 20 µg, only one injection was performed. Initial injections were done on day 8 post tumor injection. Data are presented as mean ± SEM. *$p < 0.05$, **$p < 0.01$, ***$p < 0.001$ and ****$p < 0.0001$, analyzed by (**a**) student's t-test or (**b**) one-way ANOVA, followed by Tukey's HSD multiple comparison post hoc test.

Next, we investigated the effects of i.t. administration of CDA on vaccine-primed CD8+ T cells. C57BL/6 mice were inoculated with $6x10^5$ MC-38 cells at s.c. flank. On day 7 when tumors were palpable, mice were s.c. vaccinated with NP Vacc, Sol Vacc, or PBS, followed by i.t. injection of CDA on day 11 (**Figure 3-5a**). Analyses of PBMCs on day 14 for the frequency of tumor-specific CD8+ T cells indicated that CDA mono-therapy induced weak anti-tumor CD8+ T cells in the systemic circulation (**Figure 3-5b**). Additional i.t. administration of CDA followed by s.c. NP Vacc or Sol Vacc slightly increased the mean frequency of vaccine-primed tumor-specific CD8+ T cells in circulation, but the increases were not statistically significant (**Figure 3-5b**). In stark contrast NP Vacc + CDA potently increased the number of CD3+CD8+ T cells in the TME (**Figure 3-5c**) and achieved 10.9-fold ($p < 0.0001$), 3.6-fold ($p < 0.001$), and 3.7-fold ($p < 0.001$) higher numbers of intratumoral neoantigen-specific CD8+ T cells, compared with CDA alone, NP Vacc alone, or Sol Vacc + CDA, respectively (**Figure 3-5d**). On the other hand, Sol Vacc + CDA had a minor effect on the level of CD8+ T cells in the TME (**Figure 3-5c,d**), probably due to weaker priming of CD8+ T cells by Sol Vacc. Moreover, NP Vacc + CDA significantly elevated the intratumoral concentration of IFN-γ (**Figure 3-5e**), which is a pleiotropic cytokine involved in cellular migration and effector functions of T cells during tumor rejection (*117-121*). We also monitored the effect of Vacc + CDA combination therapy on tumor growth and survival of MC-38-bearing mice. MC-38 tumor bearing mice were vaccinated with either NP Vacc or Sol Vacc on day 7, followed by i.t. administration of CDA on days 11, 14, and 17 (**Figure 3-5f**). Sol Vacc + CDA slowed the average tumor growth, but the majority of animals succumbed to tumor growth by day 50 with 32% survival rate (**Figure 3-5g,h**). Importantly, NP Vacc + CDA exhibited remarkable anti-tumor efficacy, leading to robust tumor regression and complete tumor

elimination in ~70% of animals (**Figure 3-5g,h**). In addition, 100% of the survivors from the NP Vacc + CDA group were resistant to tumor re-challenge with $1.2x10^6$ MC-38 cells injected in the contralateral s.c. flank on day 90 (**Figure 3-5i**), showing long-term immunological memory response. Overall, these results demonstrate that CDA promotes tumor trafficking of antigen-specific CD8+ T cells primed by NP Vacc, leading to potent anti-tumor efficacy and long-term memory response against tumor relapse.

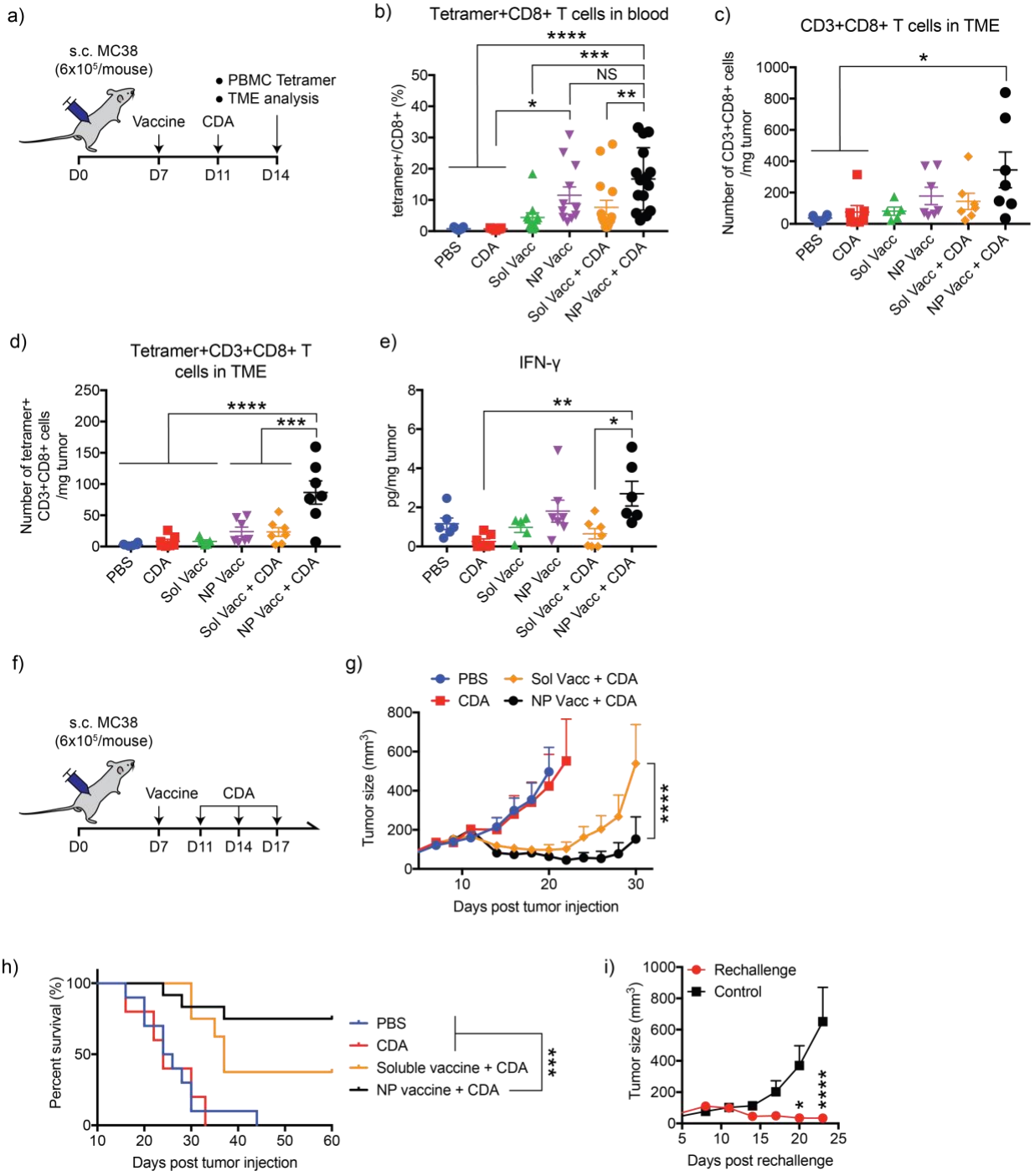

Figure 3-5. Combination of PEI NPs and STING agonist elicits tumor-specific CD8+ T cells in peripheral blood and the TME, leading to robust anti-tumor efficacy. (a) Timeline of experiment. C57BL/6 mice were inoculated at s.c. flank with $6x10^5$ MC-38 colon carcinoma cells on day 0 and vaccinated at s.c. tail base on day 7 with the indicated vaccines. A subset of animals also received intratumoral administration of 0.5 μg CDA on day 11. On day 14, animals were analyzed for **(b)** Adpgk-tetramer+CD8+ T cells within PBMCs, **(c)** tumor-infiltrating CD3+CD8+ T cells, and **(d)** tumor-infiltrating Adpgk-tetramer+CD3+CD8+ T cells by flow cytometry. **(e)** Concentrations of IFN-γ were measured in tumors using ELISA. **(f)** Timeline of experiment. C57BL/6 mice inoculated at s.c. flank with $6x10^5$ MC-38 colon carcinoma cells on day 0 were vaccinated on day 7 via s.c. tail base. These mice received intratumoral administration of 0.5 μg CDA on days 11, 14, and 17. Shown are **(g)** the average

tumor growth curves and (**h)** animal survival. (**i)** Tumor growth curve after re-challenging survivors with MC-38 cells. Mice were re-challenged with $1.2x10^6$ MC-38 cells by subcutaneous injection on the left-side flanks 90 days after the initial tumor inoculation. Data are presented as mean ± SEM. *$p < 0.05$, **$p < 0.01$, ***$p < 0.001$, and ****$p < 0.0001$, analyzed by (**b-e)** one-way ANOVA followed by Tukey's HSD multiple comparison post hoc test or (**g,i)** two-way ANOVA followed by Sidak's multiple comparisons test. (**h)** The survival curves were analyzed by the log-rank (Mantel−Cox) test.

Lastly, we sought to demonstrate the therapeutic potential and generality of NP Vacc + CDA combination therapy using B16F10 melanoma model, which is highly aggressive and resistant to conventional immunotherapies (*122, 123*). M27 peptide, a MHC class I-restricted neoantigen identified in B16F10 cells (*124*), was utilized to prepare PEI-PEG/M27 conjugates and subsequently formulated into NP Vacc with CpG as described earlier. C57BL/6 mice were inoculated at s.c. flank with 3 x 10^5 B16F10 tumor cells and vaccinated at s.c. tail base with NP Vacc on day 4, followed by i.t. administration of CDA on days 8, 11, and 14 (**Figure 3-6a**). Proliferation and activation of M27-specific CD8+ T cells were analyzed by IFN-γ ELISPOT assay performed on day 11 using splenocytes. NP Vacc elicited robust M27-specific IFN-γ+ CD8+ T cells, generating 57-fold higher ELISPOT responses than CDA mono-therapy ($p < 0.0001$, **Figure 3-6b**). Whereas combination CDA treatment slightly decreased the frequency of M27-specific IFN-γ+ T cells in spleen (**Figure 3-6b**), it significantly increased the concentrations of IFN-β, CCL5, and CXCL10 in tumor (**Figure 3-6c**), compared with NP Vacc alone. In parallel, we monitored animals for tumor growth and survival (**Figure 3-6d,e**). As B16F10 melanoma is a poorly immunogenic (*122, 123*), NP Vacc alone failed to slow the tumor growth or extend the animal survival (**Figure 3-6d,e**). While CDA mono-therapy slightly delayed the tumor growth, all mice succumbed to tumor growth within 35 days. On the other hand, NP Vacc + CDA exhibited a remarkable anti-tumor efficacy, eradicating B16F10 tumors in 100% of treated mice (**Figure 3-6d,e**). Overall, these results showed that PEI NP vaccine + CDA combination therapy exerts potent anti-tumor efficacy against even poorly immunogenic tumors.

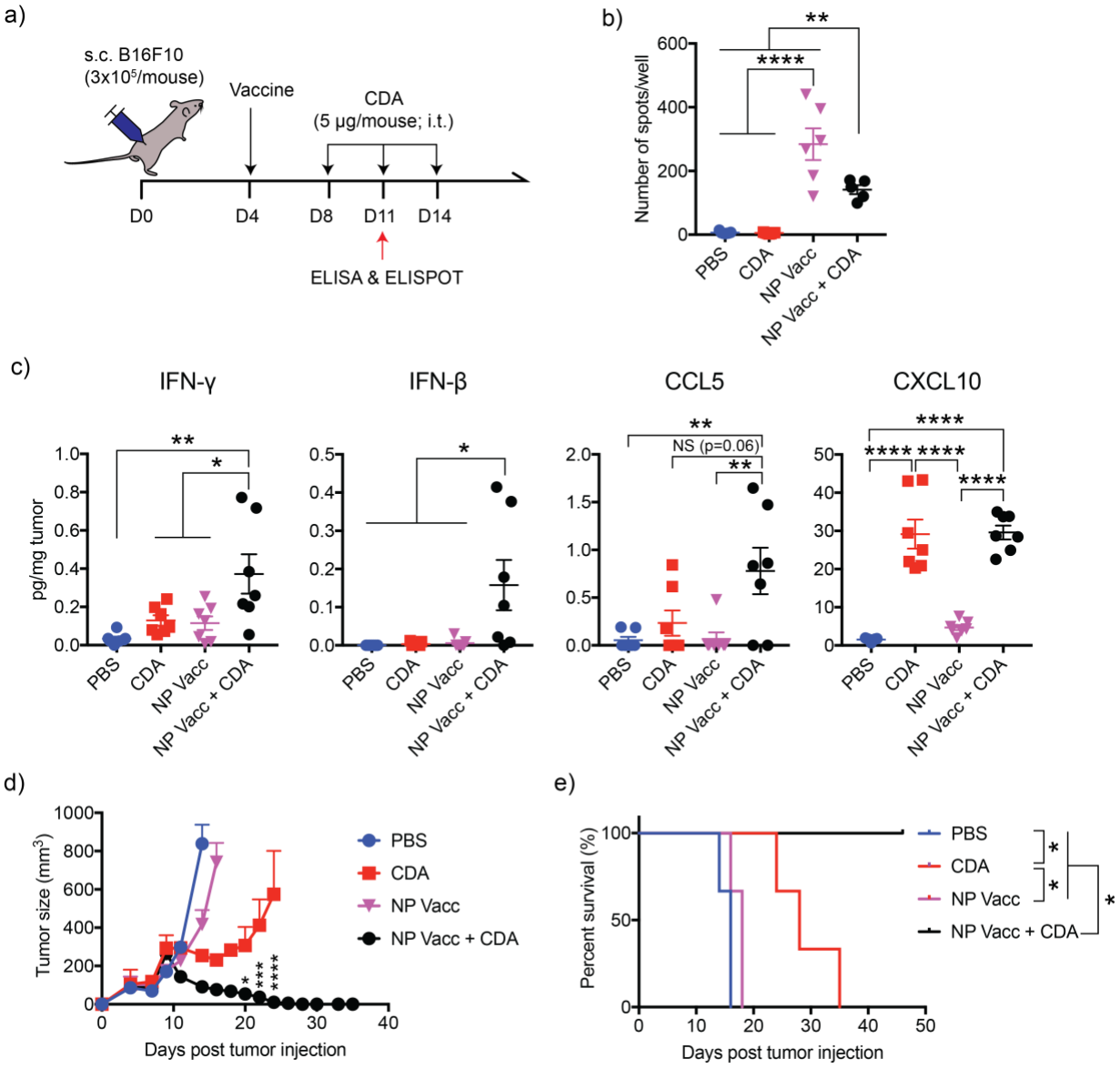

Figure 3-6. PEI NP vaccine plus CDA combination therapy regresses poorly immunogenic B16F10 melanoma. a) Timeline of experiment. While tumor growth and survival of B16F10-bearing mice were monitored, subsets of mice were sacrificed on day 11 for ELISPOT and ELISA analyses using spleens and tumor samples, respectively. b) Neoantigen peptide (M27)-specific cells within splenocytes were detected with IFN-γ ELISPOT assay. c) Cytokine concentrations in tumor measured by ELISA. d) Tumor growth and e) survival curves of B16F10 tumor-bearing mice. Asterisks in d) indicate statistical comparison between CDA and NP Vacc + CDA. Data are presented as mean ± SEM. *$p < 0.05$, **$p < 0.01$, and ****$p < 0.0001$, analyzed by **b,c)** one-way ANOVA followed by Tukey's HSD multiple comparison post hoc test or **d)** two-way ANOVA followed by Sidak's multiple comparisons test. **e)** The survival curves were analyzed by the log-rank (Mantel−Cox) test.

3.5. Conclusion

In conclusion, we have developed PEI-based NPs co-delivering CpG adjuvants and tumor-specific neoantigen peptides for personalized cancer immunotherapy and showed that they elicit potent anti-tumor CD8+ T cell responses in the systemic circulation; however, this was not sufficient to inhibit tumor growth, in part due to poor tumor infiltration of activated CD8+ T cells. We demonstrated for the first time that local administration of STING agonist can significantly enhance infiltration of NP vaccine-primed CD8+ T cells into the TME by promoting secretion of T cell-attracting chemokines and cytokines, leading to robust tumor regression and long-term immunological memory. Our strategy of utilizing STING-based immunotherapy for potentiating NP-based cancer vaccines present a new combination nano-immunotherapy that is be widely applicable for combination cancer immunotherapy.

CHAPTER IV. Lipid-based Vaccine Nanoparticles for Induction of Humoral Immune Responses against HIV-1 and SARS-CoV-2

4.1. Abstract

The current health crisis of corona virus disease 2019 (COVID-19) highlights the urgent need for vaccine systems that can generate potent and protective immune responses. Protein vaccines are safe, but conventional approaches for protein-based vaccines often fail to elicit potent and long-lasting immune responses. Nanoparticle vaccines designed to co-deliver protein antigens and adjuvants can promote their delivery to antigen-presenting cells and improve immunogenicity. However, it remains challenging to develop vaccine nanoparticles that can preserve and present conformational epitopes of protein antigens for induction of neutralizing antibody responses. Here, we have designed a new lipid-based nanoparticle vaccine platform (NVP) that presents viral proteins (HIV-1 and SARS-CoV-2 antigens) in a conformational manner for induction of antigen-specific antibody responses. We show that NVP was readily taken up by dendritic cells (DCs) and promoted DC maturation and antigen presentation. NVP loaded with BG505.SOSIP.664 (SOSIP) or SARS-CoV-2 receptor-binding domain (RBD) was readily recognized by neutralizing antibodies, indicating the conformational display of antigens on the surfaces of NVP. Rabbits immunized with SOSIP-NVP elicited strong neutralizing antibody responses against HIV-1. Furthermore, mice immunized with RBD-NVP induced robust and long-lasting antibody

responses against RBD from SARS-CoV-2. These results suggest that NVP is a promising platform technology for vaccination against infectious pathogens.

4.2. Introduction

As shown during the current COVID-19 pandemic, reliable and efficient vaccine delivery systems are urgently needed for vaccine development against COVID-19 as well as other emerging pathogens (*125, 126*). Traditional vaccines based on the live attenuated virus and inactivated virus vaccines are potent activators of the immune system, but they are limited by potential viral reversion and long development and regulatory timeline. On the other hand, protein vaccines with favorable safety profiles have been widely used for prophylactic vaccination against various pathogens, such as hepatitis B and influenza viruses (*127*). Yet, protein subunit vaccines often fail to elicit potent and long-lasting immune responses.

These challenges may be addressed by co-administering subunit protein vaccines with potent adjuvants (*128*), especially in nanoparticle formulations that allow for their co-delivery to antigen-presenting cells for strong immune activation (*129*). There are various nanoparticle vaccine platforms under development, including polymers (*130, 131*), gold (*132, 133*), silica (*79, 134*), and others (*44, 135*). In particular, lipid-based nanoparticles are generally considered to have excellent biocompatibility and safety, and they have been used as a vaccine carrier to deliver mRNA (*136*), DNA (*137-139*), and peptides (*140*). However, for protein antigens, it remains challenging to preserve their conformational epitopes and achieve robust neutralizing antibody responses using nano-vaccines. In particular, conformational display of antigens in vaccine formulations is crucial as immunogens should present epitopes to which the immune cells recognize, interact, and generate immune responses. Here, we sought to address these challenges

by designing a new lipid-based nanoparticle vaccine platform (NVP) that can load and present viral proteins (HIV-1 and SARS-CoV-2 antigens) in a conformational manner for induction of antigen-specific antibody responses.

In particular, previous studies on acquired immunodeficiency syndrome (AIDS) have revealed the presence of broadly neutralizing antibodies in a subset of AIDS patients (*141, 142*). As the human immunodeficiency virus-1 (HIV-1) envelope glycoprotein (Env gp) has been identified to induce broadly neutralizing antibodies, various HIV-1 Env gp immunogens have been developed. Among them, BG505.SOSIP.664 (SOSIP) has emerged as a promising immunogen for inducing neutralizing antibodies against HIV-1 (*143-145*). SOSIP is derived from the BG505 HIV-1 clade A virus, which was isolated from a 6-week-old infant who later developed broadly neutralizing antibodies (*145, 146*). The native form of the glycoprotein gp160 is cleaved into gp120 and gp41 subunits during HIV-1 entry into host cells. To utilize gp160 for vaccination purpose, the membrane-associated and cytoplasmic domains were truncated and stabilized by insertion of a disulfide bond (referred to as "SOS") and an Ile/Pro ("IP") substitution at residue 559 (I559P), resulting in an immunogen termed as SOSIP (*143-145*). SOSIP self-assembles into a soluble HIV-1 Env trimer; therefore, nano-vaccine formulation with SOSIP should maintain the structural integrity and neutralizing epitopes of SOSIP.

During the initial COVID-19 outbreak, the structural similarities between SARS-CoV and SARS-CoV-2 were discovered (*147*). It was subsequently revealed that spike glycoprotein (S protein) of SARS-CoV-2 was responsible for viral infection via interaction with angiotensin-converting enzyme 2 (ACE2) receptors on human cell membranes and that the antibodies generated against the S protein effectively neutralize viral entry to human cells (*42, 148*). The receptor-binding domain (RBD) is the functional domain within the S protein that first engages

with ACE2, is considered a prime target for COVID-19 vaccine development, and can be produced as a recombinant antigen to generate directed antibody responses (*149, 150*).

It should be noted that both SOSIP and RBD possess tertiary molecular structures through various bonds, including disulfide bond (*41, 151*), that are prone to denaturation if placed under harsh condition, e.g., extreme pH, temperature, and physical stress. While we have previously reported lipid-based vaccine nanoparticles that employ thiol-maleimide crosslinking reaction to form nanoparticles (*152-155*), they are not ideal for immunogens held together by disulfide bonds, such as in SOSIP. Therefore, we sought to design a new nano-formulation for loading HIV-1 SOSIP and SARS-CoV-2 RBD while preserving epitopes for inducing antibody responses. We show that pre-formed lipid vesicles incubated with protein antigens, followed by complexation and stabilization of lipid layers with branched polyethyleneimine (PEI), forms a nanoparticle vaccine platform (NVP) capable of loading viral antigens in a conformational manner. NVP co-loaded with antigens and monophosphoryl lipid A (MPLA, a potent Toll-like receptor-4 agonist) was readily taken up by dendritic cells (DCs) and promoted DC maturation and antigen presentation. NVP carrying SOSIP or RBD was recognized and surface-bound by neutralizing antibodies, indicating the conformational display of antigens on the surfaces of NVP. Rabbits immunized with SOSIP-NVP elicited neutralizing antibody responses against HIV-1. Moreover, mice immunized with RBD-NVP induced robust and durable antibody responses against RBD from SARS-CoV-2. These results suggest that NVP is a promising platform technology for vaccination against infectious pathogens.

4.3. Materials and Methods

Reagents

SOSIP proteins were kindly provided by Drs. John Moore and Rogier Sanders from Weill Medical College, Cornell University, New York. Recombinant RBD proteins were kindly provided by Dr. Janet Smith of University of Michigan, Ann Arbor. Antigen (SOSIP)-specific primary monoclonal antibodies b6 and PGV04 were kindly provided by the International AIDS Vaccine Initiative. Rabbit Anti-Mouse IgG H&L-HRP was purchased from Abcam. Goat Anti-Mouse IgG1-HRP and Goat Anti-Mouse IgG2a-HRP were purchased from Southern Biotech. Following antibodies were used for antigen display assay: human IgG1 kappa isotype (EMD Millipore), PE-conjugated anti-human IgG (Fcγ) secondary antibody (ebioscience), Alexa Fluor 488-labeled anti-human IgG1 Fc secondary antibody (Invitrogen), Anti-SARS-CoV-2 RBD Neutralizing Antibody, Human IgG1 (SAD-S35) (Acrobiosystems).

Synthesis and characterization of nanoparticle vaccine platform (NVP)

1,2-dioleoyl-sn-glycero-3-phosphocholine (DOPC) (Avanti Polar Lipids), n-(succinimidyloxy-glutaryl)-L-α-phosphatidylethanolamine, dioleoyl (DOPE-NHS) (NOF America Corporation) and monophosphoryl lipid A (MPLA) (Avanti Polar Lipids), all dissolved in chloroform, were mixed in 50:50:0.5 molar ratio in a glass vial. Lipids were dried under nitrogen gas, followed by a further complete drying step by putting the vial inside a desiccator. The dried lipid film was rehydrated with 100 µl of bis-tris propane (BTP) buffer (pH 7.0) by vortexing for 10 sec every minute for 7 min. The resulting multilamellar vesicles were probe tip-sonicated at 40% amplitude for 5 min while placed in ice. The resulting unilamellar vesicles (ULV) were mixed with 100 µl of either SOSIP (25 µg) - or RBD (20 µg)-containing BTP buffer and incubated in 37 ^{o}C for 30 min under constant shaking. Branched PEI of 1800 Da (number-based average) (Sigma Aldrich) was added at 0.35:1 primary amine:NHS ratio (NHS groups present in liposome), and then the mixture was further incubated at 37 ^{o}C for 30 min. The resulting antigen-loaded NVP

suspension was centrifuged at 14,000 g for 5 min, then were washed with PBS twice, followed by final resuspension with 200 µl of PBS. The particles were transferred to deionized water for size and surface charge measurement using the Zetasizer Nano (Malvern, UK). The loading efficiencies of proteins in NVP were measured by sodium dodecyl sulphate–polyacrylamide gel electrophoresis (SDS-PAGE), followed by Coomassie Blue staining (for SOSIP and RBD). Gels were imaged with a gel doc machine, Fluorchem M Imaging System (Protein Simple).

In vitro DC uptake assays

Mouse BMDCs were isolated from bone marrow obtained from hind femurs of C57BL/6 mice. Cells were cultured in media supplemented with GM-CSF for 10 days in 37 ºC, 5% CO2. Mature BMDCs were seeded in $2x10^5$ per well of a 96-well tissue culture plate (flow cytometry) or $1x10^5$ per well of an 8-well chambered cover glass (confocal microscopy), incubated for at least 6 hr for cell adhesion, and then treated with DQ-OVA (Invitrogen)-containing vaccine formulations for 1-24 hr. For flow cytometry analysis, cells were recovered after trypsin treatment for 10 min. Retrieved cells were incubated with anti-CD16/32 blocking antibody for 10 min in room temperature (RT), followed by incubation with anti-CD11c, anti-CD80, and anti-SIINFEKL/MHC-I antibodies for 20 min in RT and a fixable viability dye (eFluor 450, eBioscience) for 10 min in RT. Cells were then fixed with 4% formaldehyde in PBS for 10 min, washed and resuspended in PBS containing 1% bovine serum albumin (BSA) and analyzed with a flow cytometer (Bio-Rad ZE5). For confocal microscopy, BMDCs were treated with DQ-OVA formulations for 4 hr, followed by three times of washing with PBS. Cells were then stained with 0.1 µM Lysotracker (ThermoFisher L7528) and 1 µg/ml Hoechst (ThermoFisher H3570) in 37 ºC for 30 min. After washing with PBS, cells were fixed with 4% formaldehyde in PBS for 15 min, followed by washing with PBS. Cells were then analyzed with Nikon A1Rsi confocal microscope.

Antigens display on NVP

For assessing antigen display on NVP, 1,1´-dioctadecyl-3,3,3´,3´-tetramethylindodicarbocyanine (DiD) (Invitrogen, 0.2 mol%) was added in the lipid composition of NVP. Fluorescence signal from DiD was used to normalize the amount of NVP for comparison between different formulations due to variance in the recovery of formulations. For SOSIP-NVP, SOSIP-specific antibodies, b6 and PGV04, were incubated with NVP, followed by washing in PBS and addition of PE-conjugated anti-human IgG (Fcγ) secondary antibody (ebioscience). For RBD-NVP, monoclonal neutralizing antibody (SAD-S35, Acrobiosystems) against SARS-CoV-2 was treated (1:100 dilution), followed by washing in PBS (x3) and addition of Alexa Fluor 488-labeled anti-human IgG1 Fc secondary antibody (1:50 dilution) (Invitrogen). Antibody incubations were performed at room temperature for 30 min with constant shaking. Resulting samples were measured with a fluorometer (Biotek Synergy Neo microplate reader) at excitation/emission wavelengths of 485 nm/528 nm and 630 nm/680 nm or by "NanoFACS" as we recently reported (*153*).

In vivo vaccination study

Animals were cared for following federal, state, and local guidelines. All experiments performed on animals were in accordance with and approved by the Institutional Animal Care and Use Committee (IACUC) at the University of Michigan, Ann Arbor. White New Zealand rabbits (6-8 weeks old females from Jackson Laboratory) were vaccinated subcutaneously at four sites on both caudal thighs (2 sites per side) with either soluble mixture SOSIP and MPLA or NVP co-loaded with SOSIP and MPLA. Doses used for primary and boost injections were 30 μg SOSIP + 50 μg MPLA and 12.4 μg SOSIP + 20.6 MPLA, respectively. Primary vaccination was injected on day 0, followed by boost vaccinations on days 28 and 84. 2-3 ml of blood was sampled from

each rabbit via marginal ear vein on days 28, 56, 105 and 169, which was placed in room temperature undisturbed for 1 hr to induce coagulation, followed by centrifugation at 2,000 g for 12 min at 4 ^{o}C to obtain serum. Rabbit immune sera were analyzed for neutralizing activities against homologous tier 1A (MW965.26) and 2 (BG505/T332N) viral entry using the TZM-bl cell assay, which measures transactivation of a luciferase reporter gene by an infecting virus (*156, 157*). BALB/c mice (6-8 weeks old females from Jackson Laboratory) were vaccinated subcutaneously at the tail-base on days 0, 14, and 28 with either soluble mixture RBD and MPLA or NVP co-loaded with RBD and MPLA. PBS was included as a negative control. The dose used for each injection was 0.5 μg RBD and 1 μg MPLA. Blood was sampled from each mouse via submandibular vein on days 14, 28 and 42. Samples were collected in a gel-containing tube (Microvette 500 SER-GEL, Sarstedt Inc.), followed by centrifugation at 10,000 g for 5 min to obtain serum. Mouse immune sera were analyzed for RBD-specific IgG, IgG_1, and IgG_{2a} antibody titers using ELISA. Briefly, RBD protein was coated on 96-well ELISA plates (0.1 μg/well) and serially diluted sera samples were added. After one hr of incubation and multiple washings, horse radish peroxidase (HRP)-labeled secondary antibodies were added and further incubated for 1 hr in room temperature. Secondary antibodies used included rabbit anti-mouse IgG H&L-HRP (Abcam), goat anti-mouse IgG1-HRP (Southern Biotech) or goat anti-mouse IgG2a-HRP (Southern Biotech). Next, TMB substrate solution was added, and the reaction was stopped by the addition of NaF. The absorbance was measured at a 620 nm wavelength using a plate reader (Synergy Neo, BioTek). To measure antibody titers, titration curves were drawn based on the absorbance and the dilution factor, from which half maximal effective concentration (EC50) values were calculated using a software Gen5 (BioTek).

Lymph node trafficking study

BALB/c mice were subcutaneously injected at the tail-base with PBS, soluble antigen + MPLA, or antigen-MPLA-NVP. As a model antigen for investigating lymph node trafficking, Alexa Fluor 647-labeled ovalbumin (AF647OVA) (Invitrogen) was used. A dose consisting of 10 µg of AF647OVA and 11 µg of MPLA was injected to each mouse. After 4, 8, 24 and 48 hr of injection, serum samples were collected for ELISA to measure proinflammatory cytokine levels. After 48 hr, draining lymph nodes were collected for fluorescence imaging to quantify the amount of antigen. Lymph nodes were placed in the imaging machine (IVIS spectrum, PerkinElmer) and imaged using 640 nm and 680 nm ex/em filters. Lymph nodes were then processed into single cells for flow cytometric analysis. Briefly, lymph nodes were homogenized with a mini-tissue homogenizer, then passed through a 40 µm strainer to collect single cells. After washing the cells twice with PBS (1% BSA), anti-CD16/32 Ab was added for 10 min at 4 ^{o}C, followed by the addition of anti-mouse CD80 Ab (FITC) (BD Biosciences), anti-mouse CD86 Ab (PECy7) (eBioscience), and anti-mouse CD11c Ab (PE) (BioLegend) Ab for 30 min at 4 ^{o}C. Then the cells were washed twice with PBS, stained for live/dead (EBioscience, Fixable viability dye eFluor 450), and fixed with 4% formaldehyde. Resulting cells were washed twice with PBS (1% BSA) and analyzed by flow cytometry.

Blue native PAGE

For Blue Native PAGE, samples were run on NativePAGE^{TM} Novex® Bis-Tris gel system (Life Technologies). Briefly, samples were diluted in Native PAGE sample buffer, bath sonicated to disrupt aggregates, and were incubated with N-Dodecyl β-D-maltoside (DDM, Invitrogen) at a 1.11% working concentration for 30 min on ice. Immediately before loading onto gels (3%-12% Bis-Tris), Coomassie G-250 was added to the samples following manufacturer's instructions. Gels were run at room temperature using dark blue cathode buffer for approximately 100 min. Gels

were destained according to manufacturer's instructions, and protein migration was assessed by silver staining (Thermo Fisher).

Statistical analysis

The results are expressed as means ± SEM. Prism 7.0e (GraphPad Software) software was used for statistical analyses. Statistical comparisons were performed using either unpaired student's t-test or one-way or two-way ANOVA, followed by Tukey's HSD multiple comparison test. Statistical significances are indicated as $*p < 0.05$, $**p < 0.01$, $***p < 0.001$, and $****p < 0.0001$.

4.4. Results and Discussion

Synthesis and characterization of NVP.

We synthesized a nanoparticle vaccine platform (NVP) by adding viral antigens to pre-formed unilamellar lipid vesicles, followed by incubation with branched PEI that allows for complexation and stabilization of vesicles into NVP via interaction between NHS-functionalized phospholipids and primary amine groups in PEI. Briefly, multilamellar vesicles were prepared by hydrating a lipid film composed of 1,2-dioleoyl-sn-glycero-3-phosphocholine (DOPC), n-(Succinimidyloxy-glutaryl)-L-α-phosphatidylethanolamine, dioleoyl (DOPE-NHS) and monophosphoryl lipid A (MPLA, a Toll-like receptor-4 agonist) (50:50:0.5 mol ratio). Multilamellar vesicles were tip sonicated to form into unilamellar vesicles, which then were mixed and surface-loaded with antigen proteins. Branched PEI (1,800 Da) was subsequently added in a primary amine:NHS ratio of 0.35:1 to induce complexation of lipid vesicles and nanoparticle formation by the reaction between the primary amines on PEI and the NHS groups on the

unilamellar vesicles (**Figure 4-1a**). The resulting NVP exhibited a hydrodynamic size of 200-400 nm and a polydispersity index of 0.1-0.3 depending on the antigen added, with slightly negative surface charge as shown by dynamic light scattering (DLS) measurement (**Figure 4-1b**).

a)

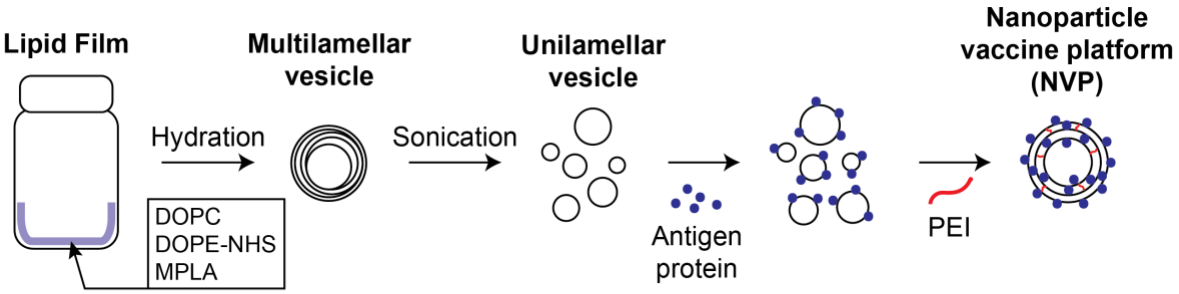

b)

	Mean size (nm)	PDI	Zeta potential (mV)	Loading efficiency (%)
Blank NVP	214.3 ± 5.0	0.104 ± 0.021	-25.7 ± 0.3	NA
SOSIP-NVP	335.8 ± 15.4	0.300 ± 0.021	-18.9 ± 0.4	27.8 ± 1.7
RBD-NVP	236.2 ± 2.4	0.244 ± 0.002	-23.4 ± 0.7	21.0 ± 0.8

Figure 4-1. Preparation and characterization of NVP. (**a)** Schematic drawing of NVP preparation process. (**b)** Mean hydrodynamic size, PDI, and surface charge of NVPs as measured by DLS. Protein loading efficiency was calculated based SDS-PAGE analysis.

NVP improves antigen uptake by DCs and enhances DC activation and antigen presentation

As a model antigen, DQ-labeled ovalbumin (DQ-OVA) was loaded to NVP to examine antigen delivery to and activation of DCs *in vitro* (**Figure 4-2a-f**) DQ is a self-quenched dye that emits fluorescence upon degradation after cellular entry (*158*). PAGE analysis showed efficient loading (~60%) of DQ-OVA to NVP (**Figure 4-2g**). BMDCs treated for 1 hr with NVP carrying DQ-OVA (DQ-OVA-NVP) exhibited a 2.72-fold increase in the DQ signal, compared with those treated with soluble DQ-OVA and MPLA mixture, as confirmed by flow cytometry (**Figure 4-2a**). A similar trend was observed over 24 hr (**Figure 4-2b**). As shown by confocal microscopy, BMDCs treated with DQ-OVA-NVP for 4 hr showed significantly higher DQ signal within the cytosol, with a high level of co-localization with lysosomes (**Figure 4-2h**). In addition, DQ-OVA-NVP induced robust DC maturation, as shown by the up-regulation of CD80 co-stimulatory

marker on DCs within 1 hr of incubation (**Figure 4-2c**) and throughout 24 hr time window (**Figure 4-2d**). Moreover, we examined antigen presentation on DCs by flow cytometry assay after staining DCs with a monoclonal antibody specific to an immunodominant OVA epitope (SIINFEKL) loaded in major histocompatibility complex-I (MHC-I) molecule. NVP-mediated DQ-OVA delivery led to significantly greater antigen presentation on DCs (**Figure 4-2e-f**). Taken together, these results show that NVP significantly increases DC uptake of vaccines, leading to improved DC activation and antigen presentation.

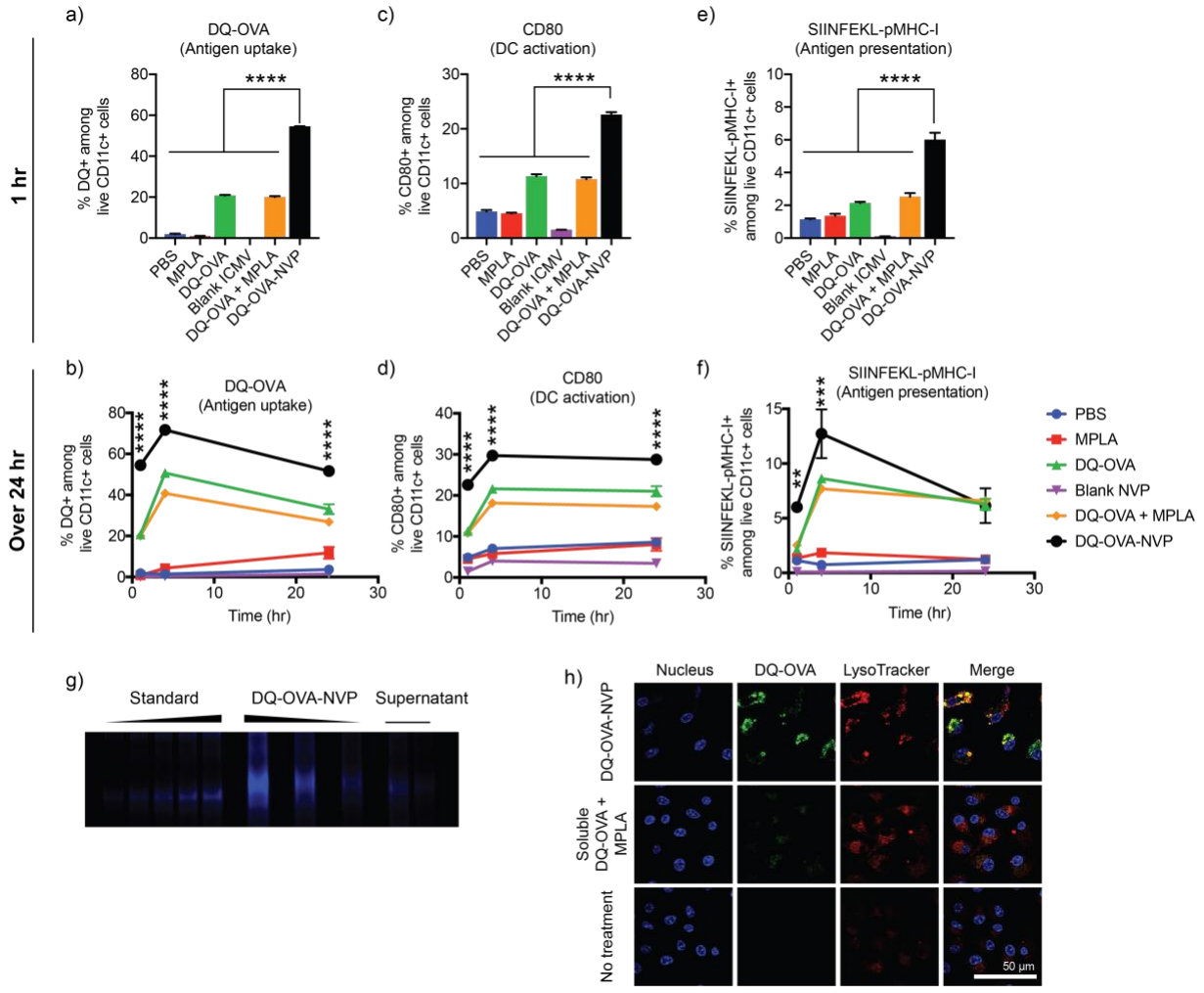

Figure 4-2. NVP enhances antigen uptake, activation and antigen processing by dendritic cells *in vitro*. (a-g) BMDCs were treated with DQ-OVA and MPLA using the indicated formulations, and DQ-OVA signal was quantified by (**a-b**) flow cytometry after 1, 4, and 24 hr of incubation. BMDCs were also assessed for (**c-d**) CD80 expression and (**e-f**) antigen presentation of SIINFEKL on MHC-I. **(g)** SDS-PAGE image of DQ-OVA-loaded NVP. **(h)** After 4 hr of incubation, BMDCs were stained with LysoTracker and Hoechst, followed by confocal microscopy. Data are presented as mean ± SEM. $^{**}p < 0.01$, $^{****}p < 0.0001$,

analyzed by one-way ANOVA **(a,c,e)** or two-way ANOVA **(b,d,f)**, followed by Tukey's HSD multiple comparison post hoc test. Asterisks in **(b,d,f)** indicate statistical comparison between DQ-OVA-NVP and DQ-OVA.

NVP effectively delivers antigen to DCs in lymph nodes

Next, we investigated NVP-mediated lymph node trafficking of antigen using a model antigen, Alexa Fluor 647 (AF647)-labeled ovalbumin (AF647OVA). Mice were given tail-base subcutaneous injection of PBS, soluble AF647OVA + MPLA, or AF647OVA-loaded NVP (OVA-MPLA-NVP), followed by flow cytometry or ELISA analyses (**Figure 4-3a**). After 48 hr of vaccination, draining inguinal lymph nodes were visualized by IVIS fluorescence imaging. Mice administered with OVA-MPLA-NVP had significantly stronger AF647 signal in lymph nodes, compared with those treated with the soluble formulation (**Figure 4-3b**). Flow cytometric analysis showed that CD11c+ DCs in lymph nodes from the OVA-MPLA-NVP group exhibited signs of maturation, as shown by CD80 and CD86 staining (**Figure 4-3c**). Interestingly, among CD80+ and CD86+ DCs, the OVA-MPLA-NVP group had significantly higher mean fluorescence intensity of AF647OVA, compared with the soluble vaccine group (**Figure 4-3d**), showing robust DC-targeted delivery of antigen by NVP. Lastly, the serum levels of proinflammatory cytokines, IL-6 and IL-12p40, were measured using ELISA. Serum concentrations of IL-6 and IL-12 were elevated at 4 hr and 8 hr post injection, respectively, for the soluble vaccine group (**Figure 4-3e**), whereas there was no spike of either cytokines in the NVP group. Taken together, these results showed that NVP provides an efficient and safe platform for antigen delivery to antigen-presenting cells in lymph nodes.

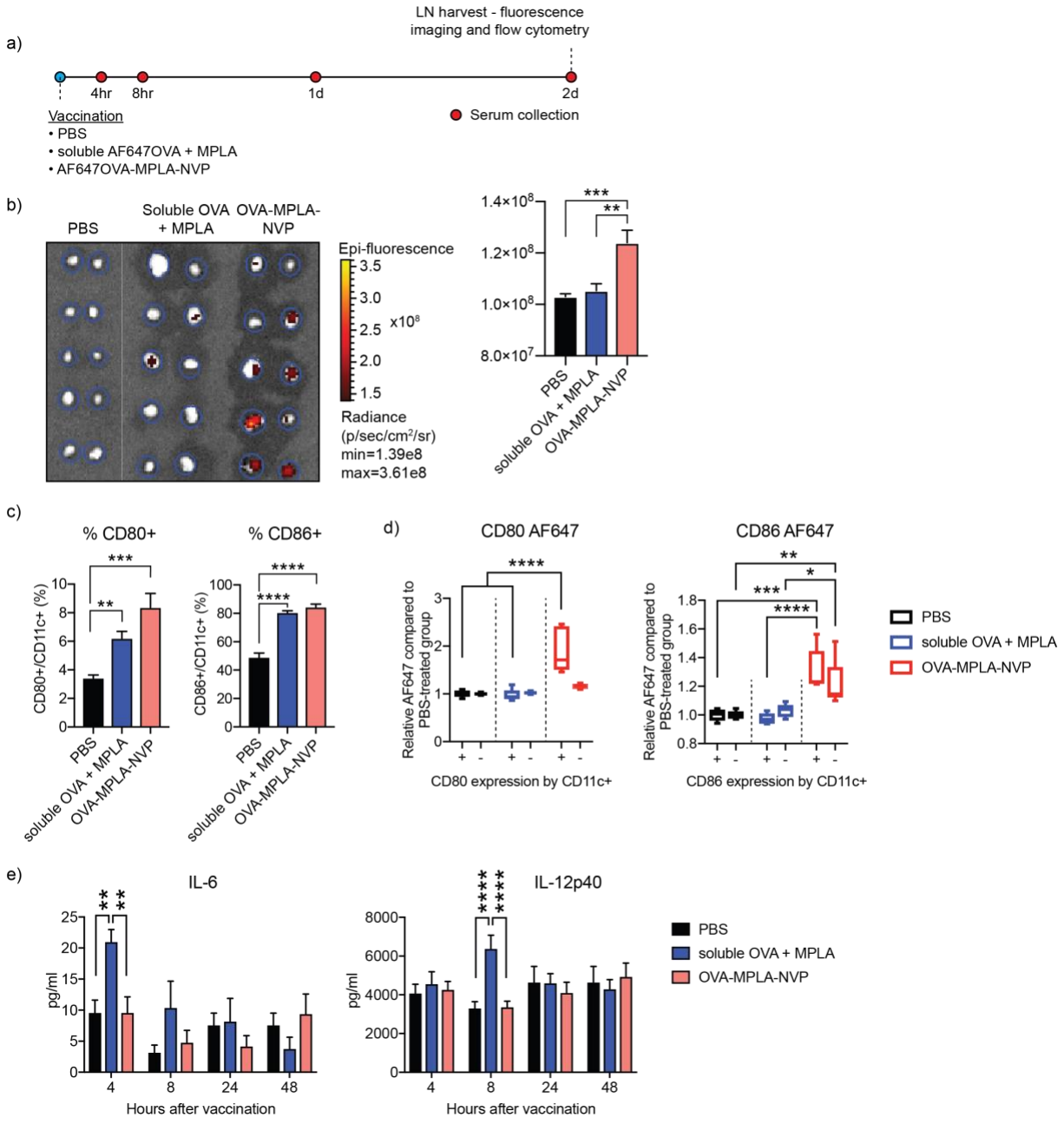

Figure 4-3. NVP improves antigen delivery to antigen-presenting cells in lymph nodes. (a) Mice were administered subcutaneously with PBS, soluble AF647OVA + MPLA, or AF647OVA-MPLA-NVP, followed by tissue analysis on the indicated time points. **(b)** Inguinal lymph nodes were excised and imaged for AF617OVA signal at 48 hr after vaccination. **(c)** CD11c+ DCs in inguinal lymph nodes were analyzed for CD80 and CD86 maturation markers. **(d)** CD11c+ DCs with or without upregulation of CD80 and CD86 were analyzed for AF647OVA. **(e)** At the indicated time points after vaccination, serum concentrations of IL-6 and IL-12p40 were analyzed by ELISA. Data are presented as mean ± SEM. *$p < 0.05$, **$p < 0.01$, ***$p < 0.001$, ****$p < 0.0001$, analyzed by (b,c) one-way ANOVA or (d,e) two-way ANOVA, followed by Tukey's HSD multiple comparison test.

Loading recombinant HIV envelope glycoprotein (SOSIP) into NVP

BG505.SOSIP.664 (SOSIP) is a recombinant HIV-1 envelope glycoprotein derived from the BG505 clade A virus. SOSIP is held together by a disulfide bond and self-assembles into a soluble HIV-1 Env trimer (**Figure 4-4a**). SOSIP is a promising immunogen for HIV-1 vaccine development, as shown by prior pre-clinical studies reporting SOSIP-mediated induction of neutralizing antibodies against HIV-1 (*143, 144, 159*). Here, we prepared NVP carrying SOSIP antigen and examined its efficacy to induce neutralizing antibody response against HIV-1. Using the procedure described above, we loaded SOSIP into NVP (SOSIP-NVP), which exhibited a hydrodynamic size of ~330 nm, as determined by DLS analysis (**Figure 4-1b**). PAGE-based quantification indicated a ~25% loading efficiency of SOSIP in NVP (**Figure 4-4b**). Notably, it is crucial to maintain the conformational epitopes and trimeric structure of HIV-1 Env for the induction of broadly neutralizing antibody responses (*160*). Therefore, we examined whether SOSIP-NVP preserves the structure and epitopes of SOSIP during the vaccine formulation. Our non-reducing PAGE analysis performed on SOSIP retrieved from SOSIP-NVP indicated that SOSIP-NVP maintained the disulfide bond in SOSIP without disruption during the loading process (**Figure 4-4b**). SOSIP also appeared in the high molecular weight area in the PAGE gel, which may have been due to complexation with PEI and incomplete retrieval process from SOSIP-NVP. In addition, the preservation of quaternary structure of SOSIP trimer after NVP loading was examined by blue-native PAGE. Interestingly, application of a significant physical stress (e.g. tip sonication) while SOSIP trimer is present in solution induced dissociation of the trimer into monomer and dimer, demonstrating the delicate binding force between the subunits (**Figure 4-4c**, 3rd lane). Thus, we modified the SOSIP-NVP preparation by adding SOSIP to the reaction mixture after any physical stresses were taken place, which resulted in the preservation of intact quaternary

structure after SOSIP-NVP formulation (**Figure 4-4c**, 5th lane). Nevertheless, these results indicated that SOSIP was effectively loaded into NVP.

To further examine whether SOSIP was displayed on the surface of NVP with its epitopes remaining intact, we performed immunofluorescence directly on SOSIP-NVP. For this, we employed Env-specific human antibodies, PGV04 and b6, which recognize the CD4 binding site of Env. PGV04 and b6 are HIV-1 broadly neutralizing antibody and non-neutralizing antibody, respectively. PGV04 and b6 were incubated with SOSIP-NVP, followed by washing and another round of incubation with fluorophore-tagged anti-human IgG antibody. Then fluorescence signal on SOSIP-NVP was quantified to assess antibody binding (**Figure 4-4d, e**). SOSIP-NVP was readily recognized and bound by PGV04, a broadly neutralizing antibody, on a whole population level, as shown by a plate-based fluorescence measurement (**Figure 4-4d**). SOSIP-NVP was also bound by b6, a non-neutralizing antibody, but to a lesser extent than PGV04. We recently reported that antibody-binding on nanoparticles could be quantified on an individual nanoparticle-basis using "NanoFACS" (*153*). Using NanoFACS, we confirmed that PGV04 was bound to individual SOSIP-NVPs (**Figure 4-4e**), thus showing the homogenous display of SOSIP on the surfaces of SOSIP-NVPs. These results indicated the preservation of SOSIP epitopes after loading in NVP.

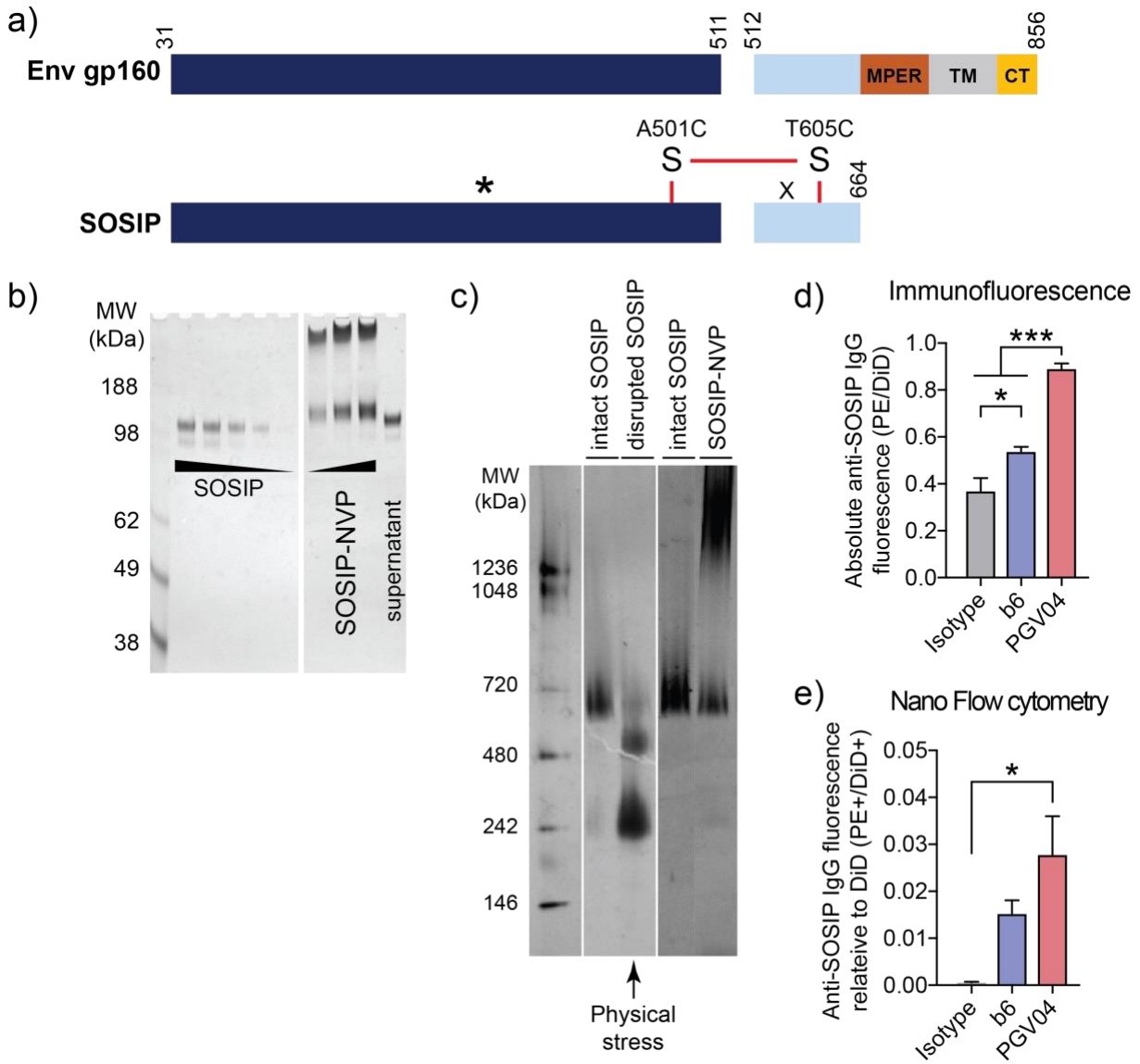

Figure 4-4. BG505.SOSIP.664 (SOSIP) protein and its display on NVP surface after loading. a) Genetic modifications from Env gp160 resulted in SOSIP, having truncation at residue 664, added glycan (indicated by *; T332N) and a disulfide bond, and other point mutations. MPER: membrane proximal region, TM: transmembrane domain, CT: cytosolic tail. **b)** Loading of SOSIP into NVP confirmed by non-reducing PAGE, followed by silver staining. **c)** Blue native PAGE showing intact SOSIP trimer before or after physical disruption as well as after loading in NVP using an optimized formulation condition. **d-e)** To examine SOSIP display on NVP, human anti-SOSIP antibodies, b6 and PGV04, were incubated with SOSIP-NVP and PE-labeled anti-human IgG antibody, followed by quantification of antibody binding by **d)** plate-based fluorescence measurement and **e)** individual nanoparticle-based flow cytometry. Data are presented as mean ± SEM. *$p < 0.05$, ***$p < 0.001$, analyzed by one-way ANOVA, followed by Tukey's HSD multiple comparison post hoc test.

SOSIP-NVP vaccination study in rabbits

We performed immunization studies with SOSIP-NVP and examined their potency to generate neutralizing antibody response in rabbits. White New Zealand rabbits were immunized

on day 0 with 30 µg SOSIP and 50 µg MPLA, followed by two boost immunizations on days 28 and 84, each with 12.4 µg SOSIP and 20.6 µg MPLA (**Figure 4-5a**). SOSIP and MPLA were administered subcutaneously either in SOSIP-NVP or soluble formulations. Sera samples collected on days 28, 56, 105 and 169 were assessed for neutralization against HIV-1 viral entry to TZM-bl cells using heterologous tier 1A virus (MW965.26, clade C) and autologous tier 2 virus (BG505/T332N) (*161, 162*). On Day 56 and more noticeably on Day 105, immune sera from the SOSIP-NVP vaccine group showed strong neutralizing activity against heterologous titer 1A MW965.26 virus (**Figure 4-5b**), with a trend for increasing neutralizing activity compared with the soluble vaccine group. Day 169 immune sera also showed neutralizing activity, although dampened compared with day 105, against MW965.26 (**Figure 4-5b**). As BG505.SOSIP.664 trimer is derived from HIV-1 clade A, our results showing neutralizing activity against MW965.26 HIV-1 clade C virus indicated that SOSIP-NVP elicited a cross-neutralizing antibody response. Furthermore, day 105 immune sera from SOSIP-NVP immunized rabbits exhibited high neutralizing antibody titers against neutralization-resistant tier 2 BG505/T332N virus, whereas the soluble vaccine group induced no neutralizing antibody response (**Figure 4-5c**). Moreover, there was also a trend for higher neutralizing antibody titers against autologous BG505/T332N up to day 169 (**Figure 4-5c**). As it has been challenging to produce vaccines capable of neutralizing against a tier 2 virus, even an autologous one such as BG505/T332N virus, these results show the promise of SOSIP-NVP for vaccination against HIV-1.

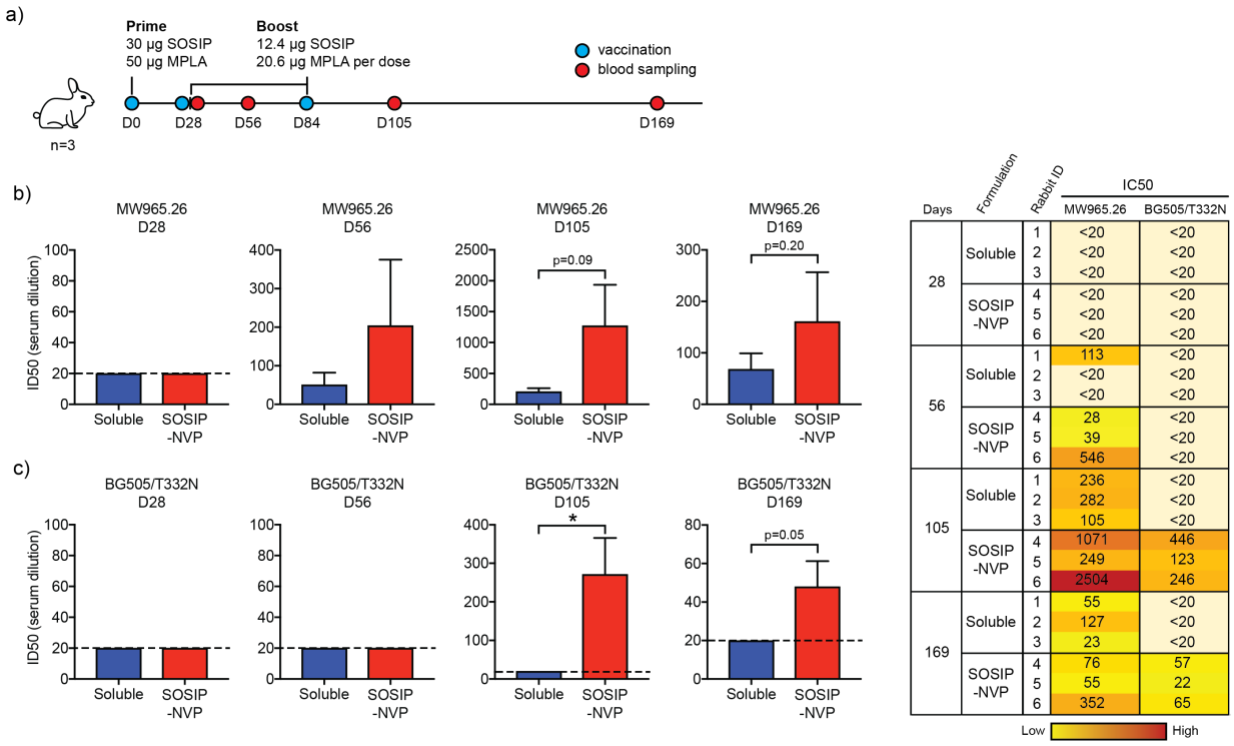

Days	Formulation	Rabbit ID	MW965.26	BG505/T332N
28	Soluble	1	<20	<20
		2	<20	<20
		3	<20	<20
	SOSIP -NVP	4	<20	<20
		5	<20	<20
		6	<20	<20
56	Soluble	1	113	<20
		2	<20	<20
		3	<20	<20
	SOSIP -NVP	4	28	<20
		5	39	<20
		6	546	<20
105	Soluble	1	236	<20
		2	282	<20
		3	105	<20
	SOSIP -NVP	4	1071	446
		5	249	123
		6	2504	246
169	Soluble	1	55	<20
		2	127	<20
		3	23	<20
	SOSIP -NVP	4	76	57
		5	55	22
		6	352	65

Figure 4-5. Vaccination of rabbits using SOSIP-NVP enhances neutralizing antibody titers in sera against homologous virus in vitro. (a) Rabbits were prime vaccinated on D0 and boost vaccinated on D28 and D84, followed by blood sampling on D28, D56, D105 and D169. (**b-c)** Immune sera were analyzed for neutralization of (**b)** tier 1A and (**c)** tier 2 homologous viruses *in vitro*. Data are presented as mean ± SEM. **p* < 0.05, analyzed by unpaired student's t-test.

NVP carrying receptor-binding domain (RBD) of SARS-CoV-2

Motivated by the promising results of SOSIP-NVP, we sought to apply the NVP technology for COVID-19 vaccine development. According to previous studies, the spike protein (S protein) of SARS-CoV-2 is responsible for the interaction with ACE2 receptors on the human cells which leads to viral infection. Inducing antibody response against S protein therefore is an effective strategy to neutralize SARS-CoV-2 (*42*, *148*). The receptor-binding domain (RBD) is the functional region within the S protein that engages ACE2, and has been suggested as a great target for vaccines against SARS-CoV-2 (*149*, *150*). In addition, our analysis on genetic sequence comparison between SARS-CoV-2 variants reported on National Center for Biotechnology Information (NCBI) as of August 2020 and the original SARS-CoV-2 that appeared in Wuhan in

2019 indicated high conservation of RBD genetic sequence, compared with other genetic regions (**Figure 4-6a,b**), thus highlighting RBD as a promising target for COVID-19 vaccine development.

We synthesized RBD-loaded NVP as described above. Loading of RBD in NVP was quantified by PAGE analysis, which showed ~21% loading efficiency (**Figure 4-6c**). The resulting RBD-loaded NVP (RBD-NVP) had a hydrodynamic size of ~240 nm as measured by DLS (**Figure 4-1b**). Surface-display of RBD on RBD-NVP was examined by direct immunofluorescence as described. RBD-NVP was incubated with human RBD neutralizing antibodies, followed by washing and addition of AF488-labeled anti-human IgG secondary antibody. RBD-NVP exhibited a significantly higher fluorescence signal, compared with blank NVP control (**Figure 4-6d**), indicating the proper display of RBD and preservation of epitopes in RBD-NVP.

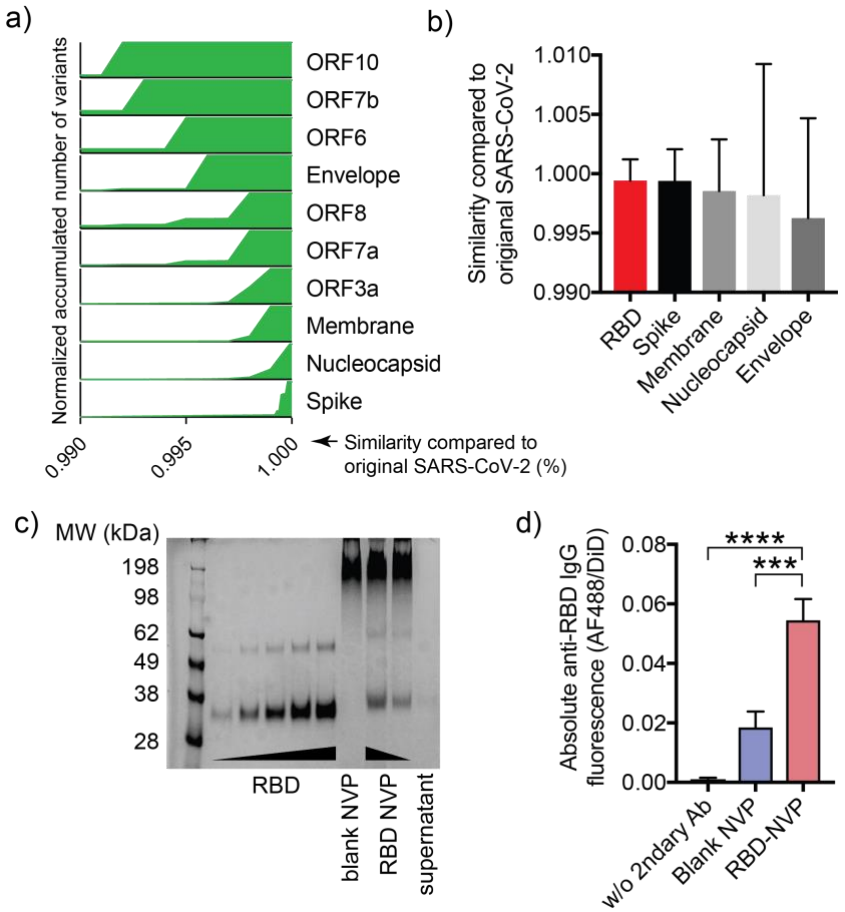

Figure 4-6. Genomic deviation of SARS-CoV-2 by coding region and characterization of RBD-NVP. (a) Spike protein is the most genetically conserved region within the genetic sequence of SARS-CoV-2, based on variants appearing with near 100% similarity to the original SARS-CoV-2 in this region. **(b)** RBD of SARS-CoV-2 variants has the highest sequence similarity to that of the original SASR-CoV-2 with the smallest deviation, compared with other domains. **(c)** RBD loading in NVP was confirmed by SDS-PAGE analysis. **(d)** RBD display on NVP surface was assessed by incubation with human anti-SARS-CoV-2 neutralizing antibody, followed by incubation with Alexa Fluor 488-labeled anti-human IgG1 Fc secondary antibody. Antibody bound to NVP was quantified by fluorometry. Data are presented as mean ± SEM. ***$p < 0.001$, ****$p < 0.0001$, analyzed by one-way ANOVA, followed by Tukey's HSD multiple comparison post hoc test.

RBD-NVP vaccination study in mice

Lastly, we examined the potency of RBD-NVP to generate anti-RBD antibody response in mice. BALB/c mice were vaccinated three times with 2 weeks interval between each injection (days 0, 14, and 28) using 0.5 μg of RBD and 1 μg of MPLA either in NVP or soluble formulation (**Figure 4-7a**). Sera samples were collected on days 28, 42, and 70 and assessed for RBD-specific serum IgG, IgG_1, and IgG_{2a} titers. RBD-NVP generated significantly higher RBD-specific antibody titers, compared with RBD + MPLA soluble vaccine (**Figure 4-7b-d**). Specifically, by day 42 (2 weeks after 3rd vaccination), RBD-NVP elicited 55-fold, 17-fold, and 284-fold higher RBD-specific IgG, IgG_1, and IgG_{2a} titers, respectively, compared with the soluble vaccine (**Figure 4-7b-d**). By day 70 (6 weeks after 3rd vaccination), mice immunized with RBD-NVP still maintained 30-fold, 13-fold, and 671-fold higher RBD-specific IgG, IgG_1, and IgG_{2a} titers, respectively, compared with the soluble vaccine group (**Figure 4-7b-d**). While the examination of functionality and neutralizing activities of these antibodies are beyond the scope of our current studies, these initial results indicated that RBD-NVP induced robust, long-lasting, Th1/Th2-balanced antibody responses against RBD.

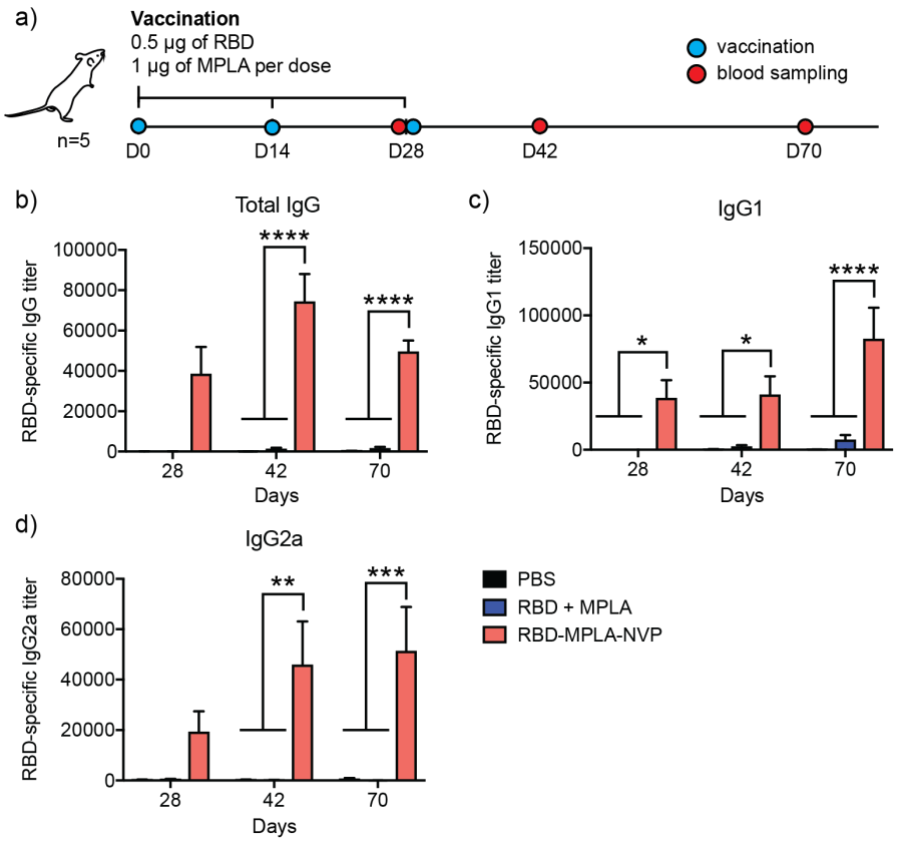

Figure 4-7. RBD-NVP elicits robust RBD-specific antibody responses in mice. (a) BALB/c mice were vaccinated three times, with 2 weeks intervals between each injection. Blood was sampled on the indicated days. RBD-NVP significantly increased serum antibody titers of RBD-specific **(b)** IgG, **(c)** IgG1, and **(d)** IgG2a, compared to the soluble vaccine. Data are presented as mean ± SEM. *$p < 0.05$, **$p < 0.01$, ***$p < 0.001$ and ****$p < 0.0001$, analyzed by two-way ANOVA, followed by Tukey's HSD multiple comparison post hoc test.

4.5. Conclusion

Overall, we have developed NVP for the delivery of protein antigens and demonstrated the versatility of NVP for protein-based vaccination against infectious pathogens. Protein antigens incorporated into NVP maintained the configuration of the epitopes, as shown by the recognition and binding of neutralizing antibodies on the surfaces of antigen-displaying NVP. NVP was readily taken up by DCs *in vitro*, leading to greater DC activation and antigen presentation, compared with soluble vaccine formulation. We have successfully prepared NVP carrying SOSIP derived from HIV-1 and RBD derived from SARS-CoV-2. Animals immunized with NVP

generated strong antigen-specific antibody responses. While these initial proof-of-concept studies have shown the promise of NVP, more studies are warranted to delineate the immunological mechanisms of action and to assess protective immunity against viral challenge (e.g., HIV-1 or SHIV challenge in non-human primates; and SARS-CoV-2 challenge in mice engineered to express human ACE2).

CHAPTER V. Prebiotics Treatment for Modulation of Gut Microbiota and Improvement of Cancer Vaccine Efficacy

5.1. Abstract

It has long been known that diet has close relationship with the state of gut microbiota. Many dietary fibers are the sources for fermentation by the gut bacteria, which produce metabolites that have influence on the host in diverse aspects. Recent reports stating the close correlations between the gut microbiota and onset of diseases that were considered to be difficult-to-treat, such as cancer, autistic and autoimmune diseases, drew a lot of attention from various fields of study. Especially, the findings of bacterial metabolites called short chain fatty acids (SCFA) influencing the immune responses following therapeutic interventions sparked a huge interest in the field of cancer immunotherapy. Here, we sought to use engineering approaches to enhance the immune response after vaccination, by including prebiotics in the diet in an attempt to modulate the gut microbiota. Tested with mouse tumor models, several prebiotics such as potato starch and fructo-oligosaccharide were found to induce changes in gut bacterial frequencies and subsequent immune responses after vaccination, which resulted in enhanced vaccine efficacy in terms of tumor growth suppression.

5.2. Introduction

The microbiome is a collection of genes from trillions of microorganisms living inside an individual human. Each organ inside the body has its own unique microbiota developed, all of which have been known to have great impact on general human health. Gut microbiota has been one of the most extensively studied among others. Since 2010, an avalanche of studies reported the relationship between the gut microbiota and health and disease onset of other organs of the body (*163*). Especially, there are many recent studies reporting close relationships between the host gut microbiota and the immune system, where both members of the innate and adaptive immunity are found to be strongly influenced. Consumption of dietary fibers diversifies bacteria in the gut, which subsequently influences various members of the immune system, including dendritic cells, macrophages, regulatory T cells and memory T cells (*55, 164, 165*). Also, there are accumulating reports of certain bacterial species and their metabolites modulating patients' responses to immunotherapies (*166, 167*).

For the communication between microbiota and immune system, the metabolites of bacteria called short chain fatty acids (SCFA) act as one of the crucial mediators (*55, 164*). When bacteria metabolize, the metabolites called short chain fatty acids (SCFA) are released, which act as a mediator for the cross-talk between the gut microbiota and the immune system, ultimately contributing to therapeutic outcomes during cancer immunotherapy (*168, 169*). In the similar context, consuming dietary fibers, or prebiotics, which bacteria metabolize on has also been found to be important for the general health and immunity of an individual. With recent findings of SCFA acting as an important factor for the generation and potency of memory T cells, there are increasing interests in the field of immunology to investigate the effects of microbiota and T cell immune responses (*165*). However, despite the reports suggesting potential connections between the diet,

microbiota and immune responses (*166, 167*), there have not yet been studies of how the diet influences T cell responses after vaccination in cancer prophylactic/therapeutic settings. Here, we investigated the effects of prebiotics consumption on microbiota and how the changes in microbiota influence the T cell response generated by vaccination against cancer using a mouse tumor model. There are many prebiotics known to have effects on gut microbiome when consumed, such as inulin (*170, 171*), metformin (*172-174*), pectin (*175, 176*) and potato starch (*177*). Prior to tumor inoculation, these prebiotics were given by oral gavage followed by vaccination. Many of the prebiotics that were tested were shown to have influence on bacterial composition in the gut, including the increase in *Akkermansia* frequency, which has been found to be closely related to host's immune response during cancer immunotherapy (*168*).

5.3. Materials and Methods

Animal studies

Animals were cared for following federal, state, and local guidelines. All experiments performed on animals were in accordance with and approved by the Institutional Animal Care and Use Committee (IACUC) at the University of Michigan, Ann Arbor. BALB/c mice (n=5 per group) were given oral gavages with prebiotics using below indicated amounts:

	Experiment #1		**Experiment #2**	
Vaccination: Adpgk HDL (15.5 nmol + 2.3 nmol CpG); injected s.c. at tail-base	Water	NA	Water	NA
	Inulin	120 mg	Inulin gel	60 mg
	Metformin	6 mg	FOS	150 mg
	Pectin	10 mg	Potato starch gel	30 mg
	Fucoidan	4 mg	-	-

	Fructo-oligosaccharide (FOS)	120 mg	-	-
No vaccination	Water	NA	Water	NA

*Indicated doses are amount per gavage given to each mouse.

Oral gavages were given using 22-gauge gavage needles (Cadence Science™) once every 2 days for 47 days (experiment #1) or for 8 days (experiment #2). Each gavage volume was fixed to 100 µl. Vaccinations were given subcutaneously at the tail-base, injected on both sides with 50 µl injection volume per side. For serum IgG detection study, OVA (100 µg) and Alum (Alhydrogel, Fisher Scientific, 50% of total injection volume) (instead of the adpgk-HDL formulation) were given as vaccination. Fecal samples were collected at indicated time points using 1.5 mL centrifugal tubes, placed in dry ice immediately after collection. Blood samples were collected via submandibular vein using lancets. Collected blood samples were used for analyses using flow cytometry and ELISA.

ELISA for serum IgG titer measurement

Mouse immune sera were analyzed for adpgk-specific IgG antibody titers using ELISA. Briefly, ovalbumin was coated on 96-well ELISA plates (1 µg/well) and serially diluted sera samples were added. After 1 hr of incubation and multiple washings, horse radish peroxidase (HRP)-labeled secondary antibodies were added and further incubated for 1 hr in room temperature. Rabbit anti-mouse IgG H&L-HRP (Abcam) was used as the secondary antibody. Next, TMB substrate solution (Thermo Scientific) was added, and the reaction was stopped by the addition of H_2SO_4. The absorbance was measured at a 450 nm wavelength using a plate reader (Synergy Neo, BioTek). To measure antibody titers, titration curves were drawn based on the absorbance and the dilution factor, from which half maximal effective concentration (EC50) values were calculated using Prism 7 software.

Flow cytometry for analysis of antigen-specific CD8+ T cells in blood

Red blood cells in the collected blood samples were removed by mixing with ACK lysis buffer (Life Technologies). After centrifugation at 500 g for 5 min, pallet was washed with PBS twice. Resulting PBMCs were stained with a live/dead staining dye (eBioscience), followed by mixing with Fc-receptor blocking antibody (anti CD16/32) and fluorophore-labeled antibodies including CD3-FITC (Biolegend), CD8-APC (BD Biosciences), and Adpgk tetramer-PE (NIH Tetramer Core Facility). Resulting cells were fixed with 2% formaldehyde for 10 min, and then suspended in FACS buffer for flow cytometry.

Statistical analysis

The results are expressed as means ± SEM. Prism 7.0e (GraphPad Software) software was used for statistical analyses. Statistical comparisons were performed using one-way or two-way ANOVA, followed by Tukey's HSD multiple comparison test or Sidak's multiple comparison test, as indicated. The survival curves were analyzed by the log-rank (Mantel−Cox) test. Statistical significances are indicated as $*p < 0.05$, $**p < 0.01$, $***p < 0.001$, and $****p < 0.0001$.

5.4. Results

Effects of prebiotics on CD8+ T cell responses after vaccination were examined using BALB/c mice (n=5 per group). Mice were acclimated for a week to stabilize gut microbiota. Oral gavages with prebiotics were given bi-daily using gavage needles with each gavage volume of 100 µl. Doses of prebiotics are indicated in the methods section. 7 days into the gavage period, mice were vaccinated subcutaneously at the tail-base with HDL nanodiscs containing CpG (2.3 nmol)

and adpgk peptide (15.5 nmol). Booster injections were given twice with 2 weeks intervals. MC38 tumor cells were injected on day 47 which was the last day of prebiotics treatment. Blood samples were collected on days 14, 28, 40 and 54 for flow cytometric analyses on peripheral CD8+ T cells. Fecal samples were collected on day 7 (**Figure 5-1a**). Using blood samples, adpgk-tetramer staining analysis was performed on CD8+ T cells (**Figure 5-1b**). All treatment groups including water-treated group that was not given prebiotics showed increase in peripheral frequency of antigen-specific CD8+ T cells over time. Although statistically significant difference between water-treated and any of the prebiotics-treated groups was not observed, there were trends of shifts in adpgk-specific CD8+ T cell levels that fluctuated over time. Mostly, the water-treated group showed the trend of lowest frequency, indicating that it is likely that prebiotics treatment has an impact on CD8+ T cell responses after vaccination. Similarly, effector and memory T cell formation showed trends of variances depending on prebiotics treatment, albeit without statistical significance (**Figure 5-1c**). Serum IgG levels were measured using ELISA (**Figure 5-2d**). Again, trends of variance between treatment groups were observed without statistical significance, where we were able to assume that prebiotics treatment indeed has influence on immune responses including CD8+ T cell and serum antibody.

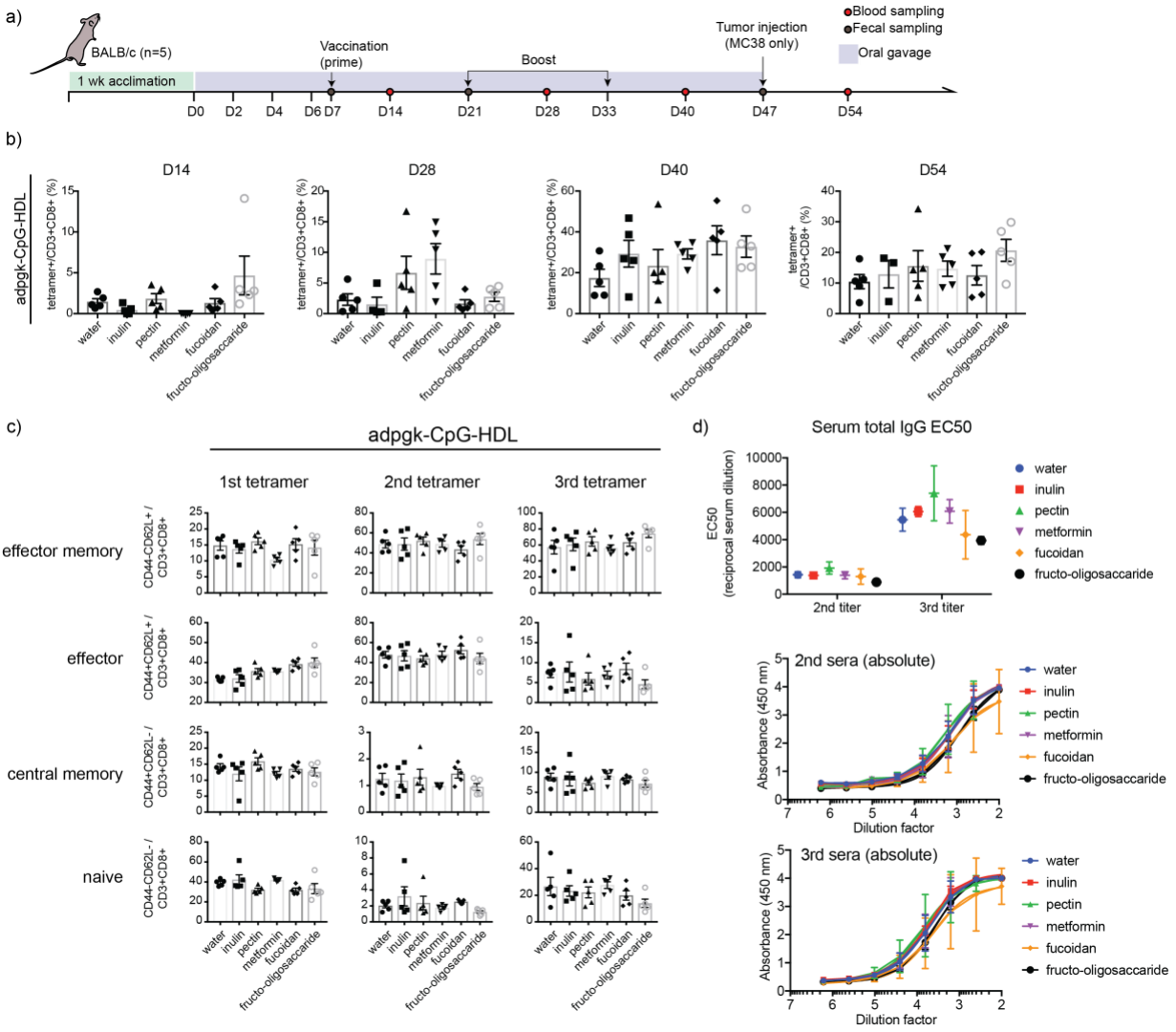

Figure 5-1. Effects of prebiotics on cellular and humoral immune responses induced by vaccination. (**a**) Schematic of experiment timeline. Mice (n=5 per group) were given three times of vaccination (prime and two boosters) on days 7, 21 and 33, while they were given oral gavages of prebiotics every two days for 47 days. Fecal samples were collected on day 7 and blood samples were collected on days 14, 28, 40 and 54. (**b**) adpgk-tetramer staining using blood samples collected on indicated dates, analyzed with flow cytometry. (**c**) Analysis of effector and memory cell transition by peripheral CD8+ T cells over time, measured by flow cytometry. (**d**) Serum IgG levels indicated in EC50 of reciprocal serum dilution, measured by ELISA.

In order to investigate how prebiotics have influenced the immune responses, fecal samples were analyzed to investigate the microbiome using 16S RNA sequencing. Among 125 bacterial species analyzed, noticeable shifts were observed from several species including *Alistipes*, *Akkermansia*, *Lachnospiraceae*, *Bacteroides* and *Turicibacter* (**Figure 5-2a**). Interestingly,

Akkermansia, which is reported to be beneficial for colonic mucin and overall gut health (*178-180*), showed trends of increase in metformin- and pectin-treated groups. In order to investigate if the impact on gut microbiota by prebiotics treatment has influence on anti-tumor vaccine efficacy, the mice that were given prebiotics and vaccinations were challenged with subcutaneous injections of MC38 mouse colon carcinoma cells on day 47, and the tumor growths were monitored (**Figure 5-2b**). Interestingly, tumor growth suppression had trends of enhancement when prebiotics were given together with vaccination to tumor-bearing mice. FOS, metformin and inulin were shown to have significant enhancement compared to other prebiotics. Although a noticeable survival benefits were not observed (**Figure 5-2c**), the results indicate that prebiotics treatment have impacts on gut microbiome which subsequently influences on host's immune responses after prophylactic vaccination against tumor.

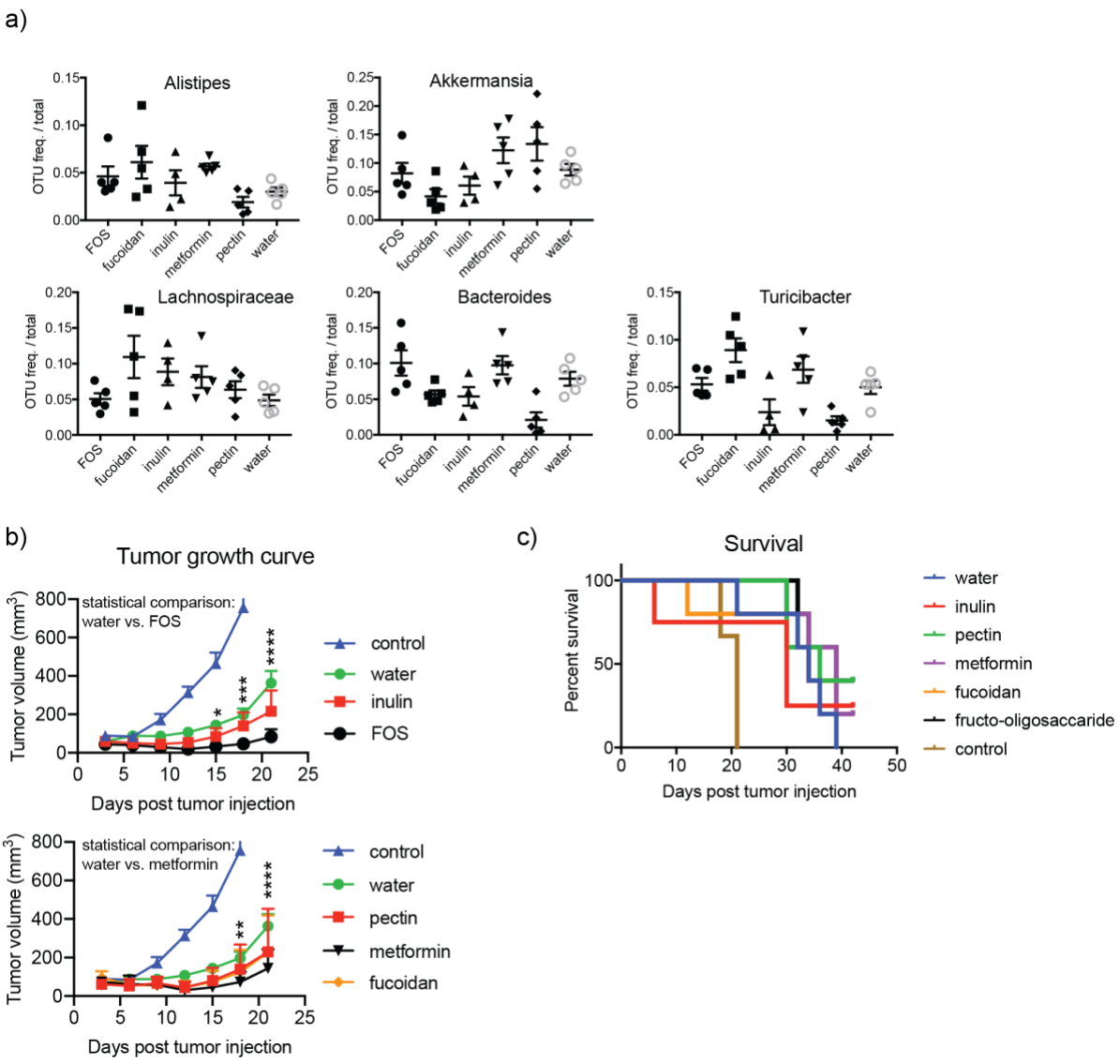

Figure 5-2. Changes in gut microbiome and their effects on vaccine efficacy in tumor-bearing mice. (a) Several gut bacterial species with trends of deviance compared to water-treated group are shown. Tumor growth curve (**b**) and survival (**c**) of tumor-bearing mice that were given oral gavages of any one of water, inulin, FOS, pectin, metformin or fucoidan in combination with vaccination. Control group was given oral gavages of water without vaccination. For statistical analysis shown in (**b**), the top panel compares between 'water' and 'FOS', and the bottom panel compares between 'water' and 'metformin'. Data are presented as mean ± SEM. *$p < 0.05$, **$p < 0.01$, ***$p < 0.001$, and ****$p < 0.0001$, analyzed by two-way ANOVA followed by Sidak's multiple comparisons test.

Next, a similar animal study was designed, this time with a therapeutic setting. Oral gavage period was given for 8 days, which was shortened compared to the previous gavage period of 47 days, based on a study reporting rapid change of microbiota of mice that occurs around 7 days

after cohousing in a different environment (*181*). These mice were inoculated subcutaneously on the right-side thigh on day 0 with MC38 cells. 4 days later, mice were given primary vaccination with adpgk-CpG-HDL (15.5 nmol adpgk + 2.3 nmol CpG). Two booster injections with the same dose, each given weekly. Fecal samples were collected on day 6 for microbiome analysis. Blood samples were collected on days 11, 18, 25 and 32 for adpgk-tetramer analysis on peripheral CD8+ T cells (**Figure 5-3a**). Similar to the previous experiment, trends of increase in antigen-specific CD8+ T cells were observed in peripheral blood until day 18, but not on day 25 and after (**Figure 5-3b**). It may have been due to the long period of time since the cessation of oral gavages of prebiotics after day 18, which may result in normalization of gut microbiome between the sample groups.

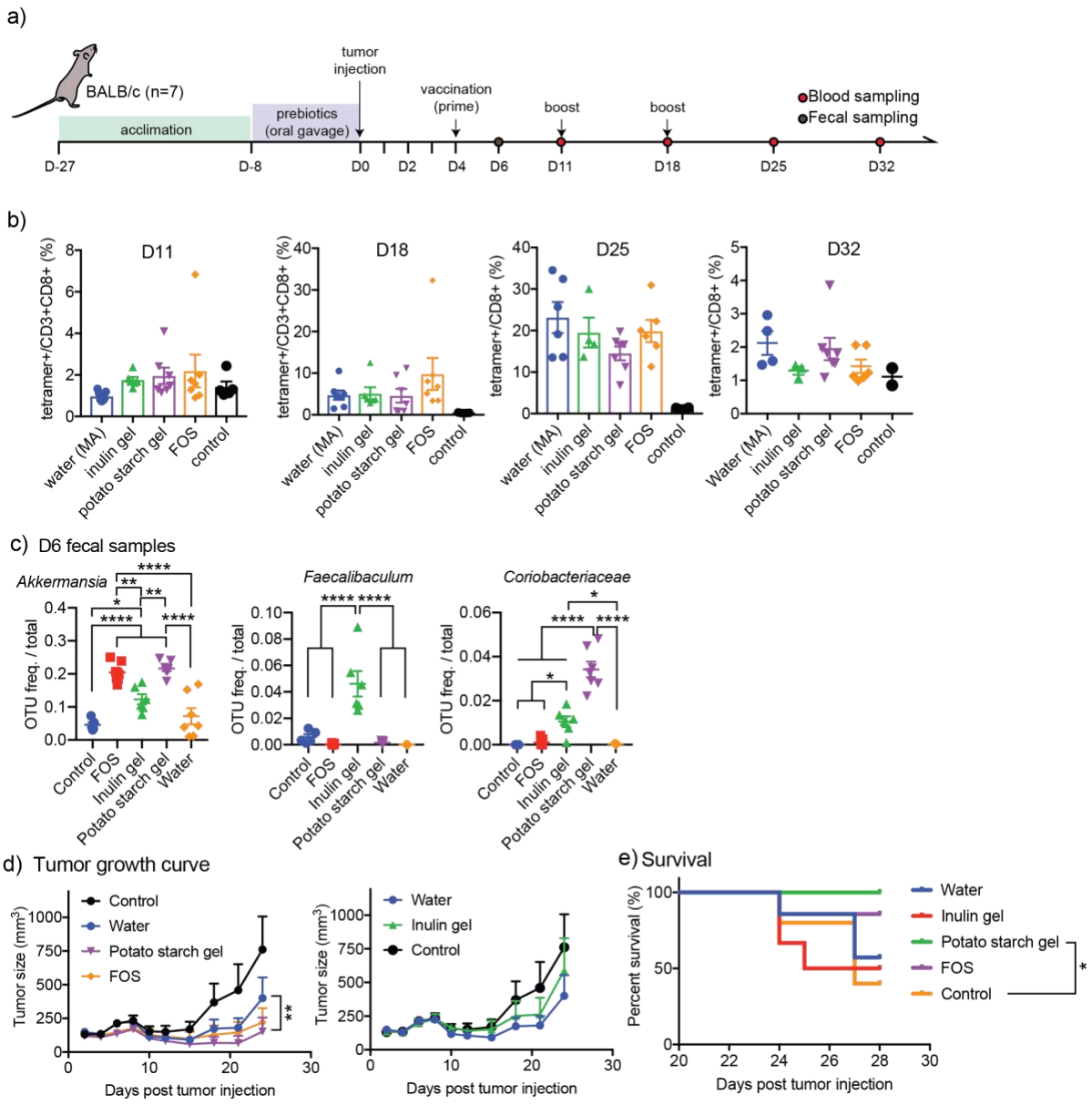

Figure 5-3. Effects of prebiotics on therapeutic efficacy of vaccination against tumor. (a) Timeline of study. BALB/c mice (n=7) were given prebiotics every two days for 8 days, followed by tumor injection using MC38 mouse colon carcinoma cells. 4 days after, mice were given vaccination once every week for three times. Fecal samples were collected on day 6, and blood samples were collected on days 11, 18, 25 and 32. (**b**) adpgk-tetramer staining on CD8+ T cells in peripheral blood, measured by flow cytometry. (**c**) 16S RNA sequencing data of fecal samples. Bacterial species that showed most noticeable changes are shown. (**d**) Tumor growth and (**e**) survival of tumor-bearing mice that received with or without vaccination and prebiotics treatment. For statistical analysis shown in (**d**), left panel compares between 'water' and 'potato starch gel'. Data are presented as mean ± SEM. *$p < 0.05$, **$p < 0.01$, and ****$p < 0.0001$, analyzed by **c)** one-way ANOVA followed by Tukey's HSD multiple comparison post hoc test or **d)** two-way ANOVA followed by Sidak's multiple comparisons test. **e)** The survival curves were analyzed by the log-rank (Mantel−Cox) test.

Fecal samples were analyzed with 16S RNA sequencing to investigate the changes in gut bacterial frequencies (**Figure 5-3c**). There were noticeable changes in several species of bacteria, including *Akkermansia*, *Faecalibaculum* and *Coriobacteriaceae*, depending on the prebiotics given. Interestingly, changes in *Akkermansia* were again observed as was in the previous study, indicating the potential positive effects of the tested prebiotics on the gut health. In line with the tetramer-staining study and changes observed in gut microbiome, mice given prebiotics showed trends of enhanced vaccine efficacy against tumor, correlating with increased survival of the tumor-bearing mice (**Figure 5-3d,e**).

5.5. Conclusion

Overall, we were able to observe the effects of prebiotics on vaccination efficacy against tumor, by the trends of changes in gut microbiome and in both cellular and humoral immune responses. Most importantly, despite the changes showing only the trends of changes that require multiple rounds of additional experiments to confirm reproducibility of the results with statistical significance, the efficacies of vaccines both in prophylactic and therapeutic settings showed enhancement when the tested animals were given oral gavages of certain prebiotics (e.g., potato starch, FOS, etc.). It states the possibility of diet-based preconditioning being included in the cancer therapeutic regimens and the importance of healthy diet that includes dietary fibers to maintain gut microbiota in a state that is beneficial for the prevention of neoplasm. Also, the study warrants further studies to investigate the effects of bacterial metabolites that are produced within the microbiota that is changed after prebiotics consumption.

CHAPTER VI. Conclusions and Perspectives

There is an overarching aim that is shared between the studies described thus far, which is modulating the immune response to achieve enhancement of therapeutics or prophylaxis. Immune responses can be perceived as a cycle that begins with recognition of antigen and danger signals by innate immune response that leads to activation of adaptive immune response, where modulation at a certain stage may bolster the cycle, leading to stronger overall immune responses. Our studies used biomaterials to target a certain stage of immune response cycle that depended on the type of material used, kind of therapeutic or prophylaxis, administration route and target disease.

In the first study, bMSN-mediated STING agonist delivery increased cellular uptake of STING agonist that enhanced STING activation of dendritic cells, subsequently leading to improved therapeutic outcomes of STING agonist treatment in mouse melanoma models. Here, we expect the large-sized pores of bMSN will not only enable the fast degradation of bMSN after administration, but also provide a possibility for larger-sized biomolecules, such as protein, to be loaded in bMSN which would make the system applicable to other therapeutic settings. Also, utilizing well-known silica surface modification chemistries may allow multiple kinds of biomolecules to be co-loaded, further diversifying the application scenarios. Meanwhile, the current study was done using mouse melanoma model, where the tumor was easily accessible for direct injections of bMSN loaded CDA, after which the presumed acidic tumor microenvironment

allows prolonged CDA release. However, there are many situations where tumors are not readily accessible for direct injections, in which case, other routes of drug administration should be considered. Intravenous injection is one of the commonly used routes of injection, where passive drainage of drug or delivery particles occurs to the sites of tumor via enhanced permeability and retention (EPR) effect (*182, 183*). In this case, the administered therapeutics are exposed to and interact with components, including albumins, present in the blood circulation, causing clearance at different parts of the body such as liver and kidney (*184*). It would be a great direction to pursue forward to modify the surface of bMSN, such as lipid- or polyethylene glycol-coating, to increase stability in blood circulation which would provide other possible routes of administration.

The next study introduced combination of nanoparticle vaccine and STING agonist for cancer immunotherapy. The nanoparticle vaccine was used to enhance the potency of a neoantigen peptide vaccine, while STING agonist treatment induced stronger release of T cell attractant chemokines from tumors, leading to increased tumor infiltration by the vaccine-induced T cells. The combination treatment was strategically designed to overcome suboptimal tumor infiltration by T cells, a limitation frequently faced by vaccines designed for cancer immunotherapy. Causes that lead to such limitation and were attempted to be solved in the study include sequestration of T cells at the vaccine depot which is often formed when certain types of vaccine delivery platforms are used, and minimal expression of chemokines by the tumor (*185-187*). Importantly, the concept of recruiting circulating T cells to tumor may be applicable in different settings such as when T cells are adoptively transferred, which also increases the available number of T cells in the blood circulation (*188*). However, while STING agonist has worked out nicely in the current study, sensitivity to STING agonist treatment varies by the tumor types where excessive dose of treatment may cause suboptimal immune responses (*71*), requiring dose optimizations. Therefore, it would

also be worthwhile to test other types of drugs that may substitute STING agonist to achieve similar effects for flexibility of adopting the idea of T cell recruitment in other therapeutic settings involving different types of tumor. For example, there are studies investigating the recruitment of circulating T cells to tumor, adopting the concept of vascular checkpoints where extravasation of T cells is controlled using various agents, such as cisplatin, temozolomide, or other anti-angiogenic agents (*105, 188-190*).

Next discussed was lipid-based nanoparticle mediated protein subunit vaccine delivery as prophylaxis against infectious diseases, where the vaccine was codelivered with an adjuvant, MPLA, to enhance activation and antigen presentation by dendritic cells, which together with increased lymph node trafficking after subcutaneous administration induced stronger humoral immune responses in mice and rabbits. Another emphasis put in the study was maintaining the tertiary and quaternary structures of the protein antigens during the loading process into nanoparticles, since it is critical to the generation of neutralizing antibodies that are able to neutralize the pathogens after vaccination (*191*). The study involved various ways to examine the conformational intactness of the protein antigens after incorporation into the nanoparticle, such as non-reduced SDS-PAGE, native blue PAGE, and neutralizing antibody treatment followed by flow cytometric analysis. From the previous generations of the lipid nanoparticles with similar multilamellar lipid structures (*152-154*), the current version excluded the use of excessive physical stress and reducing agents after protein antigens were added to the reaction mixture, in order to prevent the structural disruptions that may occur. As a result, two different kinds of proteins, each having internal disulfide bonding and/or trimeric structure, were successfully loaded in the nanoparticle with great loading efficiencies (20~25%), demonstrating the applicability of the system to delivering various proteins with different structural characteristics. However, while the

generation of IgG antibodies in serum of vaccinated mice and rabbits have been confirmed, further studies are warranted for the validation of IgG-mediated neutralization of pathogens both *in vitro* and *in vivo* settings.

Lastly, the effects of prebiotics consumption on gut microbial composition and subsequent immune response after vaccination was investigated using a mouse tumor model. Many studies reporting the correlations between the gut microbiota and various immune cell types provided the motivation to this project. Here, controlling the diet through consumption of prebiotics was proposed as a means for modulating the immune responses based on the links between prebiotics consumption, gut microbiota, and the immune system. Using mouse models, changes in gut bacterial composition upon oral delivery of prebiotics, including inulin, potato starch, fructo-oligosaccharide and metformin, were observed. Together with the impact given to gut microbiota, we observed trends of enhancements in cellular and humoral immune responses upon vaccination, which correlated with improved the potency of vaccines treated in either prophylactic or therapeutic settings. Overall, the study provided a promising strategy for immune modulation that provides possibility of applying to other therapeutic settings. However, the duration of oral gavage adopted in the two studies were either relatively short or the gavage was seized after tumor challenge, from which point the gut microbiota may normalize back to the initial state. Therefore, it warrants additional studies of how prolonging the duration of prebiotics treatment may influence the microbiota and the immune responses. Also, the bacterial metabolites, SCFA, are in part responsible for the effects the bacterial community provides to the immune cells, and therefore should also investigated in detail in future studies (*53, 55, 58, 192*).

Overall, here in the thesis, various ways of immune modulation for treating cancer and preventing infectious diseases were introduced. While some of the studies were more directed

towards proof-of-concept, others were focusing on the clinical translatability. Altogether, the future direction to which all our studies should be pursuing onward is getting thorough mechanistic insights in terms of how the immune system reacts to the therapeutic/prophylactic inputs given by our systems, such as nanoparticle mediated vaccine and drug delivery, intratumoral STING agonist treatment, and prebiotics treatment. Tracking the drug or delivery particles after administration in longer terms, analyzing the immune response bias to Th1 or Th2 responses, and investigating other cell types that are also important during immune responses, such as macrophages and B cells, would provide clearer vision of how the therapeutic outcomes can be expected in clinical settings. With these clearly defined, our systems may provide great bases for combination therapies with other potent immunotherapeutics, such as immune checkpoint inhibitors and adoptive cell transfer of T cells and DCs. With currently available immunotherapies, still a large portion of patients fails to achieve complete responses (*193, 194*). Our studies may provide alternative therapeutic methods that are practical and effective to patients that are refractory to previous treatments.

BIBLIOGRAPHY

1. P. Darvin, S. M. Toor, V. Sasidharan Nair, E. Elkord, Immune checkpoint inhibitors: recent progress and potential biomarkers. *Exp Mol Med* **50**, 1-11 (2018).

2. Q. Duan, H. Zhang, J. Zheng, L. Zhang, Turning Cold into Hot: Firing up the Tumor Microenvironment. *Trends Cancer* **6**, 605-618 (2020).

3. G. W. Tormoen, M. R. Crittenden, M. J. Gough, Role of the immunosuppressive microenvironment in immunotherapy. *Adv Radiat Oncol* **3**, 520-526 (2018).

4. A. Labani-Motlagh, M. Ashja-Mahdavi, A. Loskog, The Tumor Microenvironment: A Milieu Hindering and Obstructing Antitumor Immune Responses. *Front Immunol* **11**, 940 (2020).

5. N. A. Rizvi *et al.*, Mutational landscape determines sensitivity to PD-1 blockade in non–small cell lung cancer. *Science* **348**, 124-128 (2015).

6. B. Zhao, H. Zhao, J. Zhao, Efficacy of PD-1/PD-L1 blockade monotherapy in clinical trials. *Ther Adv Med Oncol* **12**, 1758835920937612 (2020).

7. T. Powles *et al.*, MPDL3280A (anti-PD-L1) treatment leads to clinical activity in metastatic bladder cancer. *Nature* **515**, 558 (2014).

8. P. Y. Teo *et al.*, Ovarian cancer immunotherapy using PD-L1 siRNA targeted delivery from folic acid-functionalized polyethylenimine: strategies to enhance T cell killing. *Adv Healthc Mater* **4**, 1180-1189 (2015).

9. W. Zou, J. D. Wolchok, L. Chen, PD-L1 (B7-H1) and PD-1 pathway blockade for cancer therapy: Mechanisms, response biomarkers, and combinations. *Sci Transl Med* **8**, 328rv324 (2016).

10. Z. Mei, J. Huang, B. Qiao, A. K. Lam, Immune checkpoint pathways in immunotherapy for head and neck squamous cell carcinoma. *Int J Oral Sci* **12**, 16 (2020).

11. M. Bethune, A. Joglekar, Personalized T cell-mediated cancer immunotherapy: progress and challenges. *Current Opinion in Biotechnology* **48**, 142-152 (2017).

12. C. H. June, R. S. O'Connor, O. U. Kawalekar, S. Ghassemi, M. C. Milone, CAR T cell immunotherapy for human cancer. *Science* **359**, 1361-1365 (2018).

13. N. P. Restifo, M. E. Dudley, S. A. Rosenberg, Adoptive immunotherapy for cancer: harnessing the T cell response. Nat Rev Immunol 12, 269-281 (2012).

14. S. A. Rosenberg, N. P. Restifo, Adoptive cell transfer as personalized immunotherapy for human cancer. Science 348, 62-68 (2015).

15. T. J. Fry et al., CD22-targeted CAR T cells induce remission in B-ALL that is naive or resistant to CD19-targeted CAR immunotherapy. Nature Medicine 24, 20-+ (2018).

16. S. L. Maude et al., Chimeric Antigen Receptor T Cells for Sustained Remissions in Leukemia. New England Journal of Medicine 371, 1507-1517 (2014).

17. T. N. Schumacher, R. D. Schreiber, Neoantigens in cancer immunotherapy. Science 348, 69-74 (2015).

18. Z. Hu, P. A. Ott, C. J. Wu, Towards personalized, tumour-specific, therapeutic vaccines for cancer. Nat Rev Immunol 18, 168-182 (2018).

19. U. Sahin, O. Tureci, Personalized vaccines for cancer immunotherapy. Science 359, 1355-1360 (2018).

20. L. Scheetz et al., Engineering patient-specific cancer immunotherapies. Nat Biomed Eng 3, 768-782 (2019).

21. Y. Fang et al., A pan-cancer clinical study of personalized neoantigen vaccine monotherapy in treating patients with various types of advanced solid tumors. Clin Cancer Res, (2020).

22. X. Chen, J. Yang, L. Wang, B. Liu, Personalized neoantigen vaccination with synthetic long peptides: recent advances and future perspectives. Theranostics 10, 6011-6023 (2020).

23. Y. Guo, K. Lei, L. Tang, Neoantigen Vaccine Delivery for Personalized Anticancer Immunotherapy. Front Immunol 9, 1499 (2018).

24. P. A. Ott et al., An immunogenic personal neoantigen vaccine for patients with melanoma. Nature 547, 217-221 (2017).

25. B. Sun, H. Hyun, L. T. Li, A. Z. Wang, Harnessing nanomedicine to overcome the immunosuppressive tumor microenvironment. Acta Pharmacol Sin 41, 970-985 (2020).

26. J. Nam et al., Cancer nanomedicine for combination cancer immunotherapy. Nature Reviews Materials 4, 398-414 (2019).

27. M. J. Mitchell et al., Engineering precision nanoparticles for drug delivery. Nat Rev Drug Discov, (2020).

28. S. Azzi, J. K. Hebda, J. Gavard, Vascular permeability and drug delivery in cancers. Front Oncol 3, 211 (2013).

29. V. Mollica Poeta, M. Massara, A. Capucetti, R. Bonecchi, Chemokines and Chemokine Receptors: New Targets for Cancer Immunotherapy. Front Immunol 10, 379 (2019).

30. M. T. Chow, A. D. Luster, Chemokines in cancer. Cancer Immunol Res 2, 1125-1131 (2014).

31. G. E. Idos et al., The Prognostic Implications of Tumor Infiltrating Lymphocytes in Colorectal Cancer: A Systematic Review and Meta-Analysis. Sci Rep 10, 3360 (2020).

32. C. Jochems, J. Schlom, Tumor-infiltrating immune cells and prognosis: the potential link between conventional cancer therapy and immunity. Exp Biol Med (Maywood) 236, 567-579 (2011).

33. M. Hong et al., Chemotherapy induces intratumoral expression of chemokines in cutaneous melanoma, favoring T-cell infiltration and tumor control. Cancer Res 71, 6997-7009 (2011).

34. N. Garbi, B. Arnold, S. Gordon, G. J. Hämmerling, R. Ganss, CpG motifs as proinflammatory factors render autochthonous tumors permissive for infiltration and destruction. J Immunol 172, 5861-5869 (2004).

35. K. Takashima et al., STING in tumor and host cells cooperatively work for NK cell-mediated tumor growth retardation. Biochem Biophys Res Commun 478, 1764-1771 (2016).

36. C. W. M. Ong et al., Epidemic and pandemic viral infections: impact on tuberculosis and the lung: A consensus by the World Association for Infectious Diseases and Immunological Disorders (WAidid), Global Tuberculosis Network (GTN), and members of the European Society of Clinical Microbiology and Infectious Diseases Study Group for Mycobacterial Infections (ESGMYC). Eur Respir J 56, (2020).

37. E. D. Kilbourne, Influenza pandemics of the 20th century. Emerg Infect Dis 12, 9-14 (2006).

38. E. D. Kilbourne, Perspectives on pandemics: a research agenda. J Infect Dis 176 Suppl 1, S29-31 (1997).

39. H. Lau et al., The association between international and domestic air traffic and the coronavirus (COVID-19) outbreak. J Microbiol Immunol Infect 53, 467-472 (2020).

40. G. Ciliberto, R. Mancini, M. G. Paggi, Drug repurposing against COVID-19: focus on anticancer agents. J Exp Clin Cancer Res 39, 86 (2020).

41. J. Lan et al., Structure of the SARS-CoV-2 spike receptor-binding domain bound to the ACE2 receptor. Nature 581, 215-220 (2020).

42. D. Wrapp et al., Cryo-EM structure of the 2019-nCoV spike in the prefusion conformation. Science 367, 1260-1263 (2020).

43. M. D. Shin et al., COVID-19 vaccine development and a potential nanomaterial path forward. Nat Nanotechnol 15, 646-655 (2020).

44. S. Al-Halifa, L. Gauthier, D. Arpin, S. Bourgault, D. Archambault, Nanoparticle-Based Vaccines Against Respiratory Viruses. Front Immunol 10, 22 (2019).

45. D. van Riel, E. de Wit, Next-generation vaccine platforms for COVID-19. Nat Mater 19, 810-812 (2020).

46. K. S. Park, X. Sun, M. E. Aikins, J. J. Moon, Non-viral COVID-19 vaccine delivery systems. Adv Drug Deliv Rev, (2020).

47. C. A. O'dwyer et al., Expression of heterologous antigens in commensal Neisseria spp.: preservation of conformational epitopes with vaccine potential. Infect Immun 72, 6511-6518 (2004).

48. C. M. Guinane, P. D. Cotter, Role of the gut microbiota in health and chronic gastrointestinal disease: understanding a hidden metabolic organ. Therap Adv Gastroenterol 6, 295-308 (2013).

49. B. O. Schroeder, F. Bäckhed, Signals from the gut microbiota to distant organs in physiology and disease. Nat Med 22, 1079-1089 (2016).

50. Y. Belkaid, T. W. Hand, Role of the microbiota in immunity and inflammation. Cell 157, 121-141 (2014).

51. X. Zhang, B. D. Chen, L. D. Zhao, H. Li, The Gut Microbiota: Emerging Evidence in Autoimmune Diseases. Trends Mol Med 26, 862-873 (2020).

52. J. C. Clemente, J. Manasson, J. U. Scher, The role of the gut microbiome in systemic inflammatory disease. BMJ 360, j5145 (2018).

53. W. Ratajczak et al., Immunomodulatory potential of gut microbiome-derived short-chain fatty acids (SCFAs). Acta Biochim Pol 66, 1-12 (2019).

54. C. Nastasi et al., The effect of short-chain fatty acids on human monocyte-derived dendritic cells. Sci Rep 5, 16148 (2015).

55. G. Goverse et al., Diet-Derived Short Chain Fatty Acids Stimulate Intestinal Epithelial Cells To Induce Mucosal Tolerogenic Dendritic Cells. J Immunol 198, 2172-2181 (2017).

56. K. Inamura, Roles of microbiota in response to cancer immunotherapy. Semin Cancer Biol 65, 164-175 (2020).

57. K. A. Lee, H. M. Shaw, V. Bataille, P. Nathan, T. D. Spector, Role of the gut microbiome for cancer patients receiving immunotherapy: Dietary and treatment implications. Eur J Cancer 138, 149-155 (2020).

58. M. Nomura et al., Association of Short-Chain Fatty Acids in the Gut Microbiome With Clinical Response to Treatment With Nivolumab or Pembrolizumab in Patients With Solid Cancer Tumors. JAMA Netw Open 3, e202895 (2020).

59. C. Coutzac et al., Systemic short chain fatty acids limit antitumor effect of CTLA-4 blockade in hosts with cancer. Nat Commun 11, 2168 (2020).

60. P. C. Woo, H. W. Tsoi, L. P. Wong, H. C. Leung, K. Y. Yuen, Antibiotics modulate vaccine-induced humoral immune response. Clin Diagn Lab Immunol 6, 832-837 (1999).

61. S. E. de Jong, A. Olin, B. Pulendran, The Impact of the Microbiome on Immunity to Vaccination in Humans. Cell Host Microbe 28, 169-179 (2020).

62. Y. Bordon, Antibiotics can impede flu vaccines. Nat Rev Immunol 19, 663 (2019).

63. T. Hagan et al., Antibiotics-Driven Gut Microbiome Perturbation Alters Immunity to Vaccines in Humans. Cell 178, 1313-1328.e1313 (2019).

64. A. Li et al., Activating cGAS-STING pathway for the optimal effect of cancer immunotherapy. J Hematol Oncol 12, 35 (2019).

65. S. R. Woo, L. Corrales, T. F. Gajewski, The STING pathway and the T cell-inflamed tumor microenvironment. Trends Immunol 36, 250-256 (2015).

66. L. Corrales et al., Direct Activation of STING in the Tumor Microenvironment Leads to Potent and Systemic Tumor Regression and Immunity. Cell Rep 11, 1018-1030 (2015).

67. S. K. Gadkaree et al., Induction of tumor regression by intratumoral STING agonists combined with anti-programmed death-L1 blocking antibody in a preclinical squamous cell carcinoma model. Head Neck 39, 1086-1094 (2017).

68. G. N. Barber, STING: infection, inflammation and cancer. Nat Rev Immunol 15, 760-770 (2015).

69. T. Su et al., STING activation in cancer immunotherapy. Theranostics 9, 7759-7771 (2019).

70. B. Larkin et al., Cutting Edge: Activation of STING in T Cells Induces Type I IFN Responses and Cell Death. J Immunol 199, 397-402 (2017).

71. K. E. Sivick et al., Magnitude of Therapeutic STING Activation Determines CD8+ T Cell-Mediated Anti-tumor Immunity. Cell Rep 25, 3074-3085.e3075 (2018).

72. Z. Li, J. C. Barnes, A. Bosoy, J. F. Stoddart, J. I. Zink, Mesoporous silica nanoparticles in biomedical applications. Chemical Society reviews 41, 2590-2605 (2012).

73. Slowing, II, J. L. Vivero-Escoto, C. W. Wu, V. S. Lin, Mesoporous silica nanoparticles as controlled release drug delivery and gene transfection carriers. Adv Drug Deliv Rev 60, 1278-1288 (2008).

74. D. Shen et al., Biphase stratification approach to three-dimensional dendritic biodegradable mesoporous silica nanospheres. Nano Lett. 14, 923-932 (2014).

75. V. Cauda, A. Schlossbauer, T. Bein, Bio-degradation study of colloidal mesoporous silica nanoparticles: effect of surface functionalization with organo-silanes and poly (ethylene glycol). Micropor. Mesopor. Mat. 132, 60-71 (2010).

76. Z. Li, J. C. Barnes, A. Bosoy, J. F. Stoddart, J. I. Zink, Mesoporous silica nanoparticles in biomedical applications. Chem. Soc. Rev. 41, 2590-2605 (2012).

77. N. Benne, J. van Duijn, J. Kuiper, W. Jiskoot, B. Slütter, Orchestrating immune responses: How size, shape and rigidity affect the immunogenicity of particulate vaccines. J. Control. Release 234, 124-134 (2016).

78. D. Kwon et al., Extra-Large Pore Mesoporous Silica Nanoparticles for Directing in Vivo M2 Macrophage Polarization by Delivering IL-4. Nano Lett 17, 2747-2756 (2017).

79. C. Xu, J. Nam, H. Hong, Y. Xu, J. J. Moon, Positron Emission Tomography-Guided Photodynamic Therapy with Biodegradable Mesoporous Silica Nanoparticles for Personalized Cancer Immunotherapy. ACS nano 13, 12148-12161 (2019).

80. Y. Wang et al., A nanoparticle-based strategy for the imaging of a broad range of tumours by nonlinear amplification of microenvironment signals. Nat Mater 13, 204-212 (2014).

81. B. J. Francica et al., TNFα and Radioresistant Stromal Cells Are Essential for Therapeutic Efficacy of Cyclic Dinucleotide STING Agonists in Nonimmunogenic Tumors. Cancer Immunol Res 6, 422-433 (2018).

82. S. K. Sundararaman, D. A. Barbie, Tumor cGAMP Awakens the Natural Killers. Immunity 49, 585-587 (2018).

83. G. Alter, J. M. Malenfant, M. Altfeld, CD107a as a functional marker for the identification of natural killer cell activity. J Immunol Methods 294, 15-22 (2004).

84. E. Aktas, U. C. Kucuksezer, S. Bilgic, G. Erten, G. Deniz, Relationship between CD107a expression and cytotoxic activity. Cell Immunol 254, 149-154 (2009).

85. D. Shae et al., Endosomolytic polymersomes increase the activity of cyclic dinucleotide STING agonists to enhance cancer immunotherapy. Nat Nanotechnol 14, 269-278 (2019).

86. M. C. Hanson et al., Nanoparticulate STING agonists are potent lymph node-targeted vaccine adjuvants. J Clin Invest 125, 2532-2546 (2015).

87. L. C. Lin et al., Viromimetic STING Agonist-Loaded Hollow Polymeric Nanoparticles for Safe and Effective Vaccination against Middle East Respiratory Syndrome Coronavirus. Adv Funct Mater 29, 1807616 (2019).

88. P. U. Atukorale et al., Nanoparticle Encapsulation of Synergistic Immune Agonists Enables Systemic Codelivery to Tumor Sites and IFNbeta-Driven Antitumor Immunity. Cancer Res 79, 5394-5406 (2019).

89. D. R. Wilson et al., Biodegradable STING agonist nanoparticles for enhanced cancer immunotherapy. Nanomedicine 14, 237-246 (2018).

90. A. C. Anselmo, S. Mitragotri, A Review of Clinical Translation of Inorganic Nanoparticles. The AAPS journal 17, 1041-1054 (2015).

91. J. Fu et al., STING agonist formulated cancer vaccines can cure established tumors resistant to PD-1 blockade. Sci Transl Med 7, 283ra252 (2015).

92. O. Demaria et al., STING activation of tumor endothelial cells initiates spontaneous and therapeutic antitumor immunity. Proc Natl Acad Sci U S A 112, 15408-15413 (2015).

93. A. Sallets, S. Robinson, A. Kardosh, R. Levy, Enhancing immunotherapy of STING agonist for lymphoma in preclinical models. Blood Adv 2, 2230-2241 (2018).

94. A. Ghaffari et al., STING agonist therapy in combination with PD-1 immune checkpoint blockade enhances response to carboplatin chemotherapy in high-grade serous ovarian cancer. British journal of cancer 119, 440-449 (2018).

95. J. B. Foote et al., A STING Agonist Given with OX40 Receptor and PD-L1 Modulators Primes Immunity and Reduces Tumor Growth in Tolerized Mice. Cancer immunology research 5, 468-479 (2017).

96. L. Milling, Y. Zhang, D. J. Irvine, Delivering safer immunotherapies for cancer. Adv Drug Deliv Rev 114, 79-101 (2017).

97. R. S. Riley, C. H. June, R. Langer, M. J. Mitchell, Delivery technologies for cancer immunotherapy. Nature reviews 18, 175-196 (2019).

98. U. Sahin et al., Personalized RNA mutanome vaccines mobilize poly-specific therapeutic immunity against cancer. Nature 547, 222-226 (2017).

99. T. A. Barnes, E. Amir, HYPE or HOPE: the prognostic value of infiltrating immune cells in cancer. Br J Cancer 117, 451-460 (2017).

100. S. Shimizu et al., Tumor-infiltrating CD8+ T-cell density is an independent prognostic marker for oral squamous cell carcinoma. Cancer Med 8, 80-93 (2019).

101. F. Pagès et al., International validation of the consensus Immunoscore for the classification of colon cancer: a prognostic and accuracy study. Lancet 391, 2128-2139 (2018).

102. F. Petitprez, M. Meylan, A. de Reyniès, C. Sautès-Fridman, W. H. Fridman, The Tumor Microenvironment in the Response to Immune Checkpoint Blockade Therapies. Front Immunol 11, 784 (2020).

103. P. Bonaventura et al., Cold Tumors: A Therapeutic Challenge for Immunotherapy. Front Immunol 10, 168 (2019).

104. S. Demaria et al., Development of tumor-infiltrating lymphocytes in breast cancer after neoadjuvant paclitaxel chemotherapy. Clin Cancer Res 7, 3025-3030 (2001).

105. A. M. Heeren et al., Neoadjuvant cisplatin and paclitaxel modulate tumor-infiltrating T cells in patients with cervical cancer. Cancer Immunol Immunother 68, 1759-1767 (2019).

106. C. Achard et al., Lighting a Fire in the Tumor Microenvironment Using Oncolytic Immunotherapy. EBioMedicine 31, 17-24 (2018).

107. E. Lanitis, M. Irving, G. Coukos, Targeting the tumor vasculature to enhance T cell activity. Curr Opin Immunol 33, 55-63 (2015).

108. L. Corrales, T. F. Gajewski, Molecular Pathways: Targeting the Stimulator of Interferon Genes (STING) in the Immunotherapy of Cancer. Clin Cancer Res 21, 4774-4779 (2015).

109. J. Vollmer, A. M. Krieg, Immunotherapeutic applications of CpG oligodeoxynucleotide TLR9 agonists. Advanced Drug Delivery Reviews 61, 195-204 (2009).

110. H. Petersen et al., Polyethylenimine-graft-Poly(ethylene glycol) Copolymers: Influence of Copolymer Block Structure on DNA Complexation and Biological Activities as Gene Delivery System. Bioconjugate Chemistry 13, 845-854 (2002).

111. H. Petersen, P. M. Fechner, D. Fischer, T. Kissel, Synthesis, Characterization, and Biocompatibility of Polyethylenimine-graft-poly(ethylene glycol) Block Copolymers. Macromolecules 35, 6867-6874 (2002).

112. M. Yadav et al., Predicting immunogenic tumour mutations by combining mass spectrometry and exome sequencing. Nature 515, 572-576 (2014).

113. T. Kawai, S. Akira, Toll-like Receptors and Their Crosstalk with Other Innate Receptors in Infection and Immunity. Immunity 34, 637-650 (2011).

114. Daniel S. Chen, I. Mellman, Oncology Meets Immunology: The Cancer-Immunity Cycle. Immunity 39, 1-10 (2013).

115. S. R. Woo et al., STING-dependent cytosolic DNA sensing mediates innate immune recognition of immunogenic tumors. Immunity 41, 830-842 (2014).

116. R. E. Vatner, E. M. Janssen, STING, DCs and the link between innate and adaptive tumor immunity. Mol Immunol 110, 13-23 (2019).

117. C. Nakajima et al., A role of interferon-gamma (IFN-gamma) in tumor immunity: T cells with the capacity to reject tumor cells are generated but fail to migrate to tumor sites in IFN-gamma-deficient mice. Cancer Res 61, 3399-3405 (2001).

118. F. Castro, A. P. Cardoso, R. M. Gonçalves, K. Serre, M. J. Oliveira, Interferon-Gamma at the Crossroads of Tumor Immune Surveillance or Evasion. Front Immunol 9, 847 (2018).

119. I. Melero, A. Rouzaut, G. T. Motz, G. Coukos, T-cell and NK-cell infiltration into solid tumors: a key limiting factor for efficacious cancer immunotherapy. Cancer Discov 4, 522-526 (2014).

120. P. Bhat, G. Leggatt, K. I. Matthaei, I. H. Frazer, The kinematics of cytotoxic lymphocytes influence their ability to kill target cells. PLoS One 9, e95248 (2014).

121. P. Bhat, G. Leggatt, N. Waterhouse, I. H. Frazer, Interferon-γ derived from cytotoxic lymphocytes directly enhances their motility and cytotoxicity. Cell Death Dis 8, e2836 (2017).

122. M. A. Curran, W. Montalvo, H. Yagita, J. P. Allison, PD-1 and CTLA-4 combination blockade expands infiltrating T cells and reduces regulatory T and myeloid cells within B16 melanoma tumors. Proc Natl Acad Sci U S A 107, 4275-4280 (2010).

123. O. De Henau et al., Overcoming resistance to checkpoint blockade therapy by targeting PI3Kgamma in myeloid cells. Nature 539, 443-447 (2016).

124. R. Kuai et al., Subcutaneous Nanodisc Vaccination with Neoantigens for Combination Cancer Immunotherapy. Bioconjug Chem 29, 771-775 (2018).

125. S. C. Pandey, V. Pande, D. Sati, S. Upreti, M. Samant, Vaccination strategies to combat novel corona virus SARS-CoV-2. Life Sci 256, 117956 (2020).

126. T. Thanh Le et al., The COVID-19 vaccine development landscape. Nat Rev Drug Discov 19, 305-306 (2020).

127. V. Vetter, G. Denizer, L. R. Friedland, J. Krishnan, M. Shapiro, Understanding modern-day vaccines: what you need to know. Ann Med 50, 110-120 (2018).

128. C. B. Fox, R. M. Kramer, L. Barnes V, Q. M. Dowling, T. S. Vedvick, Working together: interactions between vaccine antigens and adjuvants. Ther Adv Vaccines 1, 7-20 (2013).

129. Y. Fan, J. J. Moon, Particulate delivery systems for vaccination against bioterrorism agents and emerging infectious pathogens. Wiley Interdiscip Rev Nanomed Nanobiotechnol 9, (2017).

130. A. L. Silva, P. C. Soema, B. Slütter, F. Ossendorp, W. Jiskoot, PLGA particulate delivery systems for subunit vaccines: Linking particle properties to immunogenicity. Hum Vaccin Immunother 12, 1056-1069 (2016).

131. P. Gu et al., Rational Design of PLGA Nanoparticle Vaccine Delivery Systems To Improve Immune Responses. Mol Pharm 16, 5000-5012 (2019).

132. J. Nam et al., Chemo-photothermal therapy combination elicits anti-tumor immunity against advanced metastatic cancer. Nat Commun 9, 1074 (2018).

133. S. A. C. Carabineiro, Applications of Gold Nanoparticles in Nanomedicine: Recent Advances in Vaccines. Molecules 22, (2017).

134. X. Hong et al., The pore size of mesoporous silica nanoparticles regulates their antigen delivery efficiency. Sci Adv 6, eaaz4462 (2020).

135. A. E. Gregory, R. Titball, D. Williamson, Vaccine delivery using nanoparticles. Front Cell Infect Microbiol 3, 13 (2013).

136. A. M. Reichmuth, M. A. Oberli, A. Jaklenec, R. Langer, D. Blankschtein, mRNA vaccine delivery using lipid nanoparticles. Ther Deliv 7, 319-334 (2016).

137. E. M. Mucker et al., Lipid Nanoparticle Formulation Increases Efficiency of DNA-Vectored Vaccines/Immunoprophylaxis in Animals Including Transchromosomic Bovines. Sci Rep 10, 8764 (2020).

138. D. Hobernik, M. Bros, DNA Vaccines-How Far From Clinical Use? Int J Mol Sci 19, (2018).

139. W. L. Fotoran, R. Santangelo, B. N. M. de Miranda, D. J. Irvine, G. Wunderlich, DNA-Loaded Cationic Liposomes Efficiently Function as a Vaccine against Malarial Proteins. Mol Ther Methods Clin Dev 7, 1-10 (2017).

140. R. Kuai, L. J. Ochyl, K. S. Bahjat, A. Schwendeman, J. J. Moon, Designer vaccine nanodiscs for personalized cancer immunotherapy. Nat Mater 16, 489-496 (2017).

141. A. G. Dalgleish et al., The CD4 (T4) antigen is an essential component of the receptor for the AIDS retrovirus. Nature 312, 763-767 (1984).

142. J. R. Mascola, B. F. Haynes, HIV-1 neutralizing antibodies: understanding nature's pathways. Immunol Rev 254, 225-244 (2013).

143. R. W. Sanders et al., A next-generation cleaved, soluble HIV-1 Env Trimer, BG505 SOSIP.664 gp140, expresses multiple epitopes for broadly neutralizing but not non-neutralizing antibodies. PLoS pathogens 9, e1003618 (2013).

144. S. W. de Taeye et al., Immunogenicity of Stabilized HIV-1 Envelope Trimers with Reduced Exposure of Non-neutralizing Epitopes. Cell 163, 1702-1715 (2015).

145. R. W. Sanders et al., HIV-1 VACCINES. HIV-1 neutralizing antibodies induced by native-like envelope trimers. Science 349, aac4223 (2015).

146. L. Goo, V. Chohan, R. Nduati, J. Overbaugh, Early development of broadly neutralizing antibodies in HIV-1-infected infants. Nat Med 20, 655-658 (2014).

147. F. Wu et al., A new coronavirus associated with human respiratory disease in China. Nature 579, 265-269 (2020).

148. K. G. Andersen, A. Rambaut, W. I. Lipkin, E. C. Holmes, R. F. Garry, The proximal origin of SARS-CoV-2. Nat Med 26, 450-452 (2020).

149. J. Yang et al., A vaccine targeting the RBD of the S protein of SARS-CoV-2 induces protective immunity. Nature, (2020).

150. W. Tai et al., A novel receptor-binding domain (RBD)-based mRNA vaccine against SARS-CoV-2. Cell Res, (2020).

151. I. S. Georgiev et al., Single-Chain Soluble BG505.SOSIP gp140 Trimers as Structural and Antigenic Mimics of Mature Closed HIV-1 Env. J Virol 89, 5318-5329 (2015).

152. J. J. Moon et al., Interbilayer-crosslinked multilamellar vesicles as synthetic vaccines for potent humoral and cellular immune responses. Nature Materials 10, 243-251 (2011).

153. J. D. Bazzill et al., Interrogation of Antigen Display on Individual Vaccine Nanoparticles for Achieving Neutralizing Antibody Responses against Hepatitis C Virus. Nano Lett 18, 7832-7838 (2018).

154. J. D. Bazzill et al., Vaccine nanoparticles displaying recombinant Ebola virus glycoprotein for induction of potent antibody and polyfunctional T cell responses. Nanomedicine, (2018).

155. Y. Fan et al., Multilamellar Vaccine Particle Elicits Potent Immune Activation with Protein Antigens and Protects Mice against Ebola Virus Infection. ACS Nano 13, 11087-11096 (2019).

156. D. C. Montefiori, in HIV protocols. (Springer, 2009), pp. 395-405.

157. M. Sarzotti-Kelsoe et al., Optimization and validation of the TZM-bl assay for standardized assessments of neutralizing antibodies against HIV-1. J Immunol Methods 409, 131-146 (2014).

158. J. Gao, L. J. Ochyl, E. Yang, J. J. Moon, Cationic liposomes promote antigen cross-presentation in dendritic cells by alkalizing the lysosomal pH and limiting the degradation of antigens. Int J Nanomedicine 12, 1251-1264 (2017).

159. S. Beddows et al., A comparative immunogenicity study in rabbits of disulfide-stabilized, proteolytically cleaved, soluble trimeric human immunodeficiency virus type 1 gp140, trimeric cleavage-defective gp140 and monomeric gp120. Virology 360, 329-340 (2007).

160. B. S. Graham, J. R. Mascola, Lessons from failure--preparing for future HIV-1 vaccine efficacy trials. J Infect Dis 191, 647-649 (2005).

161. Z. M. Qualls et al., Identification of Novel Structural Determinants in MW965 Env That Regulate the Neutralization Phenotype and Conformational Masking Potential of Primary HIV-1 Isolates. J Virol 92, (2018).

162. R. W. Sanders et al., HIV-1 VACCINES. HIV-1 neutralizing antibodies induced by native-like envelope trimers. Science 349, aac4223 (2015).

163. P. Riccio, R. Rossano, The human gut microbiota is neither an organ nor a commensal. FEBS Lett 594, 3262-3271 (2020).

164. J. Schulthess et al., The Short Chain Fatty Acid Butyrate Imprints an Antimicrobial Program in Macrophages. Immunity 50, 432-445.e437 (2019).

165. A. Bachem et al., Microbiota-Derived Short-Chain Fatty Acids Promote the Memory Potential of Antigen-Activated CD8. Immunity 51, 285-297.e285 (2019).

166. F. Y. Shaikh, C. L. Sears, Messengers from the microbiota. Science 369, 1427-1428 (2020).

167. L. F. Mager et al., Microbiome-derived inosine modulates response to checkpoint inhibitor immunotherapy. Science 369, 1481-1489 (2020).

168. B. Routy et al., Gut microbiome influences efficacy of PD-1-based immunotherapy against epithelial tumors. Science 359, 91-97 (2018).

169. V. Gopalakrishnan et al., Gut microbiome modulates response to anti-PD-1 immunotherapy in melanoma patients. Science 359, 97-103 (2018).

170. D. Vandeputte et al., Prebiotic inulin-type fructans induce specific changes in the human gut microbiota. Gut 66, 1968-1974 (2017).

171. S. Hiel et al., Effects of a diet based on inulin-rich vegetables on gut health and nutritional behavior in healthy humans. Am J Clin Nutr 109, 1683-1695 (2019).

172. N. G. Vallianou, T. Stratigou, S. Tsagarakis, Metformin and gut microbiota: their interactions and their impact on diabetes. Hormones (Athens) 18, 141-144 (2019).

173. T. Bryrup et al., Metformin-induced changes of the gut microbiota in healthy young men: results of a non-blinded, one-armed intervention study. Diabetologia 62, 1024-1035 (2019).

174. H. Wu et al., Metformin alters the gut microbiome of individuals with treatment-naive type 2 diabetes, contributing to the therapeutic effects of the drug. Nat Med 23, 850-858 (2017).

175. N. Larsen et al., Potential of Pectins to Beneficially Modulate the Gut Microbiota Depends on Their Structural Properties. Front Microbiol 10, 223 (2019).

176. T. Jiang et al., Apple-Derived Pectin Modulates Gut Microbiota, Improves Gut Barrier Function, and Attenuates Metabolic Endotoxemia in Rats with Diet-Induced Obesity. Nutrients 8, 126 (2016).

177. S. J. Bang et al., Effect of raw potato starch on the gut microbiome and metabolome in mice. Int J Biol Macromol 133, 37-43 (2019).

178. H. Earley et al., The abundance of Akkermansia muciniphila and its relationship with sulphated colonic mucins in health and ulcerative colitis. Sci Rep 9, 15683 (2019).

179. A. Hänninen et al., induces gut microbiota remodelling and controls islet autoimmunity in NOD mice. Gut 67, 1445-1453 (2018).

180. M. C. Dao et al., Akkermansia muciniphila and improved metabolic health during a dietary intervention in obesity: relationship with gut microbiome richness and ecology. Gut 65, 426-436 (2016).

181. R. Caruso, M. Ono, M. E. Bunker, G. Núñez, N. Inohara, Dynamic and Asymmetric Changes of the Microbial Communities after Cohousing in Laboratory Mice. Cell Rep 27, 3401-3412.e3403 (2019).

182. Y. Shi, R. van der Meel, X. Chen, T. Lammers, The EPR effect and beyond: Strategies to improve tumor targeting and cancer nanomedicine treatment efficacy. Theranostics 10, 7921-7924 (2020).

183. K. Greish, Enhanced permeability and retention (EPR) effect for anticancer nanomedicine drug targeting. Methods Mol Biol 624, 25-37 (2010).

184. R. Rampado, S. Crotti, P. Caliceti, S. Pucciarelli, M. Agostini, Recent Advances in Understanding the Protein Corona of Nanoparticles and in the Formulation of "Stealthy" Nanomaterials. Front Bioeng Biotechnol 8, 166 (2020).

185. Y. Hailemichael et al., Persistent antigen at vaccination sites induces tumor-specific $CD8^+$ T cell sequestration, dysfunction and deletion. Nat Med 19, 465-472 (2013).

186. S. Gnjatic, N. Bhardwaj, Antigen depots: T cell traps? Nat Med 19, 397-398 (2013).

187. H. Harlin et al., Chemokine expression in melanoma metastases associated with CD8+ T-cell recruitment. Cancer Res 69, 3077-3085 (2009).

188. A. Ager, H. A. Watson, S. C. Wehenkel, R. N. Mohammed, Homing to solid cancers: a vascular checkpoint in adoptive cell therapy using CAR T-cells. Biochem Soc Trans 44, 377-385 (2016).

189. D. Wakita et al., Cisplatin Augments Antitumor T-Cell Responses Leading to a Potent Therapeutic Effect in Combination With PD-L1 Blockade. Anticancer Res 39, 1749-1760 (2019).

190. L. Wang-Bishop et al., Potent STING activation stimulates immunogenic cell death to enhance antitumor immunity in neuroblastoma. J Immunother Cancer 8, (2020).

191. R. Janssen, M. H. Wauben, J. Tommassen, Quaternary structure of a carrier protein influences antigenicity and immunogenicity of an inserted T cell determinant. Int Immunol 8, 829-836 (1996).

192. D. Parada Venegas et al., Short Chain Fatty Acids (SCFAs)-Mediated Gut Epithelial and Immune Regulation and Its Relevance for Inflammatory Bowel Diseases. Front Immunol 10, 277 (2019).

193. A. Haslam, V. Prasad, Estimation of the Percentage of US Patients With Cancer Who Are Eligible for and Respond to Checkpoint Inhibitor Immunotherapy Drugs. JAMA Netw Open 2, e192535 (2019).

194. P. Sharma, S. Hu-Lieskovan, J. A. Wargo, A. Ribas, Primary, Adaptive, and Acquired Resistance to Cancer Immunotherapy. Cell 168, 707-723 (2017).